64-10



VIDYA REPORT NO. 107
August 15, 1963

# THE EFFECT OF FLOW SEPARATION FROM THE HULL ON THE STABILITY OF A HIGH-SPEED SUBMARINE

## PART I—THEORY

by
S. B. Spangler
A. H. Sacks
J. N. Nielsen

prepared for
**OFFICE OF NAVAL RESEARCH**
and
**DAVID TAYLOR MODEL BASIN**

VIDYA PROJECT NO. 9065

This research was jointly sponsored by the Bureau of Ships Fundamental Hydromechanics Research Program, S-R009 01 01, administered by the David Taylor Model Basin, and by the Fluid Dynamics Branch of the Office of Naval Research, under Contract No. Nonr 3934(00).



VIDYA

RESEARCH AND DEVELOPMENT



1450 PAGE MILL ROAD, PALO ALTO, CALIFORNIA

A DIVISION OF Itek CORPORATION

FOR ERRATA

AD 432355

THE FOLLOWING PAGES ARE CHANGES

TO BASIC DOCUMENT

# ERRATA

April 8, 1964

Vidya Report No. 107

## THE EFFECT OF FLOW SEPARATION FROM THE HULL ON THE STABILITY OF A HIGH-SPEED SUBMARINE

### PART I - THEORY

by
S. B. Spangler
A. H. Sacks
J. N. Nielsen

Prepared for
OFFICE OF NAVAL RESEARCH
and
DAVID TAYLOR MODEL BASIN

Vidya Project No. 9065

| Page | Item |
|---|---|
| x | "Appendix D" should be "Report 107, Part II" |
| 8 | In Equation (3-1), the second term should be changed from $\frac{\partial^2\phi}{\partial\bar{z}^2}$ to $\frac{\partial^2\phi}{\partial\bar{y}^2}$ |
| 14 | Equation (3-13) should read $I = i\rho\Gamma\left[\zeta_1 - \frac{a^2}{\bar{\zeta}_1} + \bar{\zeta}_1 - \frac{a^2}{\zeta_1}\right]$ |
| 15 | The bracketed term of Equation (3-14) should read $\left(\zeta_1 + \bar{\zeta}_1 - \frac{a^2}{\zeta_1} - \frac{a^2}{\bar{\zeta}_1}\right)$ |
| B-1 | Equation (B-1) should read $W = -i\frac{\Gamma(t)}{2\pi}\ln\zeta = -i\frac{\Gamma(t)}{2\pi}\ln\left(re^{i\theta}\right) = -i\frac{\Gamma(t)}{2\pi}\ln r + \frac{\Gamma(t)}{2\pi}\theta$ |

| Page | Item |
| --- | --- |
| B-1 | The equation $\phi = \frac{\Gamma(t)}{2\pi}\,\theta$ should be denoted as (B-2). |
| B-3 | The bracketed part of the second equation after (B-2) should read $$\frac{\dot{\Gamma}(t)}{2\pi}\,2\pi - \frac{\dot{\Gamma}(t)}{2\pi}\,0$$ |
| B-4 | Equation (B-7) should read $$F_v = i\rho\Gamma(V_1 - \dot{\zeta}_1)$$ |
| Fig. 17 | The notation $Re_D = 3\times10^6$ should read $$Re_l = 3\times10^6$$ |
| Fig. 22 | The callout arrow at axial station $x/l \cong 0.06$ should be noted "transition." |
| Fig. 27 | The zero on the ordinate belongs at the top of the graph, not the bottom. |
| Fig. 29 | The zero on the ordinate at the lower end should be removed. The numbers 18, and 20 on the abcissa should be replaced by 20 and 24, respectively. |

व VIDYA

*The word Vidya, taken from the Vedanta philosophy of the Hindus, means knowledge. The symbol used to denote the Vidya organization is the letter "V" from Sanskrit, the ancient language of India.*

APPLIED MECHANICS....PHYSICS....ANALYSES

Copy No. 196

VIDYA REPORT NO. 107

August 15, 1963

# THE EFFECT OF FLOW SEPARATION FROM THE HULL ON THE STABILITY OF A HIGH-SPEED SUBMARINE

## PART I - THEORY

by

S. B. Spangler

A. H. Sacks

J. N. Nielsen

Prepared for

OFFICE OF NAVAL RESEARCH

and

DAVID TAYLOR MODEL BASIN

Vidya Project No. 9065



VIDYA

A DIVISION OF Itek CORPORATION

This research was jointly sponsored by the Bureau of Ships Fundamental Hydromechanics Research Program, S-R009 01 01, administered by the David Taylor Model Basin, and by the Fluid Dynamics Branch of the Office of Naval Research, under Contract No. Nonr 3934(00).

1450 PAGE MILL ROAD • PALO ALTO, CALIFORNIA

TEL: DAVENPORT 1-2455 TWX: 415 492-9270

## SUMMARY

The problem of predicting theoretically the force distribution induced on a submarine hull by flow separation at high angle of attack is considered. The hull is taken to be a body of revolution with a pointed tail. The flow is assumed to be incompressible and inviscid. The assumptions of slender-body theory are used, and the steady, three-dimensional vortex configuration on the leeward side of the inclined body is represented by an unsteady, two-dimensional vortex motion in a normal plane. The resulting force distribution is determined in terms of an assumed variation of the location of the separation line on the body with axial length.

The theory is applied to the case of a high-speed submarine at angle of attack. The total forces and moments on the submarine are determined as the sum of the forces predicted by slender-body theory in the absence of separation and the forces predicted by the separation theory. Experimental data on the location of separation on an inclined cylindrical body are used with the theory to predict the normal force and pitching moment for angles of attack up to 20° for a typical submarine configuration. Nonlinear effects attributable to separation are found to start at an angle of attack of approximately 8°. These effects are found to reach the same magnitude as the non-separated forces and moments at an angle of attack of 20°. Comparisons with experimental data for a specific submarine configuration (Part II of this report) indicate that the theory predicts well the onset and the qualitative nature of the nonlinear effects. The quantatative agreement is fair. The dependence of these results on the assumed hull separation characteristics and the complete lack of experimental separation data applicable to the submarine case is discussed.

The method of Truckenbrodt for axisymmetric, incompressible turbulent boundary layers is used to predict the boundary-layer blanketing effect on the stern control surfaces for a typical submarine. It is concluded that this is not a significant effect for the case considered.

## TABLE OF CONTENTS

## LIST OF FIGURES

## LIST OF SYMBOLS

| | |
|---|---|
| $a$ | local body radius, feet |
| $C_{D_C}$ | cross-flow drag coefficient, $C_{D_C} = \dfrac{dN/dx}{q_\infty (\sin^2 \alpha)\, 2a}$ |
| $C_f$ | average skin-friction coefficient |
| $C_f'$ | local skin-friction coefficient, $C_f' = \dfrac{\tau_\omega}{\frac{1}{2}\rho U_\infty^2}$ |
| $C_p$ | pressure coefficient, $C_p = \dfrac{p - p_\infty}{q_\infty}$ |
| $C_p$ | prismatic coefficient, $C_p = 4 \times \text{Hull Vol}/\pi d^2 l$ |
| $d$ | maximum body diameter, feet |
| $H$ | boundary-layer shape parameter, $H \equiv \delta^*/\theta$ |
| $\bar{H}$ | boundary-layer shape parameter, $\bar{H} \equiv \delta^{**}/\theta$ |
| $I$ | impulse, lb-sec/ft |
| $i$ | $\sqrt{-1}$ |
| $L$ | Truckenbrodt shape factor, defined by Equation (46), Reference 28 |
| $l$ | body axial length, feet |
| $M$ | pitching moment about center of gravity unless noted otherwise, ft-lb |
| $M$ | Mach number |
| $m$ | nondimensional axial position of maximum body thickness, $m = \dfrac{x_m}{l}$ |
| $N$ | normal force, lb. Positive in positive z direction |
| $N_V$ | viscous normal force, or that force induced by separation and vortex motion |
| $\dfrac{dN}{dx}$ | normal force per unit length, lb/ft |
| $p$ | static pressure, psfa |

$q$ dynamic head, $lb/ft^2$

$r$ radial distance from origin in a cylindrical coordinate system, feet

Re Reynolds number based on free-stream velocity and a characteristic length

$Re_\theta$ Reynolds number based on momentum thickness

$Re_x$ Reynolds number based on axial distance along body

$Re_l$ Reynolds number based on body axial length

$r_o$ nondimensional nose radius, $r_o$ = nose radius $\times l/d^2$

$r_1$ nondimensional tail radius, $r_1$ = tail radius $\times l/d^2$

S body cross-section area, $ft^2$

t time, sec

$U_\infty$ free-stream velocity, ft/sec

U local velocity at body surface given by potential flow, ft/sec

$u',v'$ velocities along the $x'$, $y'$ direction, respectively, ft/sec

$v_r,v_\theta$ radial and tangential velocities, respectively, in an $r$, $\theta$ coordinate system, ft/sec

V complex velocity in the normal plane, ft/sec

v, w velocity components along the real (y) and imaginary (z) axes in the normal plane, ft/sec

W complex potential, $W = \phi + i\psi$

$x_s$ axial station on the body where separation first appears, feet

x,y,z orthogonal coordinate system oriented with reference to the body, see Figure 5

$\bar{x},\bar{y},\bar{z}$ orthogonal coordinate system oriented with reference to velocity vector, see Figure 5

$x', y'$ — coordinates in an orthogonal curvilinear coordinate system tangential to and normal to local body surface, respectively

$\alpha$ — angle of attack, degrees

$\beta$ — angle of drift, degrees

$\Gamma$ — vortex strength, $ft^2/sec$

$\delta$ — boundary-layer thickness, ft, unless otherwise noted

$\delta^*$ — boundary-layer displacement thickness, ft, unless otherwise noted

$\delta^{**}$ — boundary-layer energy thickness, ft, unless otherwise noted

$\zeta$ — complex coordinate in normal plane, $\zeta = y + iz = re^{i\theta}$

$\bar{\zeta}$ — complex conjugate coordinate in normal plane, $\bar{\zeta} = y - iz = re^{-i\theta}$

$\theta$ — angle of a radius vector with respect to $y$ axis in normal plane, degree

$\theta$ — momentum thickness of boundary layer, ft, unless otherwise noted

$\lambda$ — distance along body surface from nose, feet

$\xi$ — integration variable, defined in Equation (4-14)

$\rho$ — density, $lb\text{-}sec^2/ft^4$

$\tau$ — shear stress, $lb/ft^2$

$\tau_w$ — shear stress at the wall, $lb/ft^2$

$\phi$ — velocity potential

$\psi$ — stream function

Subscripts and Superscripts

$(\ )_l$ — laminar value

$(\ )_t$ — turbulent value

$(\ )_V$ — viscous, or induced by separation and vortex shedding

$(\ )_{CG}$ property of the center of gravity

$(\ )_{\infty}$ property of the free-stream flow

$(\ )_{o}$ property of the separation point on the body in the normal plane

$(\ )_{1}$ property of the center of the vortex in the normal plane

$(\ )_{RE}$ real part of variable

$(\ )_{IM}$ imaginary part of variable

$(\dot{\ })$ time derivative of variable

$(\bar{\ })$ complex conjugate of variable

The nomenclature of Section 5.3 and Appendix D for the forces and moments on a submarine corresponds to that of Reference 37. The following variables were used:

x,y,z orthogonal coordinate system oriented with respect to the submarine axis, z positive downward

$M'$ pitching moment, positive nose up, $M' = \dfrac{M}{q_{\infty}\, l^3}$

$N'$ yawing moment, positive nose starboard, $N' = \dfrac{N}{q_{\infty}\, l^3}$

$Y'$ lateral force, positive starboard, $Y' = \dfrac{Z}{q_{\infty}\, l^2}$

$Z'$ vertical force, positive downward, $Z' = \dfrac{Z}{q_{\infty}\, l^2}$

$q'$ angular velocity in pitch, $q' = \dfrac{ql}{U_{\infty}}$

$r'$ angular velocity in yaw, $r' = \dfrac{rl}{U_{\infty}}$

# THE EFFECT OF FLOW SEPARATION FROM THE HULL ON THE STABILITY OF A HIGH-SPEED SUBMARINE PART I - THEORY

## 1. INTRODUCTION

This is the first Technical Report under Contract Nonr 3934(00). This report describes the work done to date under the subject contract to predict analytically the effects of flow separation from the hull on the static stability characteristics of a modern, high-speed submarine at angle of attack. This work was sponsored jointly by the Office of Naval Research and the Bureau of Ships under the latter's Fundamental Hydromechanics Research Program administered by the David Taylor Model Basin.

In the last decade, the philosophy of design of the submarine has changed radically. The advent of the nuclear power plant has made it feasible to design a submarine primarily for submerged operation with a capability of sustained, high-speed operation. As a result there has been an increasing interest in the submerged dynamic behavior and the stability characteristics of the submarine. In particular, it has become highly desirable to predict analytically its stability characteristics under various conditions of motion and attitude. The study described in this report has the purpose of developing a method of predicting the normal force and pitching moment on a high-speed submarine configuration at angle of attack, with specific interest in that range of angle of attack in which flow separation occurs on the hull. The general approach to the problem has been to characterize the separated flow region over the leeward side of the hull in terms of a steady vortex system which induces a viscous force distribution on the hull and stern control surfaces.

The analysis of the high angle-of-attack case is described in the following work. In addition, certain boundary-layer effects are investigated, and calculations are made for the zero angle-of-attack case. The methods are applied to a typical high-speed submarine configuration in order to determine the importance of the various effects.

A classified portion of this report, Part II, shows comparisons between theory and experiment for a specific submarine configuration. Finally, the theory is evaluated in terms of the assumptions made and the comparisons with experimental data.

## 2. GENERAL STATEMENT OF THE PROBLEM

The section contains a discussion of the geometric characteristics of the submarine as they pertain to this study and a description of the two regions of flow over the submarine as distinguished by whether or not flow separation occurs on the leeward side of the hull at angles of attack.

A sketch of a modern, high-speed submarine is shown in Figure 1. In general, if the submarine is at an angle of attack in the vertical plane or at an attitude of yaw and roll in the horizontal plane, the bridge fairwater and fairwater planes will induce forces on the hull and stern control surfaces, which would not exist in the absence of these appendages. In addition, if the flow over the hull is separated due to angle of attack or drift, forces arising from separation will be induced on the hull and stern control surfaces. These "interference" forces will affect the total forces and moments on the submarine and therefore its stability characteristics. The first step in analyzing this problem is to investigate the interference forces arising from flow separation on the hull at high angle of attack. This is the problem to which the following study is directed. For this purpose, the submarine configuration which will be assumed is that of a hull, consisting of a long, slender body of revolution, having a cruciform control surface arrangement at the stern. The effect of the bridge fairwater, fairwater planes, bow planes and deck on the flow over the submarine at angle of attack will not be considered in the present study.

At zero and the small angles of attack, the flow over the assumed configuration is everywhere attached except at the stern where a wake is shed. Because the Reynolds number is high (a typical length Reynolds number is the order of $5\times10^{8}$), the boundary layer is turbulent over almost the entire length of the hull. At the stern the thick boundary layer blankets a considerable portion of the stern planes in a low-velocity fluid. This blanketing tends to reduce the effectiveness of the stern planes both as a stabilizing device and as a method of control. In addition, at small angles of attack, the boundary layer thins on the windward side and thickens on the leeward side. The resulting change in the pressure distribution over the aft portion of the hull produces a normal force, since, for inviscid flow there is no normal force at angle of attack. Thus, the turbulent boundary-layer could have an appreciable effect on the forces on the hull and stern planes at zero and small angles of attack.

At large angles of attack, flow separation occurs on the leeward side of the hull and a vortex sheet configuration occurs over the leeward side of the hull, much as shown in the following sketch:

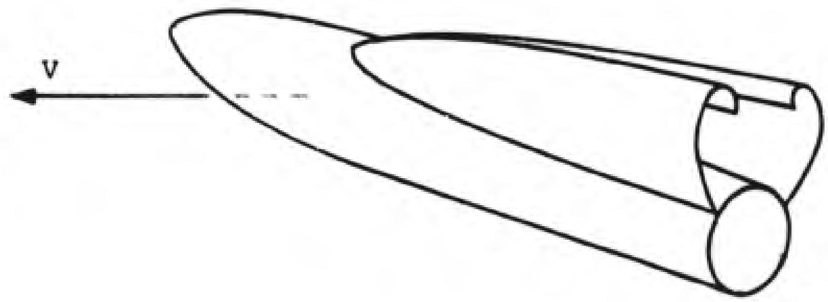


This flow configuration was first studied in detail in connection with missiles, in which some unexpected stability characteristics were traced to interference effects induced by the shed vortex system. Several experimental studies have been made of the vortex system above the leeward side of bodies at high angle of attack (Refs. 1 to 8). In these studies, it has been found for both low speed and supersonic flow that at some angle of attack separation first appears at the rear of the body and as the angle of attack is increased, the axial location of the origin of separation moves forward. A vortex sheet is attached to the body along the line of separation and rolls up over the body. Over a wide range of flow conditions, the configuration is symmetrical with respect to a vertical plane passing through the body longitudinal axis and steady with respect to the body.

This type of flow configuration has been investigated experimentally by means of flow field measurements and smoke or vapor-screen photographs. An example of the former is the work of Mello, Reference 6. Typical measurements by Mello are shown in Figure 2 for Mach 2 at $\alpha = 20^{\circ}$. The left-hand side of Figure 2 shows contours of constant ratio of local to free-stream total pressure. The right-hand side shows velocity direction and magnitude deduced from total and static pressure measurements made throughout the flow field. Both measurements indicate the presence of a steady vortex pair above the body. Mello was also able to obtain good correlation between measured vortex strength and a predicted vortex strength based on measured vortex position and vortex induced forces. The theory used was based on slender-body theory, as is the present analysis.

Smoke- and vapor-screen methods are used to follow visually the development of the separation vortices along the length of the body. A typical smoke-screen photograph, reproduced from Reference 7, is shown in Figure 3 for $\alpha = 25^{\circ}$ and a velocity of 50 ft/sec on a pointed body of revolution. A plane of light across the tunnel illuminates the flow over the model and shows the centers of strong vorticity as spots in the smoke-filled region over the body. By moving the plane of light along the tunnel the axial development of the vortex core may be followed. Water-vapor condensation may be used in a similar fashion in a supersonic tunnel to indicate the centers of strong vorticity, as described in Reference 4. Reference 2 has a number of good vapor-screen photographs of vortex development on inclined bodies.

In addition to these basic studies on separation and vortex shedding from inclined bodies, methods have been developed which predict quite well the influence of shed vortices on the stability characteristics of complete aircraft and missile configurations (Refs. 9, 10, and 20).

The general approach to the analysis of the static stability characteristics in the vertical plane of a hull with stern planes will be to consider two extremes of attitude. The first, to which most of the work has been devoted, is the case of high angle of attack with flow separation. Much of the theoretical work done to date on vortex shedding from inclined bodies has used experimental data on vortex position or cross-flow drag coefficients. Since no such data are available for flow conditions and configurations resembling the submarine case, a method will be developed for predicting the position and strength of the shed vortex system and the induced hull forces. The method will be based on a known or assumed location of the separation line on the body. The second case is that of zero angle of attack in which boundary-layer characteristics will be determined and their influence on the forces and moments estimated.

## 3. HIGH ANGLE-OF-ATTACK STUDY

The analysis of vortex shedding from an inclined submarine hull consists of selecting a suitable flow model and then analyzing the model to obtain the expressions describing the vortex motion and induced forces. These subjects are discussed in the first two sections. The remaining three sections contain discussions on the use and characteristics of the method, its application to the submarine, and the stability of the vortex motion.

### 3.1 Flow Model

The flow model should represent the actual flow to the greatest extent possible and yet be tractable analytically. In the following discussion, the actual flow characteristics are described, and a model is selected as a first compromise between these two requirements.

Flow separation from a body of revolution at angle of attack is a three-dimensional problem. The essential features are illustrated in Figure 4. These features are not precisely known, but are probably very close to those shown. The discussion below follows that of Reference 11, on the basic characteristics of three-dimensional separation. Separation occurs along two lines symmetrically disposed with regard to the vertical plane of symmetry and located generally on the leeward part of the body. These lines probably meet on the body surface in the vertical plane of symmetry. At this point the separated region is probably limited to a small bubble with the flow reattaching and moving over the body surface between the free vortex layers. The surface streamlines approach the separation line from either direction and enter the separation line tangentially where they join. A streamline in the separation surface, or vortex sheet, then leaves the body surface and is inclined downstream in the sheet, following the sheet as it rolls up. The vorticity characteristics of the sheet may be visualized by considering the sheet to be made up of a large number of vortex filaments, lying side by side to form a surface. Each of these filaments originates at the separation line and has a strength given by the rate of vorticity input per unit length at the point on the separation line. These filaments do not have any force on them and follow the local streamlines (see, for instance, Ref. 12, Para. 13.10). Consequently, the line indicated as a separation streamline could also be considered one of the vortex filaments making up the vortex sheet. The filaments become more closely spaced in the rolled-up portion of the sheet and produce a region of concentrated vorticity there.

To perform an analysis of this problem, the following general approach would have to be used. Separation is caused by a viscous flow mechanism within the boundary layer. However, once separation has occured, the flow field is assummed to be inviscid and its vorticity characteristics are given by vortex filaments whose viscous cores are vanishingly small and which behave like ideal line vortices in their effect on the velocity in the flow field. Each element of length of each vortex filament contributes to the velocity in the flow field according to the filament strength and the distance from the filament element to the point in the flow field. Therefore, to get the velocity (magnitude and direction) at any point in the flow field, the contribution of all of the vortex filament length elements must be summed and added to the velocity at that point due to the free-stream flow around the body. If the point of interest is on the surface of the body, the resultant velocity will not, in general, be tangential to the body surface. In order to cause the body surface to be a stream surface, there must be some form of image vortex filament system inside the body whose velocity contribution will just cancel the normal velocity component of the external vortex filament system on the body surface. Since the induced velocities are dependent on the strengths of the vortex filaments, these must be specified, probably by recourse to experimental data. In principle, the problem may then be described by a number of simultaneous equations relating the velocities in the flow field to the location and strength of the vortex filaments and their images such that the vortex filaments lie everywhere tangent to the streamlines and the body surface is caused to be a stream surface. From a practical standpoint, a solution to this problem might involve making such simplifications as approximating the curved vortex filaments by a series of straight lines, imposing the boundary condition of no flow through the body surface only at discrete points rather than over the entire surface, and imposing the condition of tangency of the vortex filaments to the streamlines only at discrete points rather than along their entire length.

There is a possibility of simplifying the flow model considerably by making use of slender-body theory. This is the approach that has been taken in most of the interference problems arising in the missile field. In fact, it is quite reasonable to use the theory and methods developed in missile technology for the case of the submarine for two reasons. First, the geometry of the submarine is much like that of the missile. Both vehicles are basically long slender bodies of revolution having relatively small control surfaces located at the aft end of the body. Second, the slender-body methods which have been developed for predicting wing-body-tail interference effects for missiles use incompressible-flow techniques which are applicable equally to the supersonic missile and the submarine.

Slender-body theory is applicable for cases in which the body transverse or radial dimensions are small compared to the length dimensions. Under these circumstances, the first term of the linearized, steady, potential flow equation, Equation (3-1),

$$(1 - M_\infty^2) \frac{d^2\phi}{d\bar{x}^2} + \frac{d^2\phi}{d\bar{z}^2} + \frac{d^2\phi}{d\bar{z}^2} = 0 \qquad (3\text{-}1)$$

is small compared with the other two terms and may be neglected.[1] Equation (3-1) is written in its compressible form and differs from the incompressible form in that the term $(1 - M_\infty^2)$ is not present in the latter case. It can be seen that since the effect of compressibility enters only in the first term, the compressible problem becomes an incompressible problem in two dimensions when the first term is dropped. This is the basis for the statement that missile slender-body methods may be applied directly to the submarine and also the basis for the applicability of experimental results on supersonic flow over inclined bodies with vortex shedding to the case of the submarine at angle of attack. With the assumption of a slender body, Equation (3-1) becomes

$$\frac{d^2\phi}{d\bar{y}^2} + \frac{d^2\phi}{d\bar{z}^2} = 0 \qquad (3\text{-}2)$$

which is the Laplace equation of two-dimensional, incompressible, hydrodynamics in the cross-flow plane ($\bar{x}$ = constant or plane normal to the free stream velocity). For motion of the body through a fluid at small angles of attack, the flow pattern in the cross-flow plane

---

1 A complete list of symbols is given in the List of Symbols at the beginning of this report.

can be considered identical to the flow pattern in a normal plane, or plane normal to the axis of the body. For purposes of analysis of the vortex-shedding characteristics, an $x$, $y$, $z$ axis system oriented with respect to the body will be used, as defined in Figure 5. The subject of slender-body theory as it pertains to analysis of flow over bodies of revolution and vortex shedding at angle of attack is discussed in more detail in Reference 13, Chapters 3 and 4, respectively.

The major assumption involved in slender-body theory is that the flow in any normal plane is independent of the flow in any other normal plane. Figure 6 shows a body of revolution moving through a fluid with velocity $U$ at an angle of attack $\alpha$ such that separation and vortex shedding occur. If the normal plane shown in Figure 6 is considered to be fixed to and move with the body, then the two-dimensional steady flow pattern in this plane, as represented in the sketch below, is determined only by the flow and

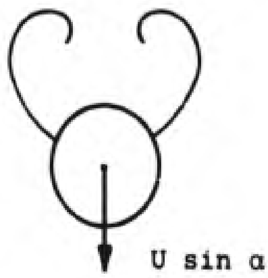


boundary conditions in this plane. Essentially, the three-dimensional curved vortex filaments making up the vortex sheets have been replaced by infinitely long, straight vortex filaments normal to the plane whose contributions to the flow in this plane are given only by their strength and position as they pass through this plane.

To determine the manner in which the vortex system changes between adjacent normal planes on the body, an analogy can be constructed between a three-dimensional, steady flow and a two-dimensional, unsteady flow. Again in Figure 6, consider the normal plane to be fixed in the fluid and allow the body to move through the plane with velocity $U$. The circle representing the body cross-section then moves downward in this plane with a velocity $U \sin \alpha$. As the axial station on the body where separation first appears moves through the plane, small vortex sheets appear at the separation points. As the body continues to move through the plane, these vortex sheets grow in length and begin to curl over the body. Thus, the steady vortex system can be considered a two-dimensional, unsteady growth of vortex sheets in a normal plane. Time in the unsteady problem may be related to distance along the body axis from the point of inception of separation by the velocity $U \cos \alpha$.

The selection of a flow model was governed primarily by the greater simplicity of analysis of the two-dimensional case. All of the techniques which have been developed for two-dimensional, incompressible potential flow-analysis can be used in the slender-body model. The image vortex system is more straightforward for a circle in two dimensions, and the method could be extended, if necessary, to non-circular cross sections by use of mapping techniques. It was felt that fewer empirical inputs would be required with the two-dimensional model, and that these would be perhaps more straightforward to obtain, particularly since there are no experimental vortex-shedding data available on bodies whose radius varies along the axis. On the other hand, the slender-body model does not consider the three-dimensional aspects of the vortex filaments, which could possibly have a appreciable effect on the results. In view of these considerations, it was decided that the initial analysis would be made with the slender-body model, and at a later time the limitations of the simplified model could be assessed and perhaps removed.

### 3.2 Analysis of the Flow Model

In the two-dimensional flow model just described, vortex sheets leave the body at separation points symmetrically located with respect to the vertical axis of symmetry, and roll up over the body. It is known (Ref. 6, for instance) that most of the vorticity in the sheet is concentrated in the rolled-up portion of the sheet. Therefore, without appreciable loss in accuracy, the vorticity in the sheet may be approximated by a single, concentrated vortex located at the "center of gravity" of the rolled-up sheet.

The flow model now has the characterisitcs indicated in Figure 7. The body is represented by a circle of radius $a$, which in the general case may vary with axial distance, $x$, along the body or time, $t$, in the unsteady analysis. Distance along the body from the point of initial separation is related to time as follows:

$$x - x_s = (U_\infty \cos \alpha)\ t \tag{3-3}$$

when zero time is defined by this relation. In this section, time will be considered the independent variable and the analog with distance will be understood. The coordinate system has the $y$, or real, axis horizontal and the $z$, or imaginary, axis vertical, positive $z$ upwards. Complex notation will be used for position. The problem is assumed to have symmetry about the $z$ axis. The body is taken to be stationary in a uniform flow of velocity $U_\infty$ whose component in the normal plane is $U_\infty \sin \alpha$ in the positive $z$ direction. At any given time there will be a vortex pair in the flow field, the right hand vortex having a strength $\Gamma$ and position $\zeta_1$. To cause the body surface to be a stream surface, there must be an image vortex within the body of equal strength and opposite sign, located at the inverse point. Separation is assumed to occur at the point $\zeta_0$ on the body, where, in general, $\zeta_0$ may change its angle, $\theta_0$, as well as its radius coordinate with time. A sheet of vanishingly small vorticity connects the separation point on the body with the vortex. This model and the analysis below follow the approach described by Bryson in Reference 14.

The complex potential for the flow of Figure 7 consists of the following terms:

(1) a uniform flow of velocity $U_\infty \sin \alpha$

(2) a doublet representing the body

(3) a vortex term for each of the two external and two image vortices

(4) a source representing the change in body radius with time.

The complex potential is then

$$W = -i\, U_\infty \sin\alpha \left(\zeta - \frac{a^2}{\zeta}\right) - i\, \frac{\Gamma}{2\pi} \ln\left(\frac{\zeta - \zeta_1}{\zeta - \frac{a^2}{\bar{\zeta}_1}} \; \frac{\zeta + \frac{a^2}{\zeta_1}}{\zeta + \bar{\zeta}_1}\right)$$

$$+ a\,\dot{a}\, \ln\zeta \qquad (3\text{-}4)$$

Appendix A contains more detail on the methods and conventions used to obtain Equation (3-4). The general expression for the complex velocity is given by the following expression:

$$\bar{V} = v - iw = -i\, U_\infty \sin\alpha \left(1 + \frac{a^2}{\zeta^2}\right)$$

$$- i\, \frac{\Gamma}{2\pi}\left(\frac{1}{\zeta - \zeta_1} + \frac{1}{\zeta + \frac{a^2}{\zeta_1}} - \frac{1}{\zeta - \frac{a^2}{\bar{\zeta}_1}} - \frac{1}{\zeta + \bar{\zeta}_1}\right) + \frac{a\,\dot{a}}{\zeta} \qquad (3\text{-}5)$$

The complex conjugate velocity at the right hand, external vortex $\bar{V}_1$ is obtained by letting $\zeta$ equal $\zeta_1$ in Equation (3-5) and dropping the singular term, since a vortex does not induce a velocity at its own center.

$$\bar{V}_1 = -i\, U_\infty \sin\alpha \left(1 - \frac{a^2}{\zeta_1^2}\right)$$

$$- i\, \frac{\Gamma}{2\pi}\left(\frac{1}{\zeta_1 + \frac{a^2}{\zeta_1}} - \frac{1}{\zeta_1 - \frac{a^2}{\bar{\zeta}_1}} - \frac{1}{\zeta_1 + \bar{\zeta}_1}\right) + \frac{a\,\dot{a}}{\zeta_1} \qquad (3\text{-}6)$$

A differential equation for the motion of the vortex pair may be obtained by considering the forces on the vortex and the sheet connecting the vortex to the separation point on the body. Theoretically, there should be zero force on the vortex and each element of length of the sheet. However, because all of the vorticity in the flow field has been lumped into the concentrated vortex and the strength of this vortex changes with time, a force is induced on the sheet. This force is given by

$$F_S = i \rho \dot{\Gamma} (\zeta_1 - \zeta_0) \tag{3-7}$$

The theoretical requirement of zero force on each element of vorticity in the flow field may be approximated by requiring zero net force on the entire vortex configuration in the flow field. With this requirement, there appears a force on the vortex which must be equal and opposite to the force on the sheet. The vortex force is given by

$$F_V = i \rho \Gamma (V_1 - \dot{\zeta}_1) \tag{3-8}$$

The derivation of Equations (3-7) and (3-8) is given in Appendix B. The condition of zero net force then requires $F_S = F_V$, or

$$i \rho \dot{\Gamma} (\zeta_1 - \zeta_0) = i \rho \Gamma (V_1 - \dot{\zeta}_1) \tag{3-9}$$

or rearranging this equation,

$$\dot{\zeta}_1 + (\zeta_1 - \zeta_0) \frac{\dot{\Gamma}}{\Gamma} = V_1 \tag{3-10}$$

Equation (3-10) is then a relation between the motion of the vortex, $\zeta_1$, its position and strength, and the velocity induced at its center by the other vortices and the flow over the body.

An additional relation is needed between the strength of the vortex and its position in the flow field. This relation is obtained from the condition that there is no flow in the normal plane along the surface of the body through the sheet at the separation point. Essentially, the separation point is a two-dimensional stagnation point. Mathematically, this condition is represented by letting

$\zeta$ equal $\zeta_o$ in Equation (3-5) and setting the complex velocity equal to the velocity of the surface of the body; that is

$$(v - iw)_{\zeta = \zeta_o} = \frac{a\,\dot{a}}{\zeta_o}$$

or

$$- i\, U_\infty \sin\alpha \left(1 + \frac{a^2}{\zeta_o^2}\right) - i\,\frac{\Gamma}{2\pi}\left(\frac{1}{\zeta_o - \zeta_1} + \frac{1}{\zeta_o + \frac{a^2}{\zeta_1}} - \frac{1}{\zeta_o - \frac{a^2}{\bar{\zeta}_1}} - \frac{1}{\zeta_o + \bar{\zeta}_1}\right) = 0 \qquad (3\text{-}11)$$

Equation (3-10), together with Equations (3-6) and (3-11) represents a nonlinear, first-order, ordinary differential equation for the variation of the complex vortex coordinate, $\zeta_1$, as a function of time. These equations can be solved for $\zeta_1(t)$ and $\Gamma(t)$, when the variations of $a$ and $\zeta_o$ with time are prescribed.

A force occurs on the body because of the motion of the vortices in the flow field downstream of the body. This force may be obtained in the following way. The impulse of a pair of vortices of equal but opposite strength is given by (Ref. 15, Para. 157).

$$I = i\,\rho\,\Gamma \text{ (distance between the pair)} \qquad (3\text{-}12)$$

Considering a vortex pair to consist of the external vortex at $\zeta_1$ and its image at $a^2/\bar{\zeta}_1$, and the other pair at $-\bar{\zeta}_1$, and $-a^2/\zeta_1$ Equation (3-12) becomes

$$I = i\,\rho\,\Gamma\left(\zeta_1 - \frac{a^2}{\bar{\zeta}_1} + \bar{\zeta}_1 - \frac{a^2}{\zeta_1}\right) \qquad (3\text{-}13)$$

The force on the entire flow configuration is given by the time rate of change of impulse of the two vortex pairs as given in Equation (3-13). Since the force on the flow field external to the body is set equal to zero by Equation (3-9), the force on the entire flow configuration is the force on the body. This force which can be considered the viscous normal force per unit length on the body, $dN_v/dx$, is given by

$$\frac{dN_v}{dx} = \frac{dI}{dt} = \frac{d}{dt}\left[ i\,\rho\,\Gamma \left( \zeta_1 + \bar{\zeta}_1 - \frac{a^2}{\bar{\zeta}_1} - \frac{a^2}{\zeta_1} \right) \right] \tag{3-14}$$

Since the impulse, Equation (3-13), is a pure imaginary number, the normal force unit length, Equation (3-14), is directed along the imaginary, or z, axis. Consequently, when the values $\Gamma$, $\dot{\Gamma}$, $\zeta_1$ and $\dot{\zeta}_1$ are known as a function of time, the distribution of normal force per unit length may be obtained as a function of time or, in the analogy, distance along the body from the origin of separation.

These relations, Equations (3-6), (3-10), (3-11), and (3-14), have been reduced in form and divided into real and imaginary parts to form two simultaneous differential equations with auxiliary relations. The equations were programmed for the Vidya IBM 1620 computer and integrated numerically using a Runge-Kutta method. These operations are discussed in detail in Appendix C.

### 3.3 General Characteristics of the Analysis

There are a number of additional factors that should be discussed in the application of the theory of Section 3.2 to a particular problem. It is the purpose of this section to discuss these factors and finally to describe the theory to a case in which some experimental data exist for purposes of comparison.

#### 3.3.1 Input and output of the computer program

The input information which is required to make a calculation on a typical case consists of the following items:

(1) the radius and rate of change of radius with length of the body as a function of axial distance from the nose

(2) the variation of the angular location of separation ($\theta_0$, as defined in Fig. 7) with axial distance along the body

(3) the body length, maximum radius, a point about which moments may be taken, and the axial location on the body at which separation first appears

(4) the angle of attack, the density of the fluid, and free-stream velocity

(5) the time increment for the finite difference integration procedure

(6) the coordinates of the starting position of the vortex as it leaves the body surface. (See Section 3.3.2.)

The program computes stepwise the motion and strength of the vortex pair and the viscous normal force per unit length induced on the body. The output of the program consists of the values, at the axial distances from the point of origin of separation corresponding to the successive time increments of the computation, of vortex position, vortex strength, the viscous normal force per unit length, and the viscous cross-flow drag coefficient. The pitching moment about the assumed center and the pitching-moment coefficient are presented at the end of the computation.

3.3.2 Starting the computation

The separation point on the body is a singular point in the differential equation for the motion of the vortex, Equation (3-10). At this point, $\zeta_1$ equals $\zeta_0$ and $\Gamma$ is zero. The second term of Equation (3-10) is then of the form zero/zero and cannot be handled by the computing machine. This problem has been resolved by starting the computation on the machine with the vortex a small distance away from the separation point in the flow field.

In Reference 14, an analysis was made of the behavior of the vortex very close to the separation point. The approach used was to let $\zeta_1 - \zeta_0 = \rho a e^{i\phi}$, where $\rho << 1$, and determine the characteristics of $\phi$ as $\rho$ approached zero. It was found that the vortex leaves the separation point along a line that is oriented $30^{\circ}$ from the downstream tangent to the cylinder at the separation point, as shown in the sketch

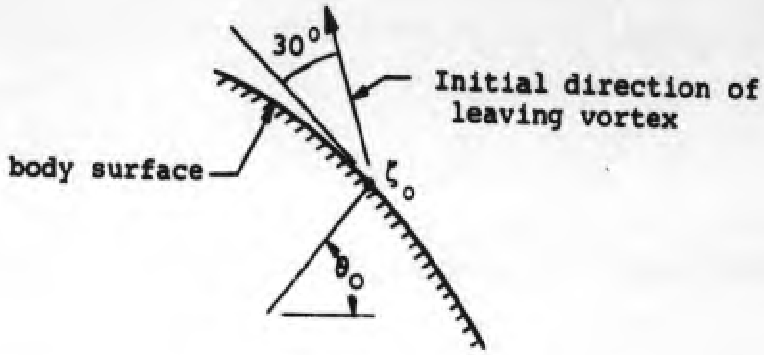


The sensitivity of the results of a computation to the location of the starting point was investigated by running the same case with different starting points. For the case of separation from a cylinder of unit radius at a given angle of attack and free-stream velocity, the following starting points were used:

(1) a point on the 30° line at a radius of 1.05
(2) a point on the 30° line at a radius of 1.025
(3) a point on the radius, $\theta_o$ = constant, at a radius of 1.05

The vortex path and strength variation for cases 1 and 2 were found to be identical beyond a radius of 1.05, because the path of the vortex with starting condition 2 essentially passed through the starting position of condition 1. The vortex path of condition 3 very rapidly approached the vortex paths of conditions 1 and 2, and beyond a radius of approximately 1.07, the vortex motion in the three paths were identical. Since the vortex velocity and strength are a function only of its position, the induced force distribution on the body is also identical. The only basic difference between the computations is the time required for the vortex to reach the point where the paths in the flow field become identical. Conditions 1 and 3 had essentially the same time and condition 2 had a somewhat longer time. The vortices tend to move away from the separation point more slowly as they are started closer to the separation point, because the forces and velocities tending to move the vortex go to zero at the separation point. These time differences have the effect of shifting the force distribution axially along the body a distance equivalent, in the analog, to the difference in time.

In the actual flow field, there is no vortex filament motion. The flow is steady, and the flow velocities and induced forces are given by the contributions of all of the vortex filaments. Consequently, the difficulty associated with starting the vortex in the two-dimensional case is the result of representing a steady phenomenon by an unsteady flow model. From a practical standpoint, so little is known of the region on the body where separation originates that it would seem reasonable to select a starting condition such that the uncertainty in the origin of the force distribution is minimized. This has been done in the calculations made by using a radius of 1.05 on the $30^{\circ}$ line in all cases. No further investigation of this problem was made during this study. The representation of this phenomenon needs to be studied, however, in connection with an improved flow model to attempt to obtain a precise definition of the origin of separation induced forces.

3.3.3 Empirical inputs to the computation

It was indicated in Section 3.3.1 that the required input data for a computation include the angular location of separation, $\theta_0$, as a function of distance along the body and the axial location, $x_s$, where separation first occurs on the body. The determination of these two values is controlled primarily by the boundary-layer characteristics on the inclined body which, in turn, are affected by the body shape, the Reynolds number, the angle of attack, the presence of appendages on the body, and less importantly by free-stream turbulence and surface roughness. At the present time, there is no satisfactory analytical method of predicting separation of a turbulent boundary layer on an inclined body of revolution. Work is in progress along these lines, but the problem is exceedingly difficult because of the lack of fundamental knowledge of turbulent boundary layers. Consequently, for purposes of this work, experimental data have been used as a guide in selecting values of $\theta_o$ and $x_s$ to be used. The major sources of data are References 1 to 6.

The axial location at which separation first appears has been generally determined by circumferential static pressure distributions taken at different axial stations on a test configuration. A typical set of measurements is shown in Figure 8, taken from Reference 6. The curve for the axial station 3.32 diameters downstream of the nose is typical of a nonseparated case in that the pressure falls to a minimum close to the maximum thickness point and rises steadily beyond the minimum. The curve for the station 4.06 diameters downstream shows a second minimum at an angle of about 50$^{\circ}$, which is typical of a separated pressure profile. In this case, separation is assumed to originate somewhere between these two axial stations. Generally, the data for $x_s$ are shown as a band rather than a line, because of this uncertainty between two measuring stations.

A collection of data on the origin of separation, based on the above method of estimation, is shown in Figure 9. These data all show the characteristics of no perceptable separation at low angles of attack and the axial location of separation moving forward with increasing angle of attack. The test configurations in these cases were cylinders with either a cone or ogive nose. It would be expected with a pointed nose that at some angle of attack separation would begin to occur at the nose. Jorgensen (Ref. 17) and Moore (Ref. 18) have shown this to be the case for a cone, and Moore indicates separation occurring at the nose for an angle of attack equal approximately to the cone semivertex angle. For the case of the Mello data (Ref. 6) in Figure 9, this would occur at an angle of attack of about 15$^{\circ}$. If the same sort of results were applicable to the ogive, separation would begin to occur at the nose of the ogives of References 1 and 5 at an angle of attack of approximately 20$^{\circ}$.

These results indicate that the important characteristics determining the axial location at which separation first appears on the leeward side of an inclined body include angle of attack, the shape of the nose, and probably Reynolds number, although there are not sufficient experimental data to determine any consistent variations with Reynolds number.

The angular location of the separation line at a given axial station is also determined experimentally by the characteristics of the circumferential pressure distribution. In the normal plane, the flow along the body surface approaches the separation point from both the upstream and downstream directions and decelerates as it nears the separation point. Thus, the static pressure would be expected to rise as the separation point is approached from either side. This characteristic is shown in Figure 8 for the 4.06 axial station, and the value of $\theta_o$ is generally taken as the angular location of the maximum in the pressure curve downstream of the first minimum. In the curve of Figure 8, this maximum occurs at a $\theta_o$ of $25^\circ$, approximately. Data obtained using this criterion are shown in Figures 10(a) and 10(b) as a function of distance along the body from the point of origin of separation. In each case the center of the band for $x_s$ was used as the point of origin of separation. The data are from References 1, 3, 5, and 6, and were all taken on the cylindrical portion of the test body. There is a large variation in the observed values of $\theta_o$; however, the following observations may be made. The value of $\theta_o$ for the case of an infinite cylinder normal to an incompressible flow with turbulent separation is approximately $50^\circ$. The data which fall closest to this value are the data of Reference 5 for a Mach number of 0.3, Figure 10(b). The other data were taken at supersonic Mach numbers and tend to give lower values of $\theta_o$, particularly at high angle of attack. It is possible for the cases involving supersonic flow that the disturbances, in the form of compression and expansion waves, induced by separation at one axial station may induce instability in the boundary layer at lower values of $\theta$ downstream so as to give the decrease in $\theta_o$ with axial distance indicated by the data. A comparison of the two sets of data from Reference 5 at different Reynolds numbers indicates a small decrease in $\theta_o$ with increasing Reynolds number at a given distance aft of the origin of separation. It would also appear that $\theta_o$ tends to decrease somewhat with increasing angle of attack. It is evident, however, that insufficient data exists on which to base any empirical relationships regarding the variation of $\theta_o$ with angle of attack or Reynolds number. The data of Figure 10 were used as a guide in the calculations made.

3.3.4 Characteristics of the solution

A number of computations were made on a pointed cylinder inclined to the flow, where separation was first assumed to occur on the cylinder rather than on the forebody. These computations served two purposes. First, the basic characteristics of the flow and vortex motion are more clearly indicated, because the effect of a varying body radius does not enter. Second, the experimental work on vortex shedding has been done primarily with inclined cylinders with cone or ogive forebodies, and the experimental results may be compared with theoretical predictions for vortex position and strength and viscous normal force distribution.

A computation was made on a cylinder of unit radius inclined at an angle of $20^\circ$ to free-stream flow assuming the angular location of separation, $\theta_o$, to be constant with length. The results of this computation are indicated in Figures 11, 12, and 13. Figure 11(a) shows the position of the vortex in the flow field as a function of distance along the body from the origin of separation (or time, in the analogy). Equal distance increments are noted on the vortex path. The value of $\theta_o$ is $40^\circ$, and the vortex was started on the $30^\circ$ line as described in Section 3.3.2. Since the vortex follows essentially a vertical trajectory after it leaves the surface, the force on the sheet, and therefore the force on the vortex (Appendix B), is horizontal. Under these conditions, the vortex tends to move horizontally with the local velocity and vertically with a velocity relative to the local velocity given by the force conditions. This can also be seen from Equation (3-10), Section 3.2, where the real part of the quantity $(\dot{\zeta}_1 - \zeta_0)$ is very small, and the real part of $\dot{\zeta}_1$ is essentially equal to the real part of $V_1$. With increasing distance (or time), the vortex approaches the Föppl curve, which is a locus of points at which a symmetric vortex pair may exist at rest downstream of a cylinder immersed in uniform flow (see, for instance, Ref. 12 or 13 for a detailed discussion of the Föppl curve). The distance increments noted on the curve show the vortex accelerating as it leaves the body and then decelerating as it approaches the Föppl curve.

The asymptotic behavior of the vortex is indicated in Figure 11(b) which shows an enlargement of a portion of the Föppl curve. Noted on the Föppl curve are three values of vortex strength, $\Gamma/2\pi a\, U_\infty\, \alpha$. Noted also is a point on the Föppl curve marked $\theta_o = 40^\circ$ which is determined by the simultaneous solution of the Föppl equations (Equations (4-82) and (4-83), Ref. 13) and the boundary conditions represented by Equation (3-11). This point is the location of one vortex of a symmetric pair whose strength is such as to cause zero induced velocity at the point and zero velocity along the body at the separation point. Values of $(x - x_s)/a$ are noted on the vortex trajectory and at the last value noted (60), the strength is given. The vortex appears to be spiraling in toward the point, $\theta_o = 40^\circ$. Ultimately, the vortex will reach this point, at which time its motion and change in strength ceases. For $(x - x_s)/a > 30$, the strength begins to decrease slightly. As a result, the viscous normal force becomes negative.

One limitation with the two-dimensional, unsteady-flow model is apparent in the asymptotic behavior of the vortex pair. For a vortex pair downstream of an infinite cylinder in two-dimensional flow, the Föppl curve is the locus of points at which there is a zero induced velocity at the vortex center, that is, the velocity contributions of the other external vortex, the two image vortices and the flow around the cylinder exactly cancel. In the real case, no such condition would be expected to exist because of the three-dimensional nature of the vortex filaments. The body should continue to sustain a viscous normal force, feed vorticity into the flow field, and cause the vortex sheets to grow continuously in strength. The behavior predicted by the theory for the vortex close to the Föppl curve corresponds to either a very long body (a separated length of 12 diameters or more) or very high angle of attack, since the parameter of interest is $(x - x_s)\alpha/a$. In the latter case, as $\alpha$ increases, the flow must ultimately approach the two-dimensional case (neglecting end effects) in which the Föppl phenomenon does exist. In the former case, practical bodies of interest generally have fineness ratios less than about 12. Consequently, there are no experimental data to indicate what the asymptotic behavior of the vortices or vortex induced forces should be, although the data of Figure 17, which are discussed later, show a decreasing trend in viscous cross-flow drag near the end of the body. It is possible that on bodies having very long separated regions, the approach of the vortex to the Föppl curve in the theory is associated with a tearing of the sheet and formation of a new sheet. This is a subject that needs additional investigation.

Figure 12 shows the variation of vortex strength with distance along the body. The strength increases gradually as the vortex moves away from the body in order to maintain the zero tangential velocity at the separation point on the body (Equation (3-11), Section 3.2). As the vortex approaches the Föppl curve and decelerates, the strength increases less rapidly and approaches a constant value at a large distance along the body given by the Föppl condition. The apparent non-zero value at $x - x_s$ is caused by the starting problem described in Section 3.3.2.

Figure 13 shows the force distribution induced on the cylinder by the vortex motion. The viscous cross-flow drag coefficient is the viscous normal force per unit length divided by the cross-flow dynamic head and diameter. The viscous normal force per unit length is proportional to the rate of change of vortex strength and position with distance (Eq. (C-11), Appendix C) and therefore increases as the vortex accelerates away from the body. As the vortex begins to decelerate, $C_{D_{C_V}}$ reaches a maximum and begins to decrease. At large x, $C_{D_{C_V}}$ will approach zero since the vortex approaches a constant strength and position, as shown in Figure 13.

In Section 3.3.3 it was noted that a considerable variation in $\theta_o$ exists in the available experimental data. In order to determine the sensitivity of the results of the computation to the value of $\theta_o$ used, calculations were made for the above configuration and flow using values of $25^o$ and $50^o$. The results for viscous cross-flow drag coefficient are shown in Figure 14. The three curves are similar in that each rises to a maximum and then falls off with increasing distance. The maximum value and the axial location of the maximum are quite different, however. Since the viscous normal force per unit length is proportional to the vortex velocity, it would be expected that $dN_V/dx$, and $C_{D_{C_V}}$ would be highest for the case of the separation point closest to the maximum thickness point, or $\theta = 0$, because the flow velocities in the normal plane are highest at this point. Furthermore, since the vortex must travel a longer distance in the normal plane to reach the Föppl curve, the peak of the $C_{D_{C_V}}$ curve should occur at larger values of time, or axial distance, with decreasing $\theta_o$. Both of these trends are evident in Figure 14. These calculations indicate the importance of defining reasonably well the location of the separation line on the body.

### 3.3.5 Comparison of theory with data

A calculation was made on an ogive cylinder to compare the results of a theoretical computation with experimental results. The body geometry and data used were those of Reference 5, since this was the only set of complete vortex measurement data for a low speed flow. The body is a cylinder with a tangent ogive forebody three diameters long. The overall length is 10.74 diameters. The data used were those for a Mach number of 0.3, a Reynolds number based on free-stream conditions and cylinder diameter of $3\times10^6$, and an angle of attack of $20^\circ$. A number of circumferential body static pressure measurements were made on the forebody as well as the cylinder. These measurements indicated separation first occurring between 2 and 3 diameters downstream of the nose for $\alpha = 20^\circ$, as indicated in Figure 9 of Reference 5. In the following discussion, separation is assumed to occur at 2.5 diameters. It should be indicated that at this angle of attack, there is a possibility of separation originating at the nose. This is not observable in the pressure measurements taken at the 0.5-diameter station, although it would probably be difficult to detect with pressure measurements alone.

The data for vortex position, strength, and cross-flow drag coefficient were correlated on the basis of a non-dimensional distance along the body from the point of separation, $(x - x_s)\alpha/a$, and are shown in Figures 15, 16, and 17. The data on the angular location in a normal plane of the separation line were taken from Figure 6 of Reference 5 and are shown in Figure 10(b). Although it is difficult to read $\theta_o$ from Figure 6 with any great accuracy, it appeared that $\theta_o$ was approximately constant at $40^\circ$ for $\alpha = 20^\circ$.

Figure 15 shows the $y$ and $z$ coordinates of the vortex core as a function of axial distance from the origin of separation. Data are available only at two axial stations on the body. The $z$ coordinate theory is in general agreement with the data. The $y$ coordinate theory, however, does not agree with the data. The data, with $\theta_o = 40^\circ$, show an appreciable movement of the vortices toward the vertical plane of symmetry which is not predicted by the theory. These data tend to be different in this respect from the supersonic flow data of References, 1, 6, and 8, which indicates values of $y/a$ of the order of 0.6 to 0.75. Since Reference 5 contains the only low-speed data on vortex position, it is not known whether these data are typical of the low-speed case or not.

Figure 16 shows vortex strength as a function of distance along the body. The data were deduced by the authors from a normal force distribution obtained from static pressure data on the periphery of the body at various stations. Figure 18, taken from Reference 5, shows the total normal force distribution for $\alpha = 20^\circ$. To obtain that portion of the normal force attributable to separation and vortex shedding, the forces predicted by slender-body theory with no separation (shown in Figure 18 by the dashed line) were subtracted from the total forces and the balance used to calculate the vortex strength. The authors used Equations (C-12) and (3-13) and the measured vortex positions for this calculation. Since there is generally some normal force carryover from the forebody onto the cylinder which is not predicted by slender-body theory, the forces attributed to vortex separation near the ogive-cylinder junction, and consequently the computed vortex strength, are liable to be somewhat high using this technique. The theory agrees quite well with the data except for the point nearest the origin, which might be subject to the above comments. Since the computation of vortex strength and normal force is much more sensititive to $z$ position than is $y$ position, the lack of agreement on $y$ position shown in Figure 15 is not significant.

Figure 17 shows viscous cross-flow drag coefficient as a function of distance along the body. The data were obtained from Figure 7 of Reference 5 in the manner described above. The theory and data tend to have the same trend in that the drag coefficient rises to a maximum and then decreases with distance along the body. The maximum value is predicted reasonably well, but the theoretical rate of rise is much more gradual than is indicated by the data. As was indicated previously, it is possible that the authors, using this technique, would predict too high a $C_{D_{C_V}}$ near the ogive-cylinder shoulder.

The comparisons that have been made indicate that the theory correctly describes the general characteristics of vortex motion due to separation on the leeward side of an inclined body of revolution. There are, however, considerable discrepancies having to do with the area near the origin of separation on the body and the lateral, or $y$, behavior of the vortex center, which may be due in part to difficulties associated with obtaining and reducing the experimental data as well as an inadequacy in the theory.

3.4 Application of the Analysis to a Submarine

The previous sections have described a method of obtaining the force distribution on an inclined body of revolution induced by flow separation on the leeward side of the body. In this section, the use of this method in connection with determining the total normal forces and pitching moments on a submarine at angle of attack is discussed.

The physical characteristics of a modern, high-speed submarine were discussed in Section 2. It was indicated that, for purposes of this study, the assumed configuration would consist of a hull which is a slender body of revolution and stern control surfaces.

The discussion on force distribution can be divided into those forces which would exist in the absence of separation at relatively low angles of attack and the forces induced by separation at high angles of attack. At small angles of attack, the normal force distribution on the hull is determined by the pressure distribution, which is a function of the hull shape. Since the hull is relatively slender, slender-body theory should be applicable and may be used to obtain the normal force distribution. The resulting expression for normal force per unit length is

$$\frac{dN}{dx} = 2\alpha\, q_\infty \frac{dS}{dx} \tag{3-15}$$

For no boundary layer, $dS/dx$ is the variation of the hull cross section area with length. The resulting normal force distribution is somewhat as follows:

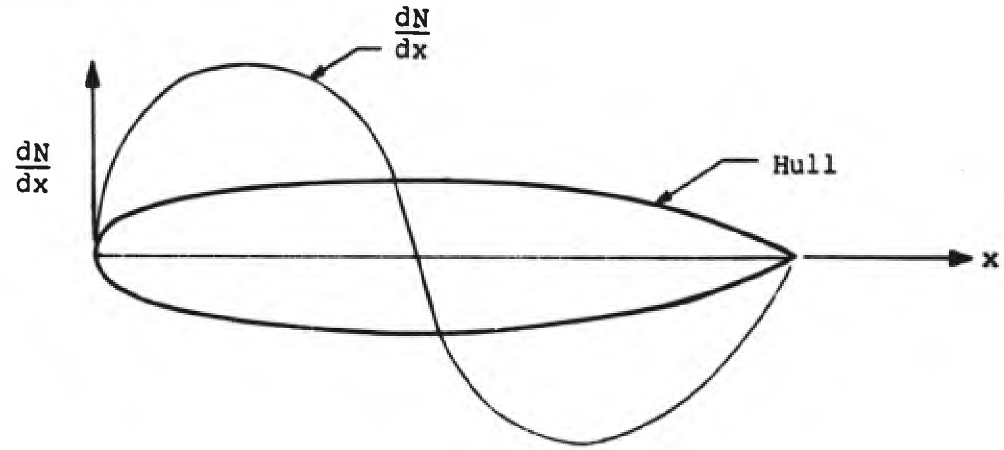


An upward (shown positive in the sketch) normal force exists aft to the station of maximum thickness, and a downward force exists aft of the maximum thickness point. It can be seen from Equation (3-15) that the net normal force for zero base area is zero; that is, the upward force forward just equals the downward force aft. Both regions, however, contribute to a nose-up pitching moment.

The presence of a boundary layer causes an "effective" hull shape to exist which is only slightly different from the real hull over most of the hull length but is appreciably different near the stern. At the stern, separation is likely due to the adverse pressure gradient. The sketch below illustrates the possible flow configurations:

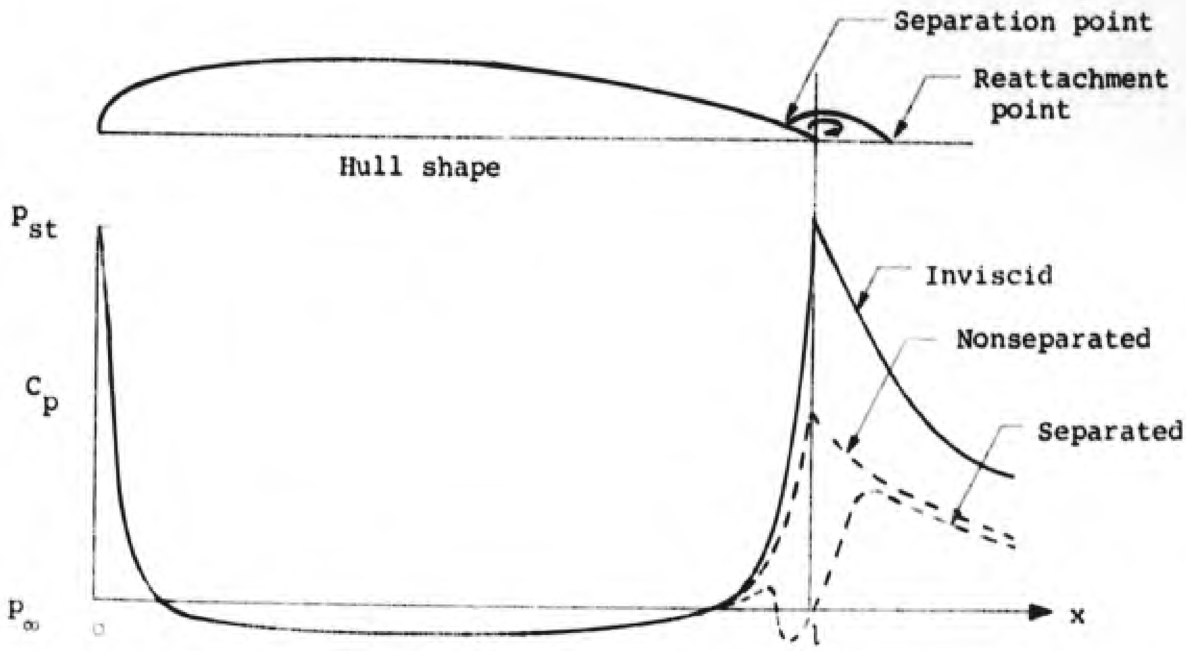


For inviscid flow, the pressure distribution is as indicated. A stagnation point exists at the rear with the free-stream stagnation pressure. Downstream of the body, the pressure decreases to $p_\infty$ as the velocity becomes parallel and uniform. For flow with a boundary layer and no separation, the pressure curve is essentially the same up to approximately the 90-percent station. At this point, the pressure rises to a stagnation value at the stern which reflects the losses in the boundary layer. Downstream, the pressure again falls off to $p_\infty$. If separation occurs on the body, a region of back flow exists at the stern. The pressure then falls from the stern forward a short distance to cause the forward flow along the surface and then rises to turn the flow out and rearward at the separation point. The stagnation condition now occurs downstream of the body at the reattachment point, beyond which the pressure drops to $p_\infty$ ultimately. It is interesting to note that the trend indicated by the separated curve is evident in the towed model and ship data of Reference 24.

Equation (3-15) may be applied to the hull with boundary layer up to perhaps the 90-percent station to get normal-force distribution. In this case, however, the net normal force is dominated by the boundary-layer effects at the stern. As a first approximation to these effects, an effective base area could be assumed for use with Equation (3-15). This is done in Section 5.3 to get the hull-alone normal force. However, since this method does not try to represent the flow phenomenon near the stern, any agreement with data would be fortuitous. For pitching moment, the flow phenomenon near the stern has a much smaller effect, since the force distributions are additive.

At angle of attack the stern planes will develop lift. For purposes of determining this effect, data on lift coefficient versus angle of attack were obtained for a typical submarine plane configuration from Reference 19. The lift on the stern planes in the presence of the hull and the lift carryover onto the hull were obtained as a function of stern plane geometry and stern plane alone lift coefficient using the methods of Reference 20 and the K factors[2] given by slender-body theory.

As the angle of attack increases, a condition will be reached in which separation on the leeward side of the hull will occur. The pressure distribution and flow around the hull are changed considerably over the non-separated case. Allen, in Reference 4, proposed a method of predicting the force distribution for a slender body under such flow conditions which consists of adding the local non-separated normal force (Equation (3-15)) to the local viscous normal force. This procedure has been widely accepted and will be used herein.

The effect of hull separation and vortex shedding on the forces on the stern planes may be obtained by considering the downwash on the planes induced by the body vortices as they pass over the stern planes. At the stern planes, the flow appears as follows:

---

[2] The K factor is defined as the ratio of the lift of the tail or body in the presence of the other to the lift of the tail alone.

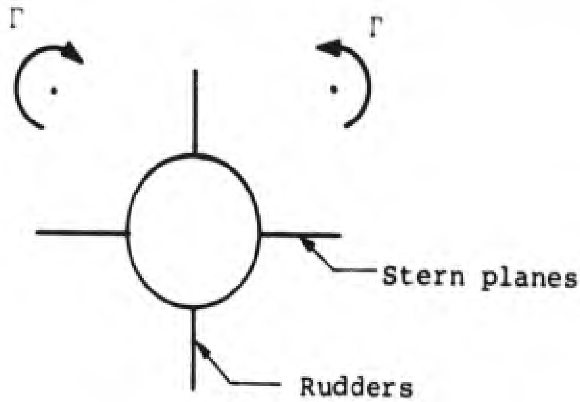


The downwash is determined by the position and strength of the vortices as they pass over the stern planes. These factors are known at the leading edge of the planes from the hull separation analysis. However, to determine the way in which the vortices move in the presence of the stern planes is a different and more difficult analysis. Since this interaction is not a large effect, it has been assumed that the vortices move in this region as if the stern planes were not present, and the vortex interference forces on the planes are characterized by the vortex strength and position at the 50-percent-chord point as determined from the hull separation analysis. The effects of this assumption on the end results are felt to be negligible, since the vortex interference force itself is a small part of the total force on the submarine. The method of computing this force follows that given in Reference 20. A tail interference factor is obtained as a function of vortex position in relation to the span and planform. A ratio of the interference force to the lift of the stern planes alone may then be obtained using the interference factor and the vortex strength. Since the flow is symmetrical about the vertical plane through the hull axis, no forces are induced on the rudders. For computing moments the stern plane forces are considered to act at the quarter chord.

The hull separation analysis requires empirical inputs for $x_s$ and $\theta_o$. Figures 9 and 10 show such data for a number of conditions. These data are deficient for submarine hull purposes in that the Reynolds number based on diameter is low by one to two orders of magnitude and the effect of varying body radius on $\theta_o$ is not shown. In addition,there may be practical considerations, such as the effect of the bridge fairwater or the deck on the location of separation, that would override any Reynolds number or hull curvature effects. In making the computations described in Section 5, the data of Figures 9 and 10 were used as a guide and modified in certain cases by hull geometry effects.

Finally, it is noted that the contributions to the normal force and pitching moment given by potential theory for no separation are linear in $\alpha$, both for the hull and the stern planes. Thus, the departure from linearity of the theoretical force and moment curves is due to flow separation effects, and it is assumed that such is also the case for the experimental results.

3.5 Flow Stability Considerations

An analogy between steady, three-dimensional flow with vortex shedding on an inclined body of revolution and unsteady, two-dimensional flow with vortex motion about an infinite cylinder has been described. This analogy is further discussed with reference to the stability of the vortex motion in this section.

For the case of an infinite cylinder normal to a steady, uniform, incompressible flow, various flow configurations are possible, depending on the Reynolds number (see, for instance, Ref. 21). The resulting experimental drag coefficient per unit length is shown in Figure 19 (taken from Ref. 21) as a function of Reynolds number based on diameter. At Reynolds numbers below approximately 20, completely viscous flow exists with no separation. The drag coefficient in this range of Reynolds numbers is in excess of 2.5. In the Reynolds number range of approximately 20 to 100, separation exists, and a steady symmetric vortex pair is observed to exist downstream of the cylinder. The drag coefficient in this region ranges from about 2.5 down to 1.4. At a Reynolds number of approximately 100, instability occurs in the flow, and vortices are shed alternately from either side of the cylinder. The frequency of shedding (Strouhal number) increases as the Reynolds number is increased. The drag coefficient ranges from 1.0 to 1.4, approximately, in the range of Reynolds number up to $5 \times 10^5$. At this point, boundary-layer transition from laminar to turbulent flow occurs before separation. Since a turbulent boundary layer is able to support a greater adverse pressure gradient without separation than a laminar boundary layer, the separation point moves rearward, and an abrupt decrease in drag coefficient occurs. At higher Reynolds numbers, the flow is essentially completely turbulent in the wake, no well-defined vortices exist, and the drag coefficient is approximately constant in the range 0.3 to 0.4.

In the three-dimensional case of the inclined body, a steady, symmetric vortex pair has been observed experimentally to exist at cross-flow Reynolds numbers (defined with the normal component of free stream velocity and diameter) in the range $10^5$ to $10^6$. Since this configuration corresponds to the two-dimensional case of Reynolds numbers of the order of 50 to 100, the difference between the flows is apparently caused by the stabilizing influence of the axial flow component in the three-dimensional case. One might expect, however, that in the three-dimensional case, as the angle of attack is increased, the flow would change from a steady to an unsteady configuration as ultimately the two-dimensional case is reached. One might also expect that as the Reynolds number is increased in the three-dimensional case, instability might begin to occur, in which case the vortex sheets might begin to "tear" and cause alternate shedding and reformation of the vortices.

The angle-of-attack effect has been observed experimentally in References 2, 4, and 7. By means of smoke-and vapor-screen techniques, it has been observed that the flow progresses through three stages as the angle of attack is increased. In the first stage, a steady symmetric vortex pair exists over the leeward side of the body. At somewhat higher angles of attack, a steady asymmetric vortex configuration results as shown conceptually in the sketch below:

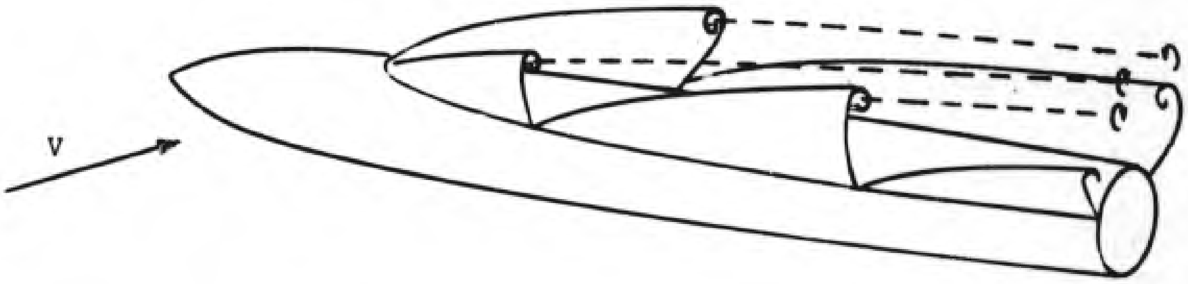


A vortex sheet on one side "tears" and forms a free vortex which then moves downstream as a second vortex forms at the separation line. On the opposite side the first sheet "tears" further aft along the body to form a free vortex and a new bound vortex so that, at any cross section, asymmetry exists. Because the flow remains steady, the force distribution is steady. However, the lack of symmetry causes local side forces to exist, as observed, for instance, in the investigation of Reference 22. At still higher angles of attack, the flow becomes unsteady, as in the two-dimensional case, and vortices are shed alternately from either side at a given station. The angles of attack at which the asymmetric steady- and unsteady-flow configurations occurred were found to be affected by the shape or bluntness of the forebody and also by forcing or controlling separation on the sides of the body using separation strips.

The Reynolds number effect on the transition between these three flow regions is essentially unknown. Reference 2 indicates a decrease in the angle of attack at which flow unsteadiness occurs with an increase in Reynolds number for one set of tests. In general, however, a large variation in Reynolds number has not been available in the experimental facilities in which the tests have been made, and no systematic set of tests has been made to investigate the effect of this parameter.

A knowledge of the characteristics of three-dimensional boundary layers is essential to an understanding of the effect of Reynolds number, angle of attack, body shape, and perhaps other factors on stability of the separated flow on the leeward side of an inclined body. Because this area is largely unknown, particularly for turbulent boundary-layers, it is not possible to draw any conclusions from the existing experimental results on the stability of the flow over a submarine at high angles of attack. Consequently, it has been assumed in this study that the flow can be characterized by a steady symmetric-vortex system on the leeward side.

## 4. ZERO ANGLE-OF-ATTACK STUDY

A submarine, because of its size, develops a boundary layer of considerable thickness on the aft portion of its hull. This thick boundary layer may have several effects on the forces and moments on the submarine. Although the primary emphasis in this study has been on the effects induced by separation at high angle of attack, it was considered desirable to investigate to some extent these boundary-layer effects on the forces and moments.

### 4.1 Boundary-Layer Characteristics

A submarine operates at a very high Reynolds number, because of the low kinematic viscosity of water. A typical value of Reynolds number is the order of $5\times10^8$, based on length. Since transition occurs at a Reynolds number of the order of $10^6$, a turbulent boundary layer exists over more than 95 percent of the length of the submarine.

The hull of a high-speed submarine is usually basically a body of revolution having a rounded nose, a relatively small curvature in the axial direction over most of its length, and a pointed tail. Near the nose, the axial curvature induces a negative pressure gradient which thins the boundary layer. Near the stern, the positive pressure gradient tends to thicken and destabilize the boundary layer. In addition, in this region, the boundary-layer thickness becomes appreciable compared to the radius of the hull, which further tends to thicken the layer. At the stern, separation is likely and a wake is shed.

The boundary-layer characteristics near the stern are affected considerably by the propeller. The propeller operates to a large extent submerged in the wake and tends to accelerate the low-velocity fluid which, in turn, reduces the effective thickness of the boundary-layer wake. This flow field is quite difficult to analyze theoretically, although the problem is being studied (Refs. 23 and 24).

The effect of angle of attack on the boundary layer is to create a cross flow over the hull from the windward to the leeward side. As a result, the boundary layer is thinned on the windward side and thickened on the leeward side. Reference 25 shows some experimental data taken in the Langley full-scale wind tunnel on an early high-speed submarine hull model without propeller over an angle-of-attack range of $\pm 6^\circ$. The data indicate a factor of 3 change in thickness on the top centerline near the stern in going from $+5.7^\circ$ to $-6.3^\circ$ angle of attack.

These boundary-layer characteristics have several effects on the forces and moments on the submarine. In the case of the hull, the boundary layer "displaces" the inviscid flow somewhat and causes a change in the pressure distribution over that which would exist in the absence of a boundary layer. This effect, which is appreciable only near the stern, creates a profile drag which would otherwise not exist. At small angles of attack, the thick boundary layer and wake become asymmetric with respect to the hull axis and cause a normal force to exist on the hull (this subject is further discussed in Section 5.3). In the case of the control and stabilizing surfaces at the stern, the boundary layer tends to partially blanket these surfaces in a low velocity fluid. Since the forces induced on these surfaces are proportional to the local dynamic pressure, these forces tend to be reduced due to the presence of the boundary layer. Furthermore, at angle of attack, the leeward surface is affected to a greater extent than the windward surface so that the action of the rudders at angle of attack, for instance, would induce a rolling moment as well as a yawing moment. The significance of these effects may be estimated by determining the boundary-layer thickness and velocity-profile characteristics on the hull.

### 4.2 Boundary-Layer Calculation Methods

Several methods have been developed for determining the characteristics of an incompressible, turbulent boundary layer on a body of revolution in axisymmetric flow. The problem of the three-dimensional, turbulent boundary layer, however, is extremely difficult to solve, and no methods are available at the present time. Consequently, the analytical work under this study has been limited to the zero angle-of-attack case.

The various methods for predicting the characteristics of an axisymmetric, turbulent boundary-layer utilize one or more forms derived from the general integral form of the boundary-layer equation, which can be written, for $\delta << \alpha$, following Reference 29,

$$\int_0^\delta u \frac{\partial u}{\partial x} u^c y^b \, dy + \int_0^\delta v \frac{\partial u}{\partial y} u^c y^b \, dy =$$

$$\frac{1}{\rho} \int_0^\delta \frac{dp}{dx} u^c y^b \, dy + \frac{1}{\rho} \int_0^\delta \frac{\partial \tau}{\partial y} u^c y^b \, dy \qquad (4\text{-}1)$$

This equation, together with the continuity equation and the definitions of momentum and displacement thickness, yields a relation between the variation of the boundary-layer thicknesses, the axial pressure gradient, and the shear stress. It has been shown (Ref. 26, for instance) that experimental velocity profiles can be represented by a one-parameter family of curves, where one form of this parameter is the ratio of displacement to momentum thickness, H. If this parameter is used and values of c and b in Equation (4-1) are assumed to be zero, for instance, the von Kármán momentum integral equation results,

$$\frac{d(\theta a)}{dx} + (H + 2)\frac{\theta a}{U}\frac{dU}{dx} = a\frac{\tau_w}{\rho U^2} \tag{4-2}$$

To completely define the problem, additional relations are required for the variation of H and shear stress with x and pressure gradient. Because of the difficulty in describing the turbulent boundary layer theoretically, empirical relations for H and $\tau$ have been used by the various investigators.

The methods that were considered were those of von Doenhoff and Tetervin (Ref. 26), Garner (Ref. 27), Truckenbrodt (Ref. 28), and Granville (Ref. 29). A good discussion of these methods (except that of Truckenbrodt) and the earlier work leading to these methods is given in Reference 29. Both von Doenhoff and Garner used the von Kármán form of the integral equation, Equation (4-2), and flat plate, empirical relationships for the variation of the wall shear stress with Reynolds number based on momentum thickness. Both used substantially the same experimental data, primarily, boundary-layer surveys on airfoils at momentum thickness Reynolds numbers up to the order of $5\times10^4$, to obtain a relationship of the form

$$\frac{dH}{dx} = f\left(\theta, H, \frac{dp}{dx}, \tau_w\right)$$

These three relations (integral equation, wall shear stress, and dH/dx relation) are then solved simultaneously to obtain the variation of momentum thickness and shape factor with length.

Truckenbrodt used the form of Equation (4-1) obtained with $c = 1$, $b = 0$. This relation, together with the continuity equation and the definition of the energy thickness, yields an "energy" equation of the form

$$\frac{1}{U^3 a} \frac{d}{dx} (U^3 a \bar{H} \theta) = \int_0^\delta \frac{\tau}{\frac{1}{2}\rho U^2} \frac{\partial}{\partial y} \left(\frac{u}{U}\right) dy \qquad (4\text{-}3)$$

where $\bar{H}$ is the ratio of energy thickness to momentum thickness. This equation was solved in closed form for $\theta$ by using some theoretical and experimental work of Rotta (Ref. 30) to obtain the following relations:

$$\frac{\tau_w}{\rho U^2} = f_1 \, (Re_\theta, H) \qquad (4\text{-}4)$$

$$\int_0^\delta \frac{\tau}{\rho U^2} \frac{\partial}{\partial y} \left(\frac{u}{U}\right) dy = f_2 (Re_\theta, H) \qquad (4\text{-}5)$$

$$\bar{H} = f_3 (H) \qquad (4\text{-}6)$$

where the functions, $f$, include empirically determined relations. The experimental work of Rotta was done with pressure gradients and momentum thickness Reynolds numbers up to approximately $10^5$. The shape factor is obtained from combining Equations (4-2) and (4-3) into a single equation and integrating using the relationships (4-4) through (4-6), so that an expression in closed form results. Reference 28 shows a comparison of the methods of von Doenhoff, Garner, and Truckenbrodt with data taken by von Doenhoff on an NACA 65(216)-222 airfoil at a Reynolds number based on chord length of $2.64 \times 10^6$ and a $10^\circ$ angle of attack. The three methods predict very similar trends for both $\theta$ and $H$ and agree reasonably well with the data, particularly for $\theta$, except very near separation, where the momentum thickness is underestimated by approximately 25 percent.

Granville used the form of Equation (4-1) obtained with $c = 0$ and $b = 1$. This relation, together with the continuity equation, the definitions of displacement and momentum thickness, and the assumption of the single parameter velocity profile using $H$, leads to a "moment of momentum" equation of the form, for $\delta \ll R$

$$\theta \frac{dH}{dx} = - \frac{H(H+1)(H^2-1)}{2} \frac{\theta}{U} \frac{dU}{dx} + H(H^2-1) \frac{\tau_w}{\rho U^2}$$

$$-(H+1)(H^2-1) \int_0^1 \frac{\tau}{\rho U^2} \, d\left(\frac{y}{\delta}\right) \tag{4-7}$$

The second equation used was Equation (4-2). These two equations solved simultaneously, together with several auxiliary relations, yield the variations of $\theta$ and $H$ with $x$. The auxiliary relations consist of:

(1) an expression for the flat-plate shear stress at the wall, derived from the Schoenherr resistance formula,

(2) a relationship between the wall shear stress in the presence of a pressure gradient and the flat-plate wall shear stress based on the law of the wall and a power-law velocity profile,

(3) an empirical relationship for the variation for a flat-plate, of shape factor, $H$, with momentum thickness Reynolds number, $Re_\theta$, developed by Tetervin and Lin from data having a Reynolds number range of $1.5 \times 10^3 < Re_\theta < 10^5$, and

(4) an expression for the integral of the shear stress through the boundary layer derived from Equations (4-7) and (4-2) on the basis of zero pressure gradient and checked on the basis of agreement with pressure-gradient data of Schubauer and Kelebanoff.

Of these four methods, it was felt that the method of Granville offered the most basic and rational approach to the prediction of the effects present in the turbulent boundary layer with pressure gradient. It could be said of all the methods that the empirical results used are based on a range of Reynolds number below that for application to a submarine. It is also a characteristic of each of the methods that the basic equations are valid only for the case of $\delta << R$, which assumption tends to be violated near the stern of the submarine. The method of Truckenbrodt is particularly simple in that no evaluation of the axial pressure (or velocity) gradient is necessary and expressions involving only the evaluation of an integral are available for computing directly both momentum thickness and shape parameter.

The most satisfactory manner of selecting a calculation method would be the application of each of the four methods to one or more cases for which experimental data exists at high Reynolds number and the subsequent evaluation of the results. However, this procedure was not considered justified because of the relatively minor role of this portion of the overall study. Since the region of greatest interest was the aft end of the hull where the application of all of the methods would be questionable, the simplest method, that of Truckenbrodt, was selected.

4.3 Boundary-Layer Calculations

The equations of Reference 28 which determine the boundary-layer characteristics are the following. The momentum thickness is given by:

$$\frac{\theta}{l} = \frac{\left[ C_t^* + \left(\frac{C_f}{2}\right)^{7/6} \int_{(\lambda/l)_t}^{(\lambda/l)} \left(\frac{U}{U_\infty}\right)^{10/3} \left(\frac{a}{l}\right)^{7/6} d\left(\frac{\lambda}{l}\right) \right]^{6/7}}{\left(\frac{U}{U_\infty}\right)^3 \left(\frac{a}{l}\right)} \tag{4-8}$$

where $$C_t^* = \left\{ \frac{C_{f_l}}{2} \left[ \int_0^{(\lambda/l)_t} \left(\frac{U}{U_\infty}\right)^5 \left(\frac{a}{l}\right)^2 d\left(\frac{\lambda}{l}\right) \right]^{1/2} \right\}^{7/6} \tag{4-9}$$

$$\left(\frac{\lambda}{l}\right)_t = \text{transition length} \tag{4-10}$$

$$c_f = 0.427\,(\log_{10} Re_l - 0.407)^{-2.74} \tag{4-11}$$

$$c_{f_l} = 1.328\,(Re_l)^{-1/2} \tag{4-12}$$

$$\lambda = \text{distance along body surface}$$

The shape factor is given by

$$L = \frac{\xi_t}{\xi} L_t + \ln_e \frac{U(\xi)}{U_t} + \frac{1}{\xi} \int_{\xi_t}^{\xi} \left[ b(\xi) - \ln_e \frac{U(\xi)}{U_t} \right] d\xi \tag{4-13}$$

where
$$\xi = \left[ c_t^* + \left(\frac{c_f}{2}\right)^{7/8} \int_{(\lambda/l)_t}^{\lambda/l} \left(\frac{U}{U_\infty}\right)^{10/3} \left(\frac{a}{l}\right)^{7/8} d\left(\frac{\lambda}{l}\right) \right]^4 \tag{4-14}$$

$$b = 0.07 \log_{10}\left(\frac{U\theta}{2}\right) - 0.23 \tag{4-15}$$

$$\xi_t = (c_t^*)^4 \tag{4-16}$$

$$H = f(L) \text{ from Figure 9 of Reference 28} \tag{4-17}$$

These equations were programmed for the Vidya IBM 1620 computer.

The input to the program consists of specifying the variation of the local velocity and body radius as a function of distance along the axis of the body, the location of transition, the value of H just downstream of transition, and the length Reynolds number. The program was written in such a way that the running length variable for the input was transformed from distance along the axis to distance along the surface. For high Reynolds numbers where transition occurs very close to the upstream end of the body, the results of the computation were found to be quite insensitive to variations in the assumed values of the transition point and H at transition. Generally, the value of H at transition was taken to be 1.4 and the location of transition, if it were not known experimentally, would be taken as $10^6/Re_l$.

The program was checked for the case of a flat plate at $Re_l = 10^8$. Transition was assumed to occur at $\lambda/l = 0.01$ with a resulting H of 1.4. The results for momentum thickness variation were compared with the von Kármán momentum equation, which for a flat plate reduced to:

$$\frac{d\theta}{dx} = \frac{C_f'}{2}$$

For the local skin-friction coefficient the Prandtl-Schlichting relation was used,

$$C_f' = (2 \log_{10} Re_x - 0.65)^{-2.3}$$

The results are shown in Figure 20. The Truckenbrodt method is seen to predict results very similar to the above method. The shape factor was compared with experimental data by assuming a power-law velocity profile and computing the exponent, $1/n$, from the computed shape factor. These results for H and n were then compared with correlations of the data of Dhawan, Schultz-Grunow and Kempf, which cover the range $10^6 < Re_l < 5\times10^8$, obtained from Reference 31. The comparison is shown in Figure 21. The agreement for H is reasonably good; for n, it is not as satisfactory. In general, the agreement tended to be poorer at high Reynolds numbers, which was to be expected, since the empirical correlations used in the Truckenbrodt method are based on data for $Re_\theta$ under $10^5$.

The program was then used to compute the boundary-layer characteristics on the USS Akron rigid airship for which data on boundary-layer velocity profiles exist at $Re_l = 1.2\times10^7$. The hull dimensions and profile were obtained from Reference 32. The boundary-layer velocity profiles were obtained from Reference 33 and reduced to obtain $\theta$ and H. The comparison between the Truckenbrodt method and data is shown in Figure 22. The agreement is reasonably good on $\theta$, but the theory tends to predict too low a shape factor over the length of the body. These results are typical of other comparisons made with high Reynolds number data taken on bodies of revolution (see Part II of this report), although the agreement on shape factor seemed to improve at higher Reynolds numbers. The effect of predicting too low a shape factor is to predict a slightly fuller velocity profile and a somewhat larger total thickness than should actually exist. These effects are quite small for the differences indicated in Figure 22, however, and are considered to have a negligible effect on the boundary-layer calculations.

As a result of the comparisons between the Truckenbrodt method and experimental data, it was felt that this method would be satisfactory for computing the boundary-layer effects of interest to this study.

## 5. APPLICATION OF METHODS TO A TYPICAL SUBMARINE CONFIGURATION

It was considered desirable to apply the methods discussed in Sections 3 and 4 to a specific, representative configuration in order to determine the size of the effects on the total forces and moments. Such a computation is discussed in this section.

### 5.1 Characteristics of the Assumed Configuration

The hull characteristics of modern, high-speed submarines are based in part on some early work done at the David Taylor Model Basin on systematizing bodies of revolution (Refs. 34 and 35). The resulting family of hull shapes was denoted Series 58. The offsets for the Series 58 hulls are determined by fitting a sixth-order polynomial to the curve of cross-section area versus length. The six coefficients are determined by specification of four non-dimensional parameters: the axial position of the maximum thickness section, m, the nose and tail radii of curvature, $r_0$ and $r_1$, respectively, and the prismatic coefficient, $C_p$. A number of Series 58 models have been built and tested, as indicated in Reference 36. For purposes of this study, one of these hulls was selected, Model 4165, and its characteristics were used with the exception of the tail radius, $r_1$, where a value of zero was felt to be more representative of existing submarines. The resulting values of the parameters are:

$$m = 0.4$$

$$r_0 = 0.50$$

$$r_1 = 0$$

$$C_p = 0.60$$

The non-dimensional hull offsets for this shape are given in the table of Figure 23. To complete the specification of the hull geometry, a fineness ratio of 7.33 was selected. For purposes of determining pitching moments, the center of gravity was assumed to be at the 44-percent axial station.

The characteristics of the stern planes that were assumed are taper ratio, aspect ratio, axial location on the hull, and span. The span was assumed to be such that when the quarter-chord line was located at the 90-percent length station on the hull, the tip of the stern plane had the same radius as the maximum hull radius. The quarter-chord line was taken to have no sweep. A taper ratio of 2/3 and an aspect ratio of 1.85, based on the span with hull and the projected area, were assumed. Since consideration of submarine motion was limited to the vertical plane, no assumptions were necessary concerning the rudder geometry. In addition, no bow plane effects were considered.

Some consideration was given to the effect of the bridge fairwater in initiating flow separation on the hull at angle of attack.

For this purpose, the leading edge of the bridge fairwater was assumed to be at the 30-percent length station on the hull and the axial length of the fairwater was assumed to be 0.1 that of the hull.

5.2 Boundary-Layer Analysis

A thick turbulent boundary layer exists on the aft portion of the submarine, as was indicated in Section 4. The degree to which the reduced velocity and dynamic head in the boundary-layer affect the forces on the stern planes was estimated using the velocity distribution computed according to the methods of Section 4.3.

The computer program utilizing the Truckenbrodt equations was applied to the hull geometry of Section 5.1. The velocity distribution used was that obtained from potential-flow theory with no allowance on the hull radius for boundary-layer displacement effects. The resulting distribution, indicated in terms of pressure coefficient, is shown in Figure 24. The assumption of no boundary-layer displacement effects should be quite good up to approximately the 90-percent length station. Beyond this station this assumption becomes increasingly poor. However, the boundary-layer theory also becomes inadequate because of its assumption of $\delta \ll R$, so the results of the computations are not reliable much beyond the 90-percent station of the hull. Transition was assumed to occur at the 4-percent axial-length station. A length Reynolds number of $6.5 \times 10^8$ was used. This would correspond, for instance, to a 200-foot-long submarine traveling at 25 knots.

The results of the computation are shown in Figures 25 and 26, which indicate the momentum thickness and shape factor as a function of distance along the hull, respectively. The displacement thickness was obtained from the shape factor and momentum thickness directly, and the velocity profiles in the boundary layer were obtained in the form $u/U$ versus $y/\theta$ from the shape factor and Figure 10 of Reference 26.

The boundary-layer effects on the stern plane forces were estimated in the following way. At any given distance from the hull surface, the lift or normal force induced on an element of surface, of the stern plane due to a small angle of attack is proportional to the dynamic head at that distance. Thus, if the dynamic head is reduced because that point on the plane is within the boundary layer, the factor by which it is reduced is $(u/U)^2$, or the square of the ratio of the local to the boundary-layer-edge velocity. For purposes of computing this effect, the stern plane was divided into strips parallel to the hull of width normal to the hull surface $\Delta y$ and length along the hull surface equal to the distance between the leading and trailing edges of the stern plane. The latter length is somewhat different from the local chord of the stern plane because of the varying hull radius along the chord length. It was assumed that the velocity ratio on the strip was uniform along the length of the strip and was given by the value of the ratio at the 50-percent-chord point. The following finite-difference expression was then evaluated:

$$R = \frac{1}{S} \sum_{0}^{S} \left(\frac{u}{U}\right)^2 \Delta S \tag{5-1}$$

where $R$ is the ratio of lift force with boundary layer to lift force without boundary layer, $S$ is the projected area of the plane, and $\Delta S$ is the area of the strip $\Delta y$ wide whose center is a distance $y$ from the hull surface.

With the quarter-chord location at the 90-percent station, the 50-percent-chord location is at approximately the 92-percent station, where Figures 25 and 26 indicate $\theta/l = 2.4\times10^{-3}$ and $H = 1.33$. Figure 10 of Reference 26 indicates, for $H = 1.33$, a value of $y/\theta = 9$ at the point where $u/U = 1$. As a result, approximately 45 percent of the semispan of the stern plane is immersed in the boundary layer. The summation of Equation (5.1) was performed using the velocity profile for $H = 1.33$ and the geometry of the stern plane. A value of $R = 0.86$ was obtained. Essentially 14 percent of the normal force is lost because of the reduced velocity in the boundary layer.

A number of simplifying assumptions were made in this calculation. The end result therefore needs to be evaluated in terms of these assumptions. First, the boundary-layer velocity profile used was obtained with a theory whose results tend to become questionable near the aft end of the hull. Because the boundary-layer thickness becomes appreciable compared to the hull radius ($\delta \approx R$), the theory should predict too low a boundary-layer thickness, and thus, too large a value of R. Secondly, a one-dimensional treatment of the velocity variation over the stern plane was used wherein the velocity at a given distance from the hull was assumed constant over the chord length. This assumption would tend to yield a somewhat high value of R, also, although the effect probably would not be large. Thirdly, the theory is unable to predict the influence of the propeller on the flow near the stern. The propeller tends to accelerate the fluid near the stern which causes a fuller velocity profile to exist than is predicted analytically. The velocities may even exceed the boundary-layer-edge velocity locally, as was observed experimentally in the model tests reported in Reference 24. This effect would tend to raise the value of R.

The last of these three effects is felt to be the dominant one in determining the flow velocities over the stern. Consequently, the value of 0.86 is considered to be somewhat low in a practical sense for the assumed configuration at zero or small angles of attack. Submarines having a larger length-to-diameter ratio, as do some of the newer ones, would have a larger boundary-layer thickness relative to the maximum hull diameter and would tend to have greater boundary-layer effects on the control surfaces. However, the propeller will still exert a large influence, and it is felt that the blanketing effect would not be a significant factor.

### 5.3 Forces and Moments at Angle of Attack

The theory for predicting normal force and pitching moment at angle of attack discussed in Section 3 was applied to the configuration described in Section 5.1. As was indicated in Section 3, the forces and moments can be considered the sum of two contributions. The first, a contribution linear with $\alpha$, is given by potential flow theory assuming no separation (with the effect of viscosity manifest primarily in the wake shed at the stern). The second, a nonlinear contribution, is the result of separation and vortex formation at high angles of attack. The results are presented for the hull alone, which would correspond to forces and moments on a towed bare hull, and the hull with stern planes, which would correspond to a powered full configuration (with the exception of a pitching-moment contribution due to the bridge fairwater).

The potential flow, non-separated, normal-force distribution on the hull was obtained using Equation (3-15). The effect of viscosity was approximated by assuming the hull to have an effective base area given by the wake radius as discussed in Section 3.4 This radius was arbitrarily assumed to be given by the sum of the hull radius and the displacement thickness of the boundary layer, as determined by the zero angle-of-attack computations of Section 5.2, at the 95-percent axial station. The resulting wake radius was 28 percent of the maximum hull radius. The normal force is then

$$N = 2\alpha q_\infty \, (\pi R_W{}^2) \tag{5-2}$$

Equation (3-15) can be multiplied on both sides by $(x - x_{CG})$ and integrated to give pitching moment about the center of gravity.

The effect of the stern planes was computed using Reference 20. The lift (or normal force) on the stern planes in the presence of the hull and the lift carryover onto the hull were determined in the form

$$C_L = K \left(C_{L_\alpha}\right)_T \alpha \tag{5-3}$$

where the two $K$ factors were obtained, using slender-body theory, from Figure 2 and Equation (21) of Reference 20, respectively. The quantity $\left(C_{L_\alpha}\right)_T$ is the lift-curve slope of the stern planes alone. A value of 2.05 was selected for $\left(C_{L_\alpha}\right)_T$ based on the data of Reference 19 for an aspect ratio for the tail alone of 1.37. This value compares favorably with a value of 2.15 predicted by slender-body theory. The $\left(C_{L_\alpha}\right)_T$ is based on the planform area of the stern planes. For determining the pitching-moment contribution of the stern planes, their center of pressure was taken to be at the quarter-chord point. No stern plane blanketing effects due to boundary layer were included.

The effects of separation and vortex shedding were computed for angles of attack of 10°, 15°, and 20°. For the hull viscous normal force and pitching moment, the computer program described in Section 3 was employed. The two inputs of greatest significance are the axial location where separation begins, $x_s$, and the angular location of the separation line in a normal plane, $\theta_o$. As has been indicated, there is no theoretical method of determining these values, and the experimental data available is deficient both in high Reynolds number effects and the effect of axially varying radius. Consequently, the data of Figures 9 and 10 were used as a guide.

For the case of the hull alone, values of $x_s/d$ were selected in the center of the range of data of Figure 9. The following values obtain:

| $\alpha$ | $x_s/d$ |
|---|---|
| $10^\circ$ | 6 |
| $15^\circ$ | 4 |
| $20^\circ$ | 3 |

Figure 10(b) indicates the incompressible data for $\theta_o$ falling in the range of $40^o$ to $50^o$. This one set of data also indicates a smaller $\theta_o$ at the higher Reynolds number. On this basis, a constant value of $40^o$ was assumed over the length which was separated on the hull. The hull viscous normal force and pitching moment, as determined from the vortex shedding program, were then added to the unseparated forces and moments. The hull-alone results are presented in Figures 27 and 28.

For the case of the hull with stern planes, the effect of the bridge fairwater located at $x/d = 2.2$ was considered in determining the values of $x_s$ to be used. The following values were assumed:

| $\alpha$ | $x_s/d_{max}$ |
|---|---|
| $10^o$ | 4.5 |
| $15^o$ | 3 |
| $20^o$ | 2.2 |

Again, a value of $\theta_o = 40^o$ constant with length was selected for the hull with stern planes. The computed viscous separation effects were added to the non-separated forces and moments and are shown in Figures 29 and 30. The notation and sign convention of Figures 27 through 30 are those of Reference 37.

The results in Figure 27 show a normal-force slope at $\alpha = 0$ for the hull alone of $4\times10^{-5}$ per degree, using the "effective" wake method. For comparison purposes, the comparable value was obtained for several bodies with pointed tails on which experimental data exist. Reference 25 shows a value of $4\times10^{-4}$ for an early, proposed high-speed submarine hull. Reference 38 indicates values of $2.5\times10^{-4}$ and $4\times10^{-4}$ for fineness rations of 10 and 5.9, respectively, for bodies similar to a submarine hull. Reference 39 shows $2\times10^{-4}$ for a Goodyear-Zeppelin model with $L/D = 7.2$. The Reynolds numbers for these tests were in the range of $10^6$ - $4\times10^7$, based on model length.

It is apparent that the theory predicts too low a $Z'_{\alpha}$ by a factor of at least 5. As was indicated in Section 3.4, this might have been expected since the method does not consider the fundamental nature of the flow at the stern.

Figure 27 shows that the viscous normal force due to separation becomes apparent at approximately $8^{\circ}$ angle of attack. This force is upward and adds to the nonseparated normal force. The separation induced forces increase rapidly with angle of attack.

The pitching-moment slope at zero $\alpha$ is also affected by the base flow, although to a much smaller degree. The nonseparated pitching-moment slope was computed both for the actual hull and the hull with boundary layer (using the axisymmetric boundary-layer calculations). The effect of the boundary layer was to reduce the slope approximately 3 percent. The moment with boundary-layer effects is shown in Figure 28. A slope of $3\times10^{-4}$ per degree is indicated. The various references for normal force of the previous paragraph indicate typical values for pitching-moment slope of $4.3\times10^{-4}$, $2.6\times10^{-4}$, $7\times10^{-4}$, which are in the same range as the computed value. The effect of separation on pitching moment is to cause an upward normal force aft of the center of gravity which decreases the overall pitching moment. Again the separation effects become apparent at about $8^{\circ}$ angle of attack and increase with angle of attack.

For the hull with stern planes, the nonseparated normal-force contribution of the stern planes is an order of magnitude larger than the hull contribution. In Figure 29, it was assumed that the configuration was self-powered and that the effect of the propeller on the flow over the stern would decrease the hull contribution to a negligible quantity. Consequently, the nonseparated normal-force coefficient indicated in Figure 29 is based only on the contribution of the stern planes. The additional forces due to separation are those on the hull and on the stern planes, due to vortex interference. As indicated previously, the hull force due to separation is an upward force adding to the stern plane force. The separation vortices passing over the stern planes induce a downwash on the planes which tends to reduce their lift. Of these two viscous effects, the hull force predominates, as shown in the following table of normal coefficients for $\alpha = 20^{\circ}$:

| Item | Z' |
|---|---|
| Stern planes in presence of hull - no separation | -0.00705 |
| Lift carryover onto hull - no separation | -0.00251 |
| Hull - separation induced | -0.00775 |
| Stern planes - vortex interference | +0.00197 |

The pitching moment for the hull with stern planes is shown in Figure 30. With no separation, the planes contribute a stabilizing pitching moment which partially compensates for the destabilizing moment of the hull. Separation on the hull induces a stabilizing moment, since the viscous normal force acts aft of the center of gravity. The vortex interference acts to reduce the lift force on the stern planes and thus provides a destabilizing moment. The sum of these effects is shown in Figure 30. The relative magnitudes are shown in the following table, for $\alpha = 20^{\circ}$:

| Item | M' |
|---|---|
| Hull - no separation | +0.00608 |
| Stern planes total - no separation | -0.00440 |
| Hull - separation-induced | -0.00173 |
| Stern planes - vortex interference | +0.00091 |

It should be noted in connection with Figures 27 through 30 that the results for the separation-vortex-induced effects are based on somewhat arbitrary assumptions concerning $\theta_o$ and $x_s$. Values were selected based on the best available data. These data, however, do not reflect a varying body radius or high Reynolds numbers characteristic of the submarine. Nor do they reflect such possible effects, for the real case, as the bridge fairwater and deck initiating separation. In general, the vortex interference effects would tend to decrease for a given $\alpha$ with increasing $\theta_o$ and increasing $x_s$.

## 6. CONCLUSIONS

A theoretical analysis of the prediction of the force distribution induced on an inclined body of revolution by flow separation has been made. The analysis follows that of Reference 14 and, with the assumption of slender-body theory, transforms the steady, three-dimensional separation-vortex flow into an unsteady, two-dimensional vortex motion in the normal plane. The theoretically predicted viscous normal-force distribution due to the vortex motion is compared with experimental data for an inclined ogive cylinder. The theory is applied to a typical submarine configuration to determine the magnitude of separation effects over a range of angles of attack, and comparisons with experimental results are made (Part II of this report).

### 6.1 Theoretical Methods

The following conclusions can be made concerning the development and use of the theoretical methods:

(1) An unsteady, two-dimensional vortex model with the vorticity in the flow field lumped into a single pair of vortices was assumed to represent the steady, three-dimensional vortex flow over the body. The simplification in the flow model yields two difficulties with respect to interpretation of the results. First, a mathematical singularity exists at the separation line on the body (starting point) which causes an uncertainty to exist in the axial location of the predicted viscous normal-force distribution. Secondly, the asymptotic behavior of the vortex pair in the unsteady analysis is governed by the Föppl condition, which should have no significance in the steady, three-dimensional case.

(2) The method requires as an input the location on the body of the separation line. There is at present no theoretical method of obtaining this information on an inclined body of revolution. Few experimental data exist on measurements of the location of separation and essentially no data exist on the area of the body where separation originates. The data that exist do not indicate the effect of a varying body radius with length. These data are also an order of magnitude low in Reynolds number compared to a typical submarine Reynolds number.

(3) A comparison of the method with the data of Reference 5 for an ogive-cylinder indicated reasonably good agreement on vortex strength and vertical position above the body but only a qualitative agreement on viscous cross-flow drag coefficient. The lateral vortex motion was not predicted by the theory. More data for incompressible flow with careful measurements on the location of separation are necessary to check the theory adequately.

(4) The method of Truckenbrodt for the calculation of incompressible, turbulent, axisymmetric boundary layers was found to predict momentum thickness well but tends to predict too low a value of shape factor, except for very high Reynolds numbers. The method appeared to be adequate up to the 90-percent-length station.

### 6.2 Application of the Methods to a Submarine

The application of the methods of analysis of flow separation and boundary-layer effects to a submarine configuration have indicated the following conclusions:

(1) For a body with a pointed tail, the use of slender-body theory together with an axisymmetric, effective wake radius for determining normal force at angle of attack is inadequate. Such a prediction must consider base separation, the nonsymmetrical effects, and the nature of viscous flow where the body radius is small compared to the viscous layer thickness. The pitching moment, however, is much less sensitive to the base flow and should be predicted reasonably well by this method.

(2) The blanketing of the stern control surfaces by the turbulent boundary layer on the hull for the self-powered case is a small effect at zero and small angles of attack.

(3) Experimental data on both hull model and full-scale submarines indicate that nonlinear normal-force and pitching-moment effects become apparent in the range of $6^\circ$ to $10^\circ$ angle of attack. The separation theory predicts the onset and direction of these effects. The quantitative agreement on the nonlinear portion based on arbitrary assumptions regarding the location of separation is fair; it could probably be made quite good by small, reasonable changes in the assumed values of $\theta_o$ and $x_s$.

(4) For the assumed typical submarine configuration at $20^\circ$ angle of attack, the separation-induced normal force on the hull was found to be approximately the same in direction and magnitude as the force determined in the absence of separation. The vortex interference force on the stern planes acted to reduce the nonseparated lift by approximately 20 percent. The pitching-moment contribution of the hull separation force was found to be a stabilizing moment approximately one-fifth the moment of the unseparated hull. The moment due to the vortex interference force on the stern planes was found to be a destabilizing effect reducing the stabilizing plane moment by approximately 20 percent.

(5) Some experimental evidence indicating the onset of unsteady vortex motion in the separated region over the body was found at angles of attack in excess of $20^\circ$ in model tests on a submarine hull shape and typical missile shapes.

## 7. RECOMMENDATIONS

On the basis of the investigations described in this report and the conclusions indicated in Section 6, the following recommendations are made for further work in the area of prediction of submarine stability characteristics:

(1) The limitations on the accuracy and completeness of the two-dimensional vortex separation model described in Section 3 should be studied in detail to determine if improvements can and should be made. In particular, the starting problem, the lumped vorticity assumption, the force-balance assumption, the asymptotic behavior, and three-dimensional effects should be considered.

(2) Additional work is needed in determining theoretically the characteristics of the turbulent, incompressible boundary layer on an inclined body of revolution. This work would hopefully include an analysis of the conditions under which such a boundary layer separates.

(3) An urgent need exists for experimental data on separation characteristics and vortex shedding on inclined bodies of revolution indicating the effects of varying body radius with length and high Reynolds number. These data should include the location of the separation line (as determined not only by pressure measurements, but flow visualization techniques as well), pressure measurements on the body at a number of axial stations, pressure measurements in the flow field to determine vortex location and strength, and flow-visualization measurements of the vortex motion.

(4) The theoretical methods should be extended to include interference effects of the bridge fairwater, the fairwater planes, and bow planes for motion of the submarine in the vertical plane.

(5) The interference methods should be extended to motion of the complete submarine in the horizontal plane, including the effects of yaw and roll.

(6) Methods should be developed for predicting the force distribution on a submarine configuration for small angles of attack where the flow is attached (except at the stern), for motion in both the vertical and horizontal planes. The work in this area reported herein was done only for comparative purposes and does not necessarily represent the best approach to this problem. Item 7 is basically a part of the same problem.

(7) Work should be done in the area of base separation for bodies with pointed tails in order to predict the surface pressures and the velocity distribution in the region of the tail. This could be the first step in the more complex problem of predicting the flow characteristics near the stern with propeller.

(8) Additional theoretical and experimental work are needed on the effects of Reynolds number, body shape, and angle of attack on the onset of instability in the vortex flow on the leeward side of inclined bodies of revolution.

## REFERENCES


1. Jorgensen, L. H. and Perkins, E. W.: Investigation of Some Wake Vortex Characteristics of an Inclined Ogive-Cylinder at Mach Number = 2. NACA Rept. 1371, 1958.

2. Gowen, F. E. and Perkins, E. W.: A Study of the Effects of Body Shape on the Vortex Wakes of Inclined Bodies at a Mach Number of 2. NACA RM A53117, 1953.

3. Perkins, E. W. and Jorgensen, L. H.: Comparison of Experimental and Theoretical Normal Force Distribution on an Ogive-Cylinder Body at M = 1.98. NACA TN 3716, 1956.

4. Allen, H. J. and Perkins, E. W.: A Study of the Effects of Viscosity on Flow over Slender Inclined Bodies of Revolution. NACA Rept. 1048, 1951.

5. Tinling, B. E. and Allen, C. Q.: An Investigation of the Normal Force and Vortex Wake Characteristics of an Ogive-Cylinder Body at Subsonic Speeds. NASA TN D-1297, 1962.

6. Mello, J. F.: Investigation of Normal Force Distribution and Wake Vortex Characteristics of Bodies of Revolution at Supersonic Speeds. Jour. of the Aero. Sci., vol. 26, no. 3, Mar. 1959.

7. Maltby, R. L. and Peckam, D. H.: Low Speed Flow Studies on the Vortex Patterns Above Inclined Slender Bodies Using a New Smoke Technique. RAE TN Aero 2482, 1956. (Astia AD 125 852).

8. Raney, D. J.: Measurements of the Cross Flow Around an Inclined Body at a Mach Number of 1.91. RAE TN Aero 2357, 1955.

9. Sacks, A. H.: Aerodynamic Forces, Moments, and Stability Derivatives for Slender Bodies of General Cross Section. NACA TN 3283, 1954.

10. Sacks, A. H.: Vortex Interference on Slender Airplanes. NACA TN 3525, 1955.

11. Maskell, E. C.: Flow Separation in Three Dimensions. RAE Rept. No. Aero 2565, 1955.

12. Milne-Thomson, L. M.: Theoretical Hydrodynamics. Fourth Edition, The MacMillan Co., 1960.

13. Nielsen, J. N.: Missile Aerodynamics. McGraw-Hill Book Co., Inc., 1960.

14. Bryson, A. E.: Symmetric Vortex Separation on Circular Cylinders and Cones. Jour. of Appl. Mechs., Dec. 1959.

15. Lamb, H.: Hydrodynamics. Sixth Edition. Dover Publications, 1932.

16. Prandtl, L. and Tietjens, O. B.: Applied Hydro- and Aerodynamics. McGraw-Hill Book Co., 1934.

17. Jorgensen, L. H.: Elliptic Cones Alone and With Wings at Supersonic Speeds. NACA Rept. 1376, 1958.

18. Moore, F. K.: Laminar Boundary Layer on Cone in Supersonic Flow at Large Angle of Attack. NACA Rept. 1132, 1953.

19. Whicker, L. F. and Fehlner, L. F.: Free Stream Characteristics of a Family of Low Aspect Ratio, All Movable Control Surfaces for Application to Ship Design. DTMB Rept. 933, 1958.

20. Pitts, W. C., Nielsen, J. N., and Kaattari, G. E.: Lift and Center of Pressure of Wing-Body-Tail Combinations at Subsonic, Transonic, and Supersonic Speeds. NACA Rept. 1307, 1959.

21. Goldstein, S., ed.: Modern Developments in Fluid Mechanics. Vol. II, Oxford University Press, 1938.

22. Cooper, M., Gapcynski, J. P., and Hasel, L. E.: A Pressure Distribution Investigation of a Fineness-Ratio-12.2 Parabolic Body of Revolution (NACA RM-10) at $M = 1.59$ and Angles of Attack Up to $36^{\circ}$. NACA RM L52G14, Oct. 1952.

23. Beveridge, J. L.: Effect of Axial Position of Propeller on the Propulsion Characteristics of a Submerged Body of Revolution. DTMB Rept. 1456, Mar. 1963.

24. Beveridge, J. L.: An Experimental Investigation of Model and Ship Submerged Wake and Afterbody Normal Pressure Distribution for the USS Albacore AGSS 569. DTMB Rept. C 896, Aug. 1958.

25. Cocke, B. W., Lipson, S., and Scallion, I.: Data from Tests of a 1/5 Scale Model of a Proposed High Speed Submarine in the Langley Full Scale Tunnel. NACA RM SL50E9a, 1950. (Declassified)

26. von Doenhoff, A. E. and Tetervin, N.: Determination of General Relations for the Behavior of Turbulent Boundary Layers. NACA Rept. 772, 1943.

27. Garner, H. E.: The Development of Turbulent Boundary Layers. Aeronautical Research Council R&M 2133, June 1944.

28. Truckenbrodt, E.: A Method of Quadrature for Calculation of the Laminar and Turbulent Boundary Layer in Cases of Plane and Rotationally Symmetrical Flow. NACA TM 1379, 1955. (Translation)

29. Granville, P. S.: A Method for the Calculation of the Turbulent Boundary Layer in a Pressure Gradient. DTMB Rept. 752, 1951.

30. Rotta, J.: Ing-Arch. Vol. 19, p. 31, 1951 and vol. 20, p. 195, 1952.

31. Sivells, J. C. and Payne, R. G.: A Method of Calculating Turbulent-Boundary-Layer Growth at Hypersonic Mach Numbers. AEDC TR 59-3, Mar. 1959, ASTIA AD 208774.

32. Freeman, H. B.: Pressure-Distribution Measurements on a Hull and Fins of 1/40-Scale Model of the US Airship "Akron." NACA Rept. 443, 1932.

33. Freeman, H. B.: Measurements of Flow in the Boundary Layer of a 1/40-Scale Model of the US Airship "Akron." NACA Rept. 430, 1932.

34. Landweber, L. and Gertler, M.: Mathematical Formulation of Bodies of Revolution. DTMB Rept. 719, Sept. 1950.

35. Gertler, M.: A Systematic Series of Streamline Bodies of Revolution for Application to the Hydrodynamic Design of High Speed Submarines. DTMB Rept. C-840, 1957.

36. Gertler, M.: Resistance Experiments on a Systematic Series of Streamlined Bodies of Revolution - for Application to the Design of High-Speed Submarines. DTMB Rept. C-297, Apr. 1950, (Declassified).

37. Imlay, F. H.: A Nomenclature for Stability and Control. DTMB Rept. 1319, May 1959.

38. Lange, G.: Force and Pressure Distribution Measurements on Eight Fuselages. NACA TM 1194, 1948. (Translation from ZWB Forschungsbericht Nr. 1516, Oct. 1941.)

39. Abbott, I. H.: Airship Model Tests in the Variable Density Wind Tunnel. NACA Rept. 394, 1931.

40. Hsu, E. Y.: The Measurement of the Boundary Layer and Local Turbulent Skin Friction on a Particular Body of Revolution. DTMB Rept. C-892, 1958. (Confidential)

41. Eskigian, N. M. and Sedlak, C.: Model Studies of a Systematic Series of Streamline Bodies of Revolution. Stevens Institute of Technology Rept. No. 547, 1955. (Confidential)

42. Eskigian, N. M.: Model Studies of a Systematic Series of Streamline Bodies of Revolution of Varying Fineness Ratio at High Angles of Attack and Angular Velocities. Stevens Institute of Technology Rept. No. 585, Nov. 1955. (Confidential)

43. Stracke, W. L.: Full Scale Evaluation of the Static Stability and Control Derivatives of the USS Albacore (AGSS 569) with Second Stern Configuration. DTMB Rept. C-829, 1957.

44. Olson, C. R.: Model - Full Scale Correlation of the Handling Qualities of the Albacore II in the Horizontal Plane and the Effect of Bridge Fairwater Removal. DTMB Rept. C-935, 1958. (Confidential)

## APPENDIX A

## THE COMPLEX POTENTIAL

The complex potential is given by

$$W = \phi + i\psi \tag{A-1}$$

where the velocities are defined in terms of the potential by

$$v = + \frac{\partial\phi}{\partial y} = + \frac{\partial\psi}{\partial z} \tag{A-2}$$

$$w = + \frac{\partial\phi}{\partial z} = - \frac{\partial\psi}{\partial y} \tag{A-3}$$

and

$$\frac{dW}{d\zeta} = v - iw = (v_r - iv_\theta)e^{-i\theta} \tag{A-4}$$

Thus, the complex potential for uniform flow in the positive $z$ direction is

$$W = -i(U_\infty \sin \alpha)\zeta \tag{A-5}$$

From Equation (A.4)

$$\frac{dW}{d\zeta} = v - iw = - i(U_\infty \sin \alpha)$$

and separating into real and imaginary parts

$$v = 0$$

$$w = + U_\infty \sin \alpha$$

The source term in Equation (3-4), which is the last term, is obtained as follows. The general expression for the complex potential of a source is

$$W = m \ln \zeta \tag{A-6}$$

where $m$ is the source strength. Using Equation (A-4)

$$\frac{dW}{d\zeta} = (v_r - iv_\theta)e^{-i\theta} = \frac{m}{\zeta} = \frac{m}{re^{i\theta}} = \frac{m}{r}e^{-i\theta}$$

Therefore, comparing real and imaginary parts,

$$v_r = \frac{m}{r}, \quad v_\theta = 0 \tag{A-7}$$

If the radius of the body is growing at a rate $\dot{a}$ and has a radius at a given time of $a$, then on the surface of the body, $r = a$ and $v_r = \dot{a}$ and from Equation (A-7)

$$\dot{a} = \frac{m}{a}$$

or

$$m = a\dot{a}$$

Therefore, the expression for the complex potential, Equation (A-6), can be written for the source representing the time rate of change of body radius as

$$W = a\dot{a} \ln \zeta$$

which is the form appearing in Equation (3-4) of the text.

## APPENDIX B

## THE FORCE CONDITIONS ON THE VORTEX AND SHEET

In the flow configuration illustrated in Figure 7, a force exists on the sheet because of the rate of change of strength of the concentrated vortex. This situation occurs as follows. Consider a vortex of strength $\Gamma(t)$ at the origin of a coordinate system as shown in the sketch

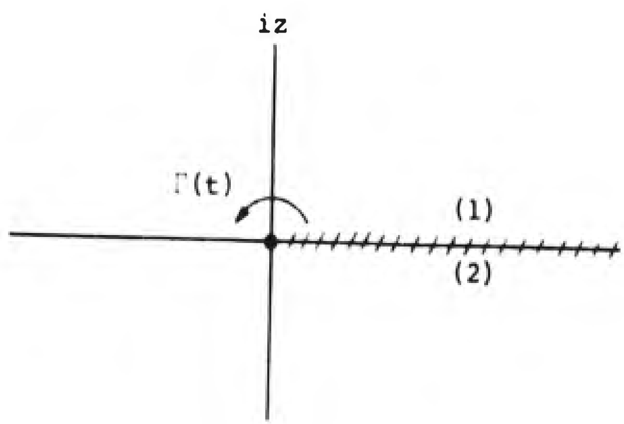


The complex potential for this vortex is

$$W = -i\,\frac{\Gamma(t)}{2\pi}\,\ln = -i\,\frac{\Gamma(t)}{2\pi}\,\ln\,(re^{i\theta})$$

$$= -i\,\frac{\Gamma(t)}{2\pi}\,\ln r + \frac{\Gamma}{2\pi}\,\theta \qquad \text{(B-1)}$$

Therefore, the velocity potential is given by the real part of the complex potential, or

$$\phi = \frac{\Gamma(t)}{2\pi}\,\theta$$

In order for the velocity potential to be single-valued, a mathematical branch cut must exist which in this case is indicated along the positive y-axis from $y = 0$ to $y = +\infty$. Thus, the value of $\theta$ is limited to the range of zero to $2\pi$. There is a discontinuity in $\phi$ across the branch cut of value $\Gamma(t)$.

The unsteady equation of motion for an incompressible fluid in the absence of body forces may be written

$$\frac{p}{\rho} + \frac{1}{2}(v^2 + w^2) + \frac{\partial\phi}{\partial t} = A(t) \tag{B-3}$$

where $A(t)$ is an arbitrary function of time. If this equation is applied between points (1) and (2), as indicated on the sketch, where the radii are the same and arbitrary but the angle $\theta$ has the value 0 and $2\pi$, respectively, there results

$$\frac{p_1}{\rho} + \frac{1}{2}(v^2 + v^2)_1 + \left(\frac{\partial\phi}{\partial t}\right)_1 = \frac{p_2}{\rho} + \frac{1}{2}(v^2 + w^2)_2 + \left(\frac{\partial\phi}{\partial t}\right)_2 \tag{B-4}$$

since $A(t)$ is the same for both points. The velocity components are given, in general, by

$$v_r = \frac{\partial\phi}{\partial r}, \quad v_\theta = \frac{1}{r}\frac{\partial\phi}{\partial\theta}$$

and at the points of interest, using Equation (B-2),

$$v_{r_1} = v_{r_2} = 0$$

and

$$v_{\theta_1} = \frac{\Gamma(t)}{2\pi r_1} = v_{\theta_2}$$

Therefore, in Equation (B-4), the velocity terms at (1) and (2) are identical and drop out. There results

$$p_1 - p_2 = \rho \left[ \left(\frac{\partial\phi}{\partial t}\right)_2 - \left(\frac{\partial\phi}{\partial t}\right)_1 \right] \tag{B-5}$$

Now, from Equation (B-2),

$$\frac{\partial\phi}{\partial t} = \frac{\dot{\Gamma}(t)}{2\pi}\,\theta$$

and Equation (B-5) becomes

$$p_1 - p_2 = \rho \left[ \frac{\dot{\Gamma}(t)}{2\pi}\,2\pi - \frac{\dot{\Gamma}}{2\pi}\,0 \right] = \rho\dot{\Gamma}(t)$$

In the case of a vortex pair, as exists in Figure 7, the branch cut may be a line joining the external vortex to the image vortex. This cut is assumed to pass through the separation point $\zeta_0$ on the body so that the portion of this cut external to the body coincides with the sheet. The force on the sheet is then determined by the pressure difference across the sheet and its end points, or

$$F_s = i\rho\dot{\Gamma}(\zeta_1 - \zeta_0) \tag{B-6}$$

since the force is at right angles to the line $\zeta_1 - \zeta_0$.

Since a force exists on the sheet and a zero net force is wanted on the flow external to the body, a force must exist on the concentrated vortex. Such a force requires a motion of the vortex in relation to the local velocity at its center, as shown in the sketch.

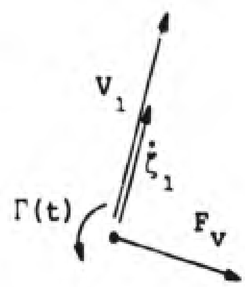


The local velocity at the vortex center is given by Equation (3-6) of the text. The vortex is moving with a velocity $\dot{\zeta}_1$. The vortex behaves as if it were stationary in a flow having a velocity $V_1 - \dot{\zeta}_1$. A force is induced on the vortex much as lift is induced on a wing with circulation in a flow. According to the Kutta-Joukowski theorem (Ref. 12, Section 7.45), the force induced on the vortex is given by the product of $\rho$, $\Gamma$, and the relative velocity and has a direction obtained by rotating the relative velocity vector 90° in a sense opposite to that of the circulation. Therefore, the force on the vortex is given by

$$F_V = i\rho\Gamma(V_1 - \dot{\zeta}_1) \tag{B-7}$$

which is Equation (3-8) of the text.

## APPENDIX C

## REDUCTION OF FORM OF THE EQUATIONS OF VORTEX MOTION

The relations describing the motion of the shed symmetric vortex pair and the induced forces on the body are given in Equations (3-6), (3-10), (3-11), and (3-14) of the text.

Equation (3-10) is the basic differential equation of motion of the vortices. It is:

$$\zeta_1 + (\zeta_1 - \zeta_o)\frac{\dot{\Gamma}}{\Gamma} = V_1 \tag{3-10}$$

The complex coordinate $\zeta_1$ is equal to $y_1 + iz_1$. The circulation $\Gamma$ is a real, positive number, as will be seen later. The velocity $V_1$ may be divided into real and imaginary parts $V_{RE_1}$ and $V_{IM_1}$. Then Equation (3-10) becomes

$$\dot{y}_1 + (y_1 - y_o)\frac{\dot{\Gamma}}{\Gamma} = V_{RE_1} \tag{C-1}$$

$$z_1 + (z_1 - z_o)\frac{\dot{\Gamma}}{\Gamma} = V_{IM_1} \tag{C-2}$$

The expression for $\bar{V}_1$ is given in Equation (3-6) of the text, where $\bar{V}_1 = V_{RE_1} - iV_{IM_1}$, as

$$\bar{V}_1 = -iU_\infty \sin\alpha\left(1 - \frac{a^2}{\zeta_1^{\,2}}\right) - i\frac{\Gamma}{2\pi}\left(\frac{1}{\zeta_1 + \frac{a^2}{\zeta_1}} - \frac{1}{\zeta_1 - \frac{a^2}{\bar{\zeta}_1}} - \frac{1}{\zeta_1 + \bar{\zeta}_1}\right)$$

$$+ \frac{a\dot{a}}{\zeta_1} \tag{3-6}$$

This expression may be separated into real and imaginary parts by letting $\zeta_1 = y_1 + iz_1$ and $\bar{\zeta}_1 = y_1 - iz_1$. As a sample, consider the first term in the brackets following $\Gamma$.

$$-i\,\frac{\Gamma}{2\pi}\,\frac{1}{\zeta_1 + \frac{a^2}{\zeta_1}} = -i\,\frac{\Gamma}{2\pi}\,\frac{\zeta_1}{\zeta_1^{\,2} + a^2} = -i\,\frac{\Gamma}{2\pi}\,\frac{(y_1 + iz_1)}{(y_1 + iz_1)^2 + a^2}$$

$$= -i\,\frac{\Gamma}{2\pi}\,\frac{(y_1 + iz_1)}{y_1^{\,2} + 2iy_1z_1 - z_1^{\,2} + a^2} = -i\,\frac{\Gamma}{2\pi}\,\frac{(y_1 + iz_1)}{\left(y_1^{\,2} - z_1^{\,2} + a^2\right) + 2iy_1z_1}$$

$$= -i\,\frac{\Gamma}{2\pi}\,\frac{(y_1 + iz_1)}{\left[\left(y_1^{\,2} - z_1^{\,2} + a^2\right) + 2iy_1z_1\right]}\;\frac{\left[\left(y_1^{\,2} - z_1^{\,2} + a^2\right) - 2iy_1z_1\right]}{\left[\left(y_1^{\,2} - z_1^{\,2} + a^2\right) - 2iy_1z_1\right]}$$

$$= -i\,\frac{\Gamma}{2\pi}\,\frac{(y_1 + iz_1)\left[\left(y_1^{\,2} - z_1^{\,2} + a^2\right) - 2iy_1z_1\right]}{\left(y_1^{\,2} - z_1^{\,2} + a^2\right)^2 + 4y_1^{\,2}z_1^{\,2}}$$

$$= -i\,\frac{\Gamma}{2\pi}\,\frac{\left(y_1^{\,3} - y_1z_1^{\,2} + y_1a^2 + 2y_1z_1^{\,2}\right) + i\left(y_1^{\,2}z_1 - z_1^{\,3} + a^2z_1 - 2y_1z_1^{\,2}\right)}{\left(y_1^{\,2} - z_1^{\,2} + a^2\right) + 4y_1^{\,2}z_1^{\,2}}$$

$$= \frac{\Gamma}{2\pi}\,\frac{\left(y_1^{\,2}z_1 - z_1^{\,3} + a^2z_1 - 2y_1z_1^{\,2}\right)}{\left(y_1^{\,2} - z_1^{\,2} + a^2\right) + 4y_1^{\,2}z_1^{\,2}} - i\,\frac{\Gamma}{2\pi}\,\frac{\left(y_1^{\,3} - y_1z_1^{\,2} + y_1a^2 + 2y_1z_1^{\,2}\right)}{\left(y_1^{\,2} - z_1^{\,2} + a^2\right) + 4y_1^{\,2}z_1^{\,2}}$$

In this manner, the real and imaginary parts of Equation (3-6) may be obtained as follows:

$$V_{RE_1} = -U_\infty \sin\alpha \,\frac{a^2}{r_1^{\,4}}\, 2y_1 z_1 - \frac{\Gamma}{2\pi}\,\frac{z_1\left(1 - \dfrac{a^2}{r_1^{\,2}}\right)}{\left(1 + \dfrac{a^2}{r_1^{\,2}}\right)^2 y_1^{\,2} + \left(1 - \dfrac{a^2}{r_1^{\,2}}\right)^2 z_1^{\,2}}$$

$$+ \frac{\Gamma}{2\pi}\,\frac{z_1}{r_1^{\,2} - a^2} + \frac{a\dot{a}y_1}{r_1^{\,2}} \qquad \text{(C-3)}$$

$$V_{IM_1} = U_\infty \sin\alpha \left[1 + \frac{a^2}{r_1^{\,4}}\left(y_1^{\,2} - z_1^{\,2}\right)\right]$$

$$+ \frac{\Gamma}{2\pi}\,\frac{y_1\left(1 + \dfrac{a^2}{r_1^{\,2}}\right)}{\left(1 + \dfrac{a^2}{r_1^{\,2}}\right)^2 y_1^{\,2} + \left(1 - \dfrac{a^2}{r_1^{\,2}}\right)^2 z_1^{\,2}} - \frac{\Gamma}{2\pi}\left(\frac{y_1}{r_1^{\,2} - a^2} + \frac{1}{2y_1}\right)$$

$$+ \frac{a\dot{a}}{r_1^{\,2}}\, z_1 \qquad \text{(C-4)}$$

where $r_1^{\,2} = y_1^{\,2} + z_1^{\,2}$.

An expression for $\Gamma$ may be obtained from Equation (3-11) of the text. From Equation (3-11),

$$\frac{\Gamma}{2\pi U \sin\alpha} = \frac{-\left(1 + \dfrac{a^2}{\zeta_0^{\,2}}\right)}{\dfrac{1}{\zeta_0 - \zeta_1} + \dfrac{1}{\zeta_0 + \dfrac{a^2}{\zeta_1}} - \dfrac{1}{\zeta_0 - \dfrac{a^2}{\bar{\zeta}_1}} - \dfrac{1}{\zeta_0 + \bar{\zeta}_1}} \qquad \text{(C-5)}$$

Again after considerable algebra, Equation (C-5) may be reduced to the form

$$\frac{\Gamma}{2\pi U_\infty \sin\alpha} = \frac{(\zeta_1 - \zeta_0)(\bar{\zeta}_1 - \bar{\zeta}_0)(\zeta_1 + \bar{\zeta}_0)(\bar{\zeta}_1 + \zeta_0)}{(\zeta_1\bar{\zeta}_1 - a^2)(\zeta_1 + \bar{\zeta}_1)} \tag{C-6}$$

Equation (C-6) may be differentiated with respect to time and divided by $\Gamma/2\pi U_\infty \sin\alpha$ to obtain the following relation

$$\frac{\dot{\Gamma}}{\Gamma} = \frac{\dot{\zeta}_1 - \dot{\zeta}_0}{\zeta_1 - \zeta_0} + \frac{\dot{\bar{\zeta}}_1 - \dot{\bar{\zeta}}_0}{\bar{\zeta}_1 - \bar{\zeta}_0} + \frac{\dot{\zeta}_1 + \dot{\bar{\zeta}}_0}{\zeta_1 + \bar{\zeta}_0} + \frac{\dot{\bar{\zeta}}_1 + \dot{\zeta}_0}{\bar{\zeta}_1 + \zeta_0}$$
$$- \frac{\dot{\zeta}_1\bar{\zeta}_1 + \zeta_1\dot{\bar{\zeta}}_1 - 2aa}{\zeta_1\bar{\zeta}_1 - a^2} - \frac{\dot{\zeta}_1 + \dot{\bar{\zeta}}_1}{\zeta_1 + \bar{\zeta}_1} \tag{C-7}$$

When the real and imaginary parts of $\zeta_1$ and $\zeta_0$ are put into Equation (C-7) and the expression reduced in form, the imaginary terms cancel and the following final expression is obtained:

$$\frac{\dot{\Gamma}}{\Gamma} = 2\,\frac{(\dot{y}_1 - \dot{y}_0)(y_1 - y_0) + (\dot{z}_1 - \dot{z}_0)(z_1 - z_0)}{(y_1 - y_0)^2 + (z_1 - z_0)^2}$$
$$+ \frac{(\dot{y}_1 + \dot{y}_0)(y_1 + y_0) + (\dot{z}_1 - \dot{z}_0)(z_1 - z_0)}{(y_1 + y_0)^2 + (z_1 - z_0)^2}$$
$$+ 2\,\frac{y_1\dot{y}_1 + z_1\dot{z}_1 - a\dot{a}}{y_1^2 + z_1^2 - a^2} - \frac{\dot{y}_1}{y_1} \tag{C-8}$$

Equations (C-1) and (C-2) may now be written, with the aid of Equations (C-3), (C-4), and (C-8), in the form

$$\dot{y}_1 + f(y_1, y_0, \dot{y}_0, z_1, z_0, \dot{z}_0) = 0 \qquad \text{(C-9)}$$

$$\dot{z}_1 + g(y_1, y_0, \dot{y}_0, z_1, z_0, \dot{z}_0) = 0 \qquad \text{(C-10)}$$

These equations were solved with a finite difference method on a digital computer and known inputs of $y_0$, $z_0$, $\dot{y}_0$, and $\dot{z}_0$ as a function of time. The latter four quantities are a function of the body radius variation with axial distance and an assumed variation of the angular location on the body of the separation point.

The expression for the viscous normal force per unit length was obtained from Equation (3-14) in the text by separating that equation into real and imaginary parts. Thus,

$$\frac{dN_V}{dx} = \frac{d}{dt}\left[i\rho\Gamma\left(y_1 + iz_1 + y_1 - iz_1 - \frac{a^2}{y_1 - iz_1} - \frac{a^2}{y_1 + iz_1}\right)\right]$$

or performing the separation

$$\frac{dN_V}{dx} = \frac{d}{dt}\left[i\rho\Gamma\left(2y_1 - 2\,\frac{a^2 y_1}{y_1^2 + z_1^2}\right)\right]$$

$$= \frac{d}{dt}\left[2i\rho\Gamma y_1\left(1 - \frac{a^2}{r_1^2}\right)\right]$$

Performing the differentiation and dropping the $i$, since the orientation of the force will be assumed along the vertical, or imaginary, axis, there results

$$\frac{dN_V}{dx} = 2\rho y_1 \left[ \dot{\Gamma}\left(1 - \frac{a^2}{r_1^{\,2}}\right) + \Gamma \dot{y}_1 \left( \frac{1 - \frac{a^2}{r_1^{\,2}}}{y_1} + \frac{2a^2 y_1}{r_1^{\,4}} \right) \right.$$

$$\left. - \frac{2\Gamma a \dot{a}}{r_1^{\,2}} + \frac{2\Gamma a^2 z_1 \dot{z}_1}{r_1^{\,4}} \right] \qquad \text{(C-11)}$$

Thus, at each value of time in the computation the value of each of the variables on the right-hand side of Equation (C-11) is known, and the viscous normal force per unit length can be determined as a function of $x$. It is possible also to take the product of a local viscous normal force per unit length and the axial distance to the center of gravity of the body and integrate this product over the separated length of the body to obtain the viscous pitching moment. The total viscous normal force may be obtained more directly as follows. From Equations (3-14) and (3-3),

$$N_V = \int_{x_s}^{l} \frac{dN_V}{dx}\, dx = \int_{x_s}^{l} \frac{dI}{dt}\, dx = \int_{0}^{t_l} \frac{dI}{dt} \frac{dx}{dt}\, dt$$

$$= \int_{0}^{t_l} \frac{dI}{dt} U_\infty \cos\alpha \, dt = U_\infty \cos\alpha \int_{0}^{I_l} dI$$

$$= U_\infty \cos\alpha \,(I)_{x=l} \qquad \text{(C-12)}$$

Thus, the value of the impulse at the rear of the body determines the total viscous normal force induced on the body by the shed vortex system.

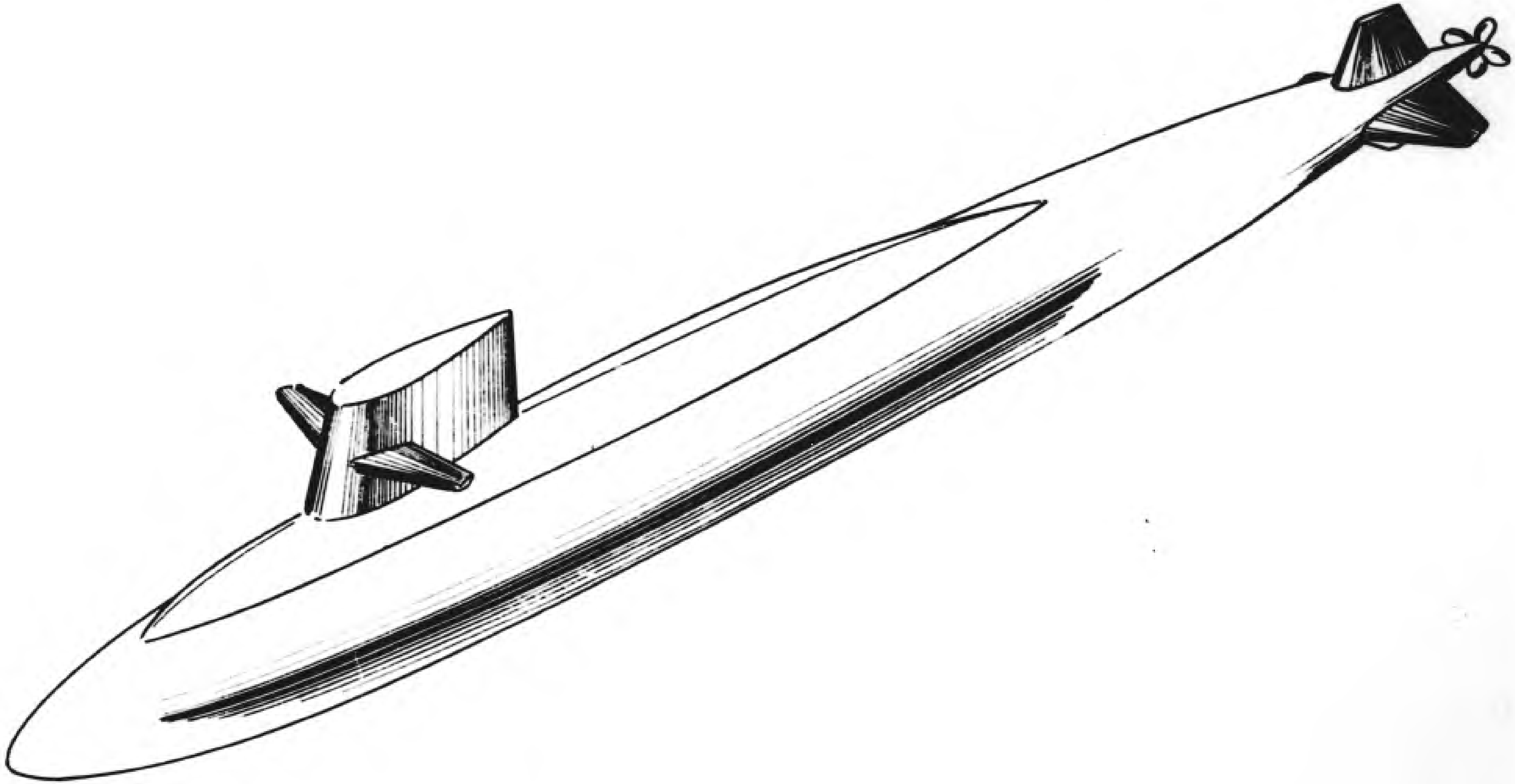

Figure 1.- Typical high-speed submarine configuration.

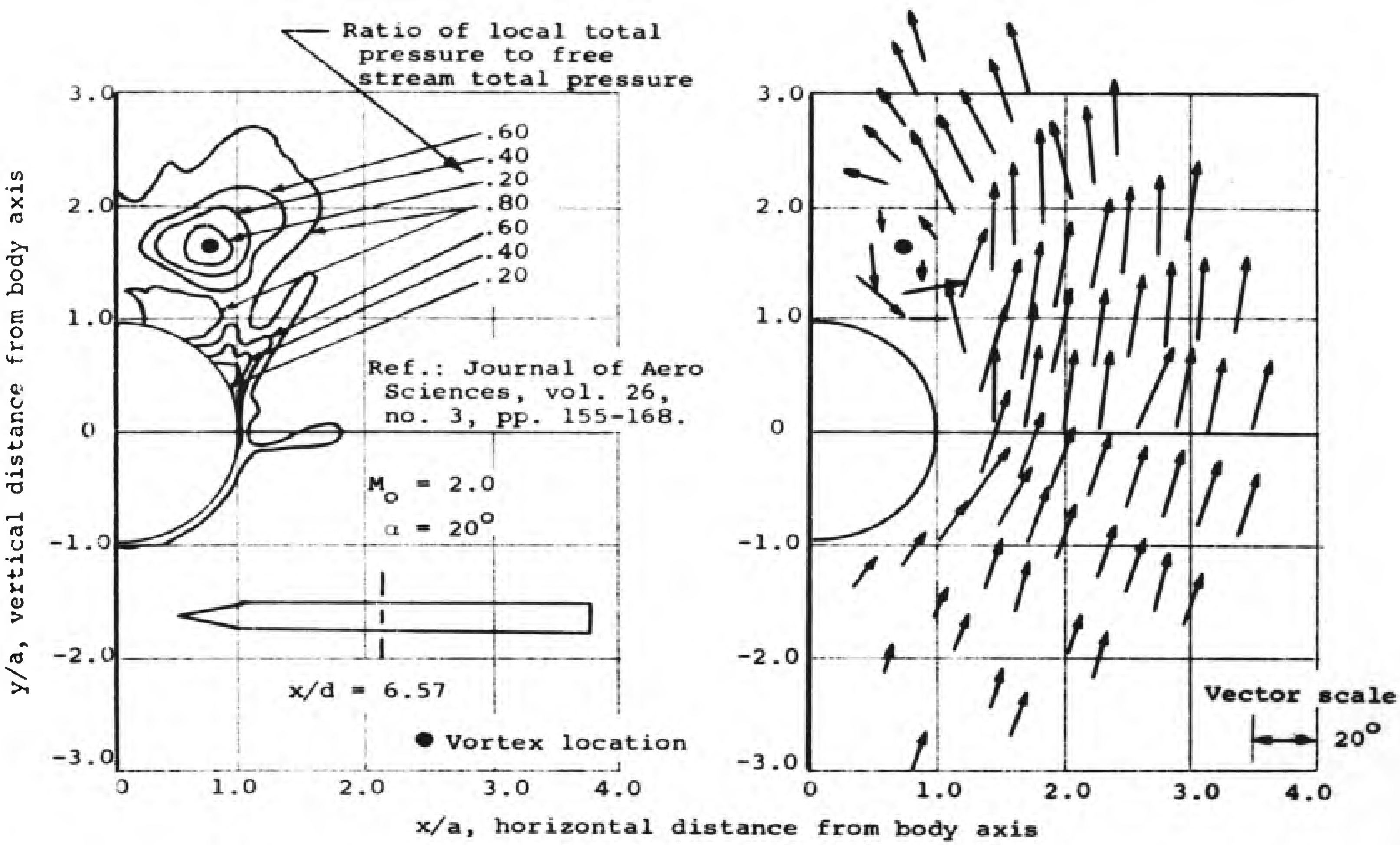


Figure 2.- Experimental total pressure ratio contours and local flow inclination.

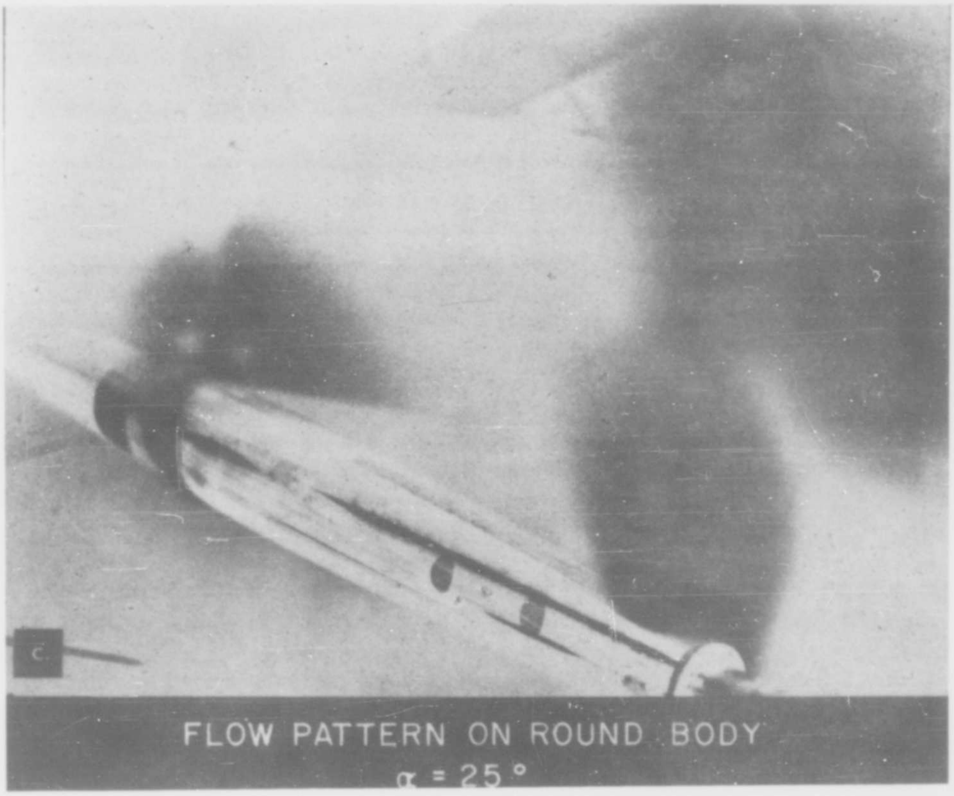


Velocity - 50 ft/sec

Angle of attack - $25^{\circ}$

Reference - RAE TN AERO 2482

Figure 3.- Smoke-screen photograph of vortex separation.

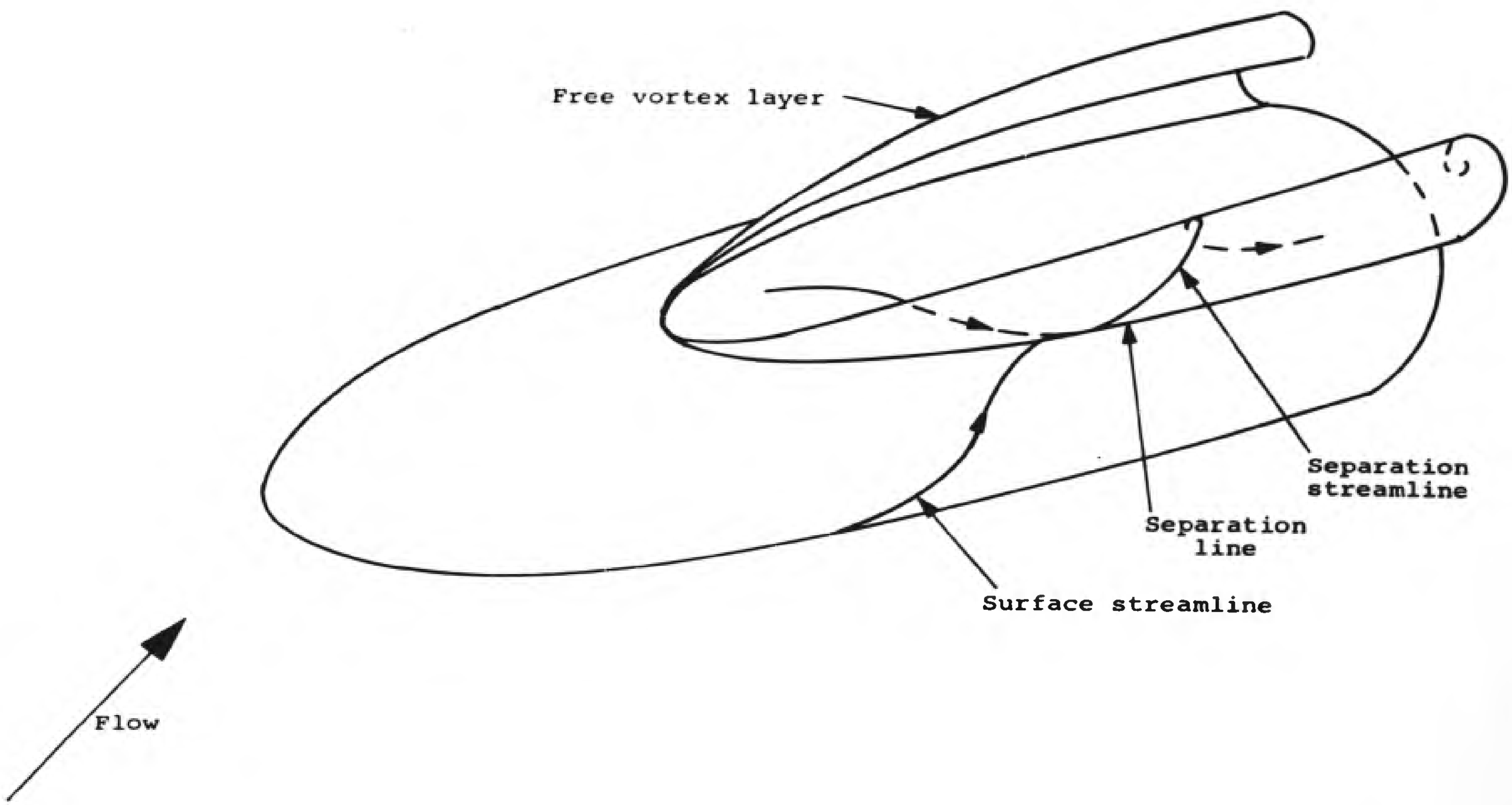


Figure 4.- Flow separation from a curved surface with vortex layer formation.

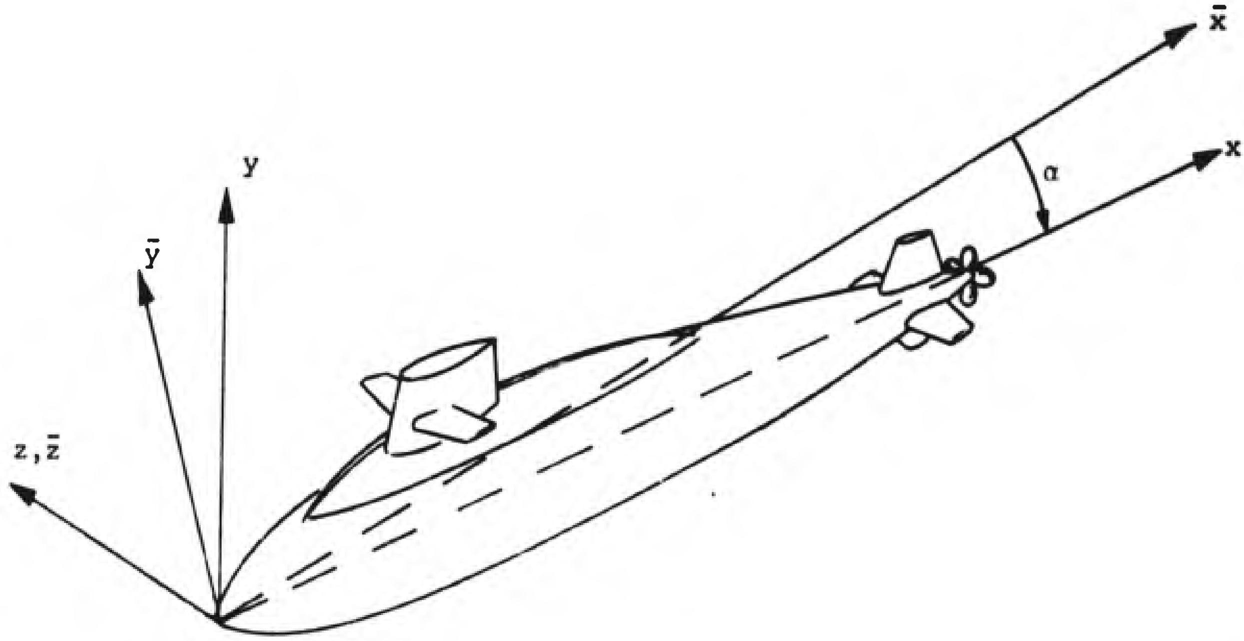


Figure 5.- Coordinate systems.

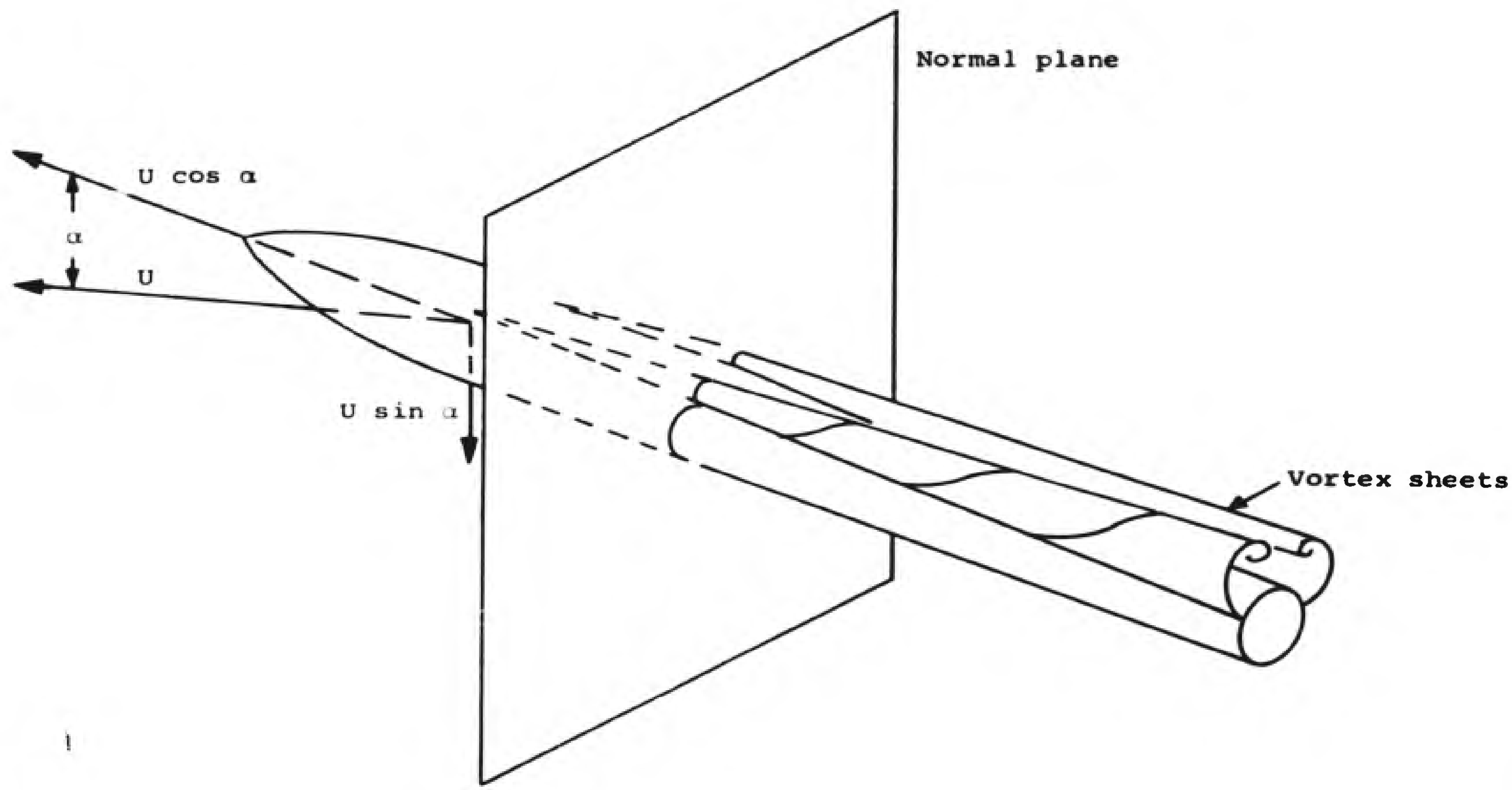


Figure 6.- Symmetric vortex shedding on a slender body of revolution at high angle of attack.

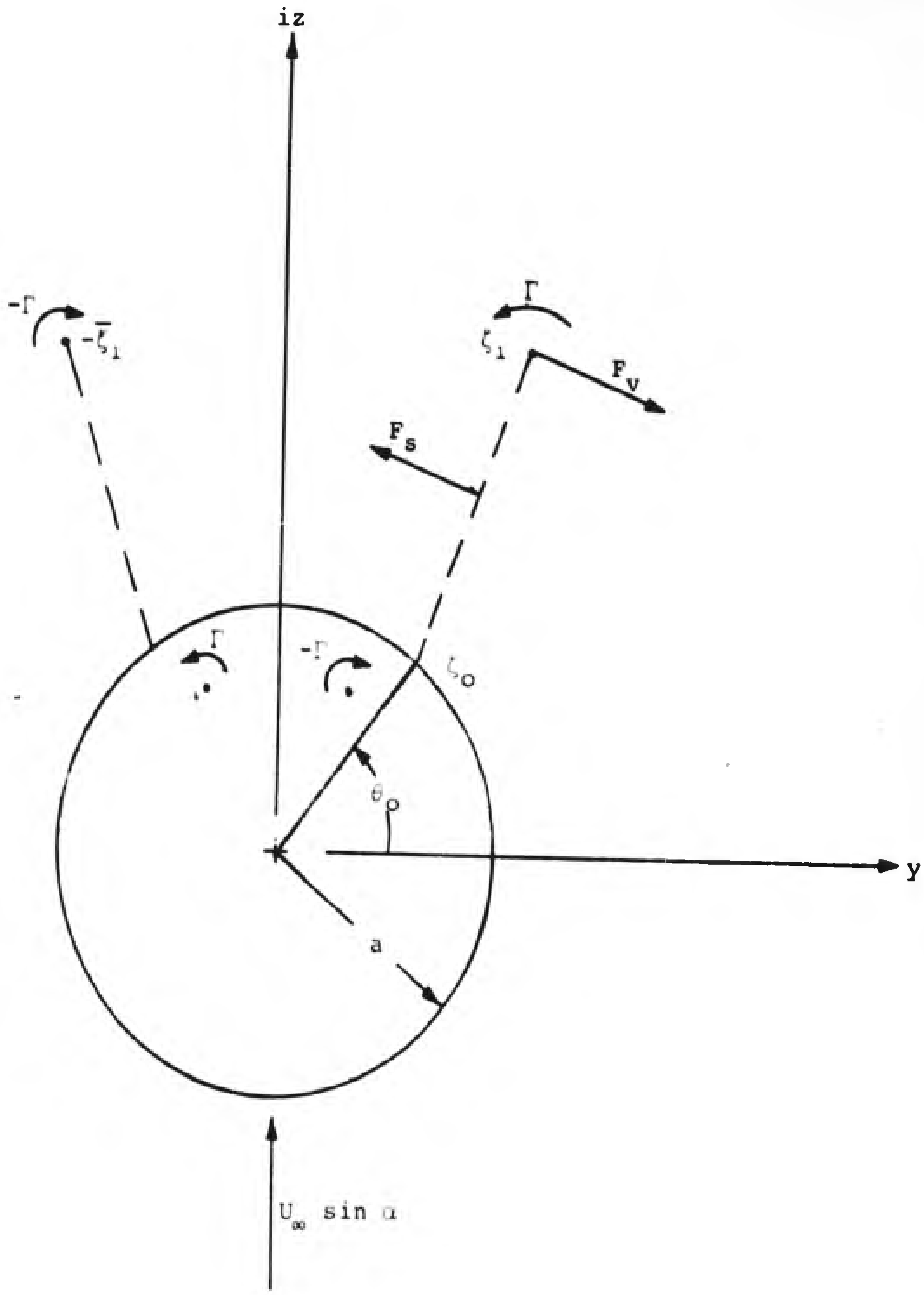


Figure 7.- Normal plane flow model.

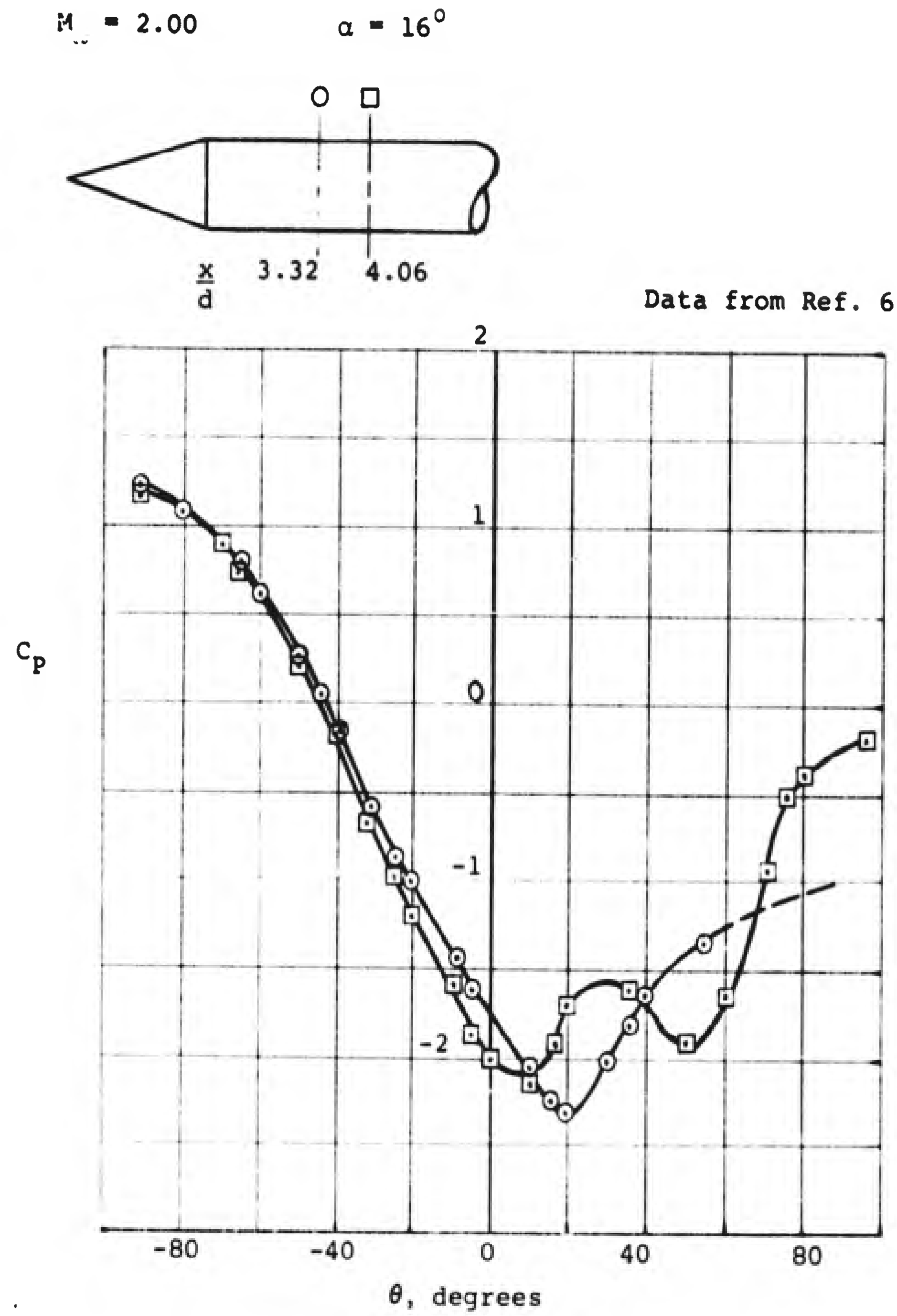


Figure 8. - Typical effects of incipient vortex formation on the circumferential variation of the static pressure coefficient.

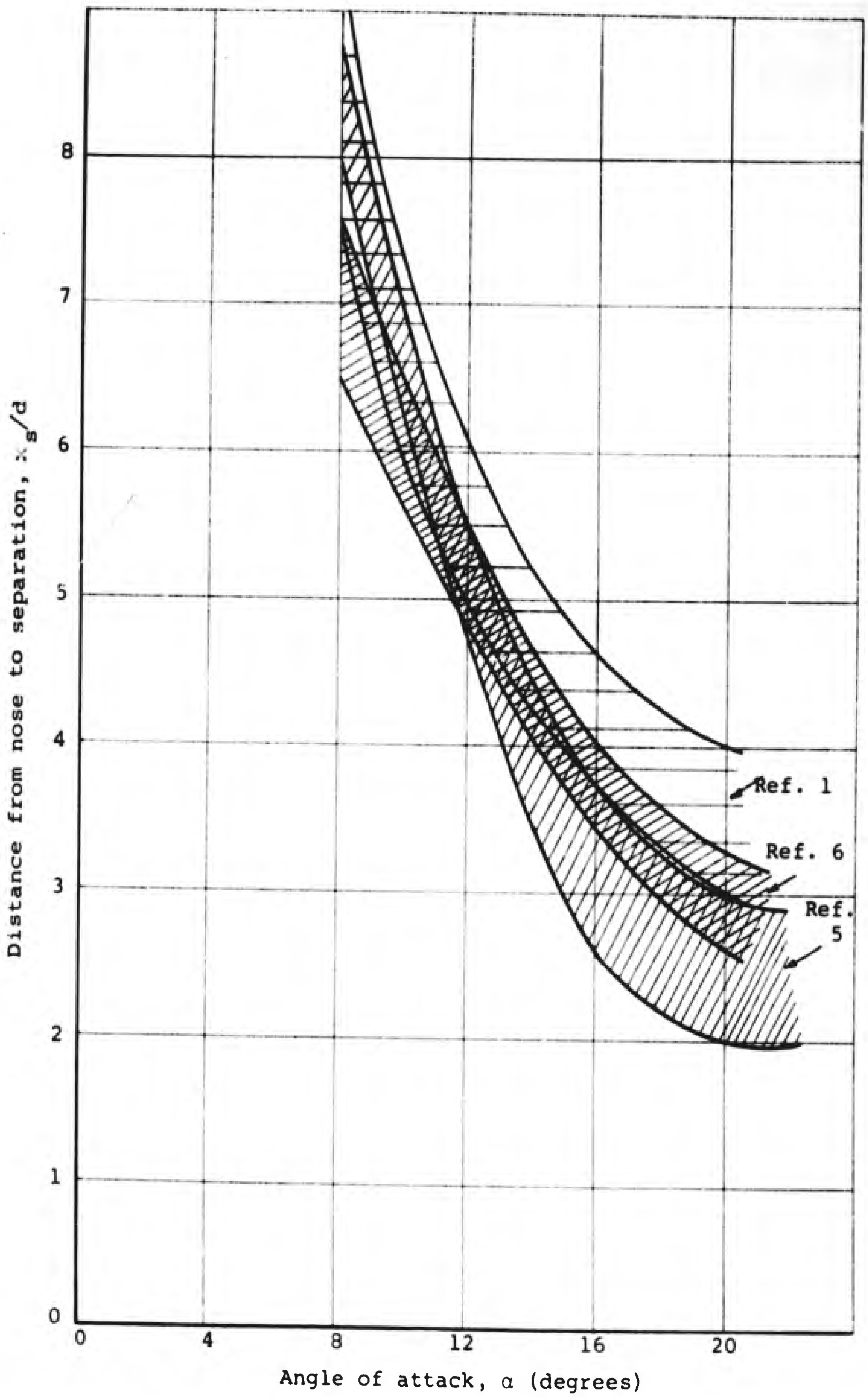


Figure 9.- Axial location of the origin of separation on inclined bodies of revolution.

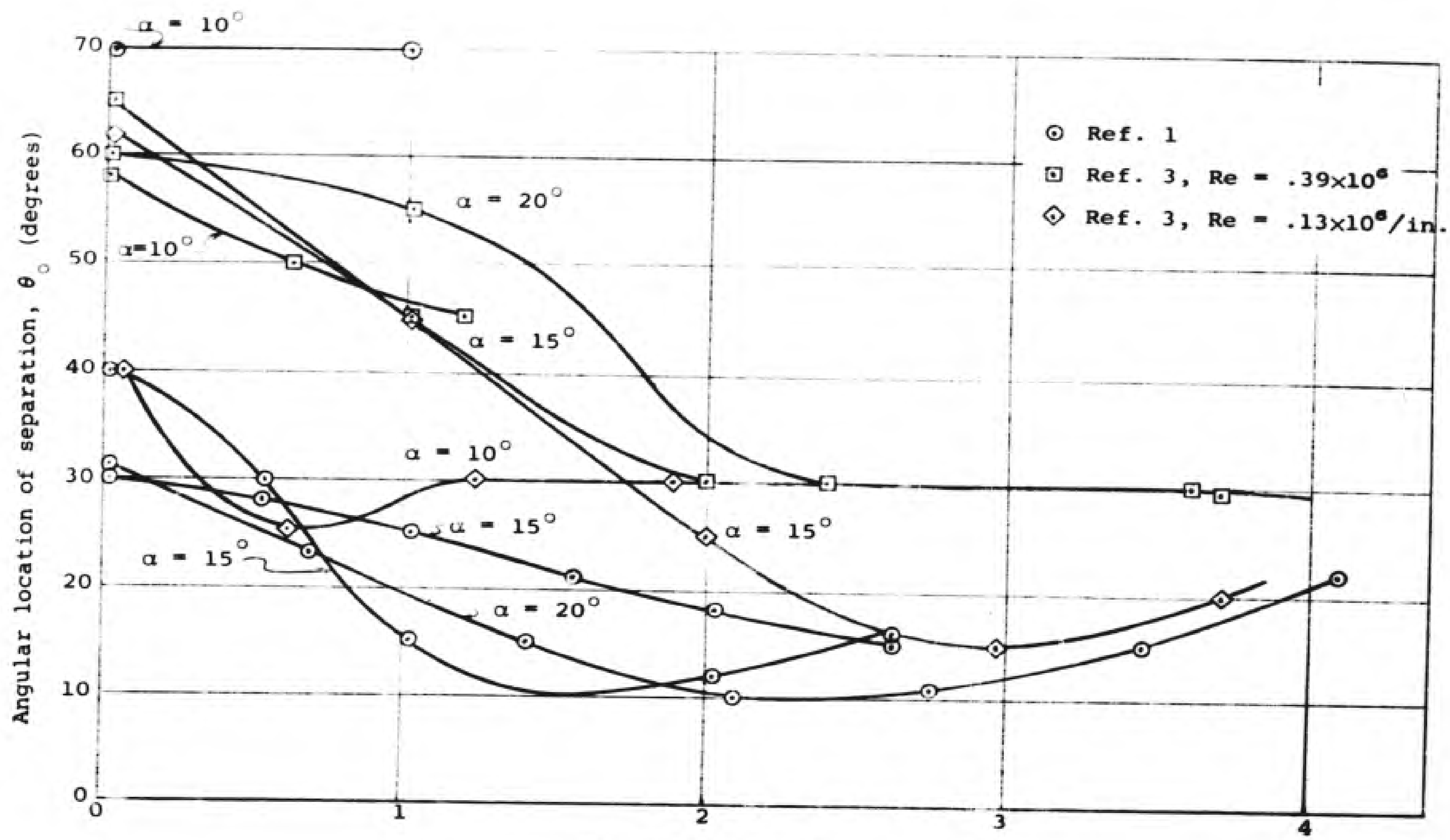


Distance along body, $(x - x_s/a)\ \alpha$

(a) Supersonic flow.

Figure 10. - Experimental data on angular location of separation on inclined bodies of revolution.

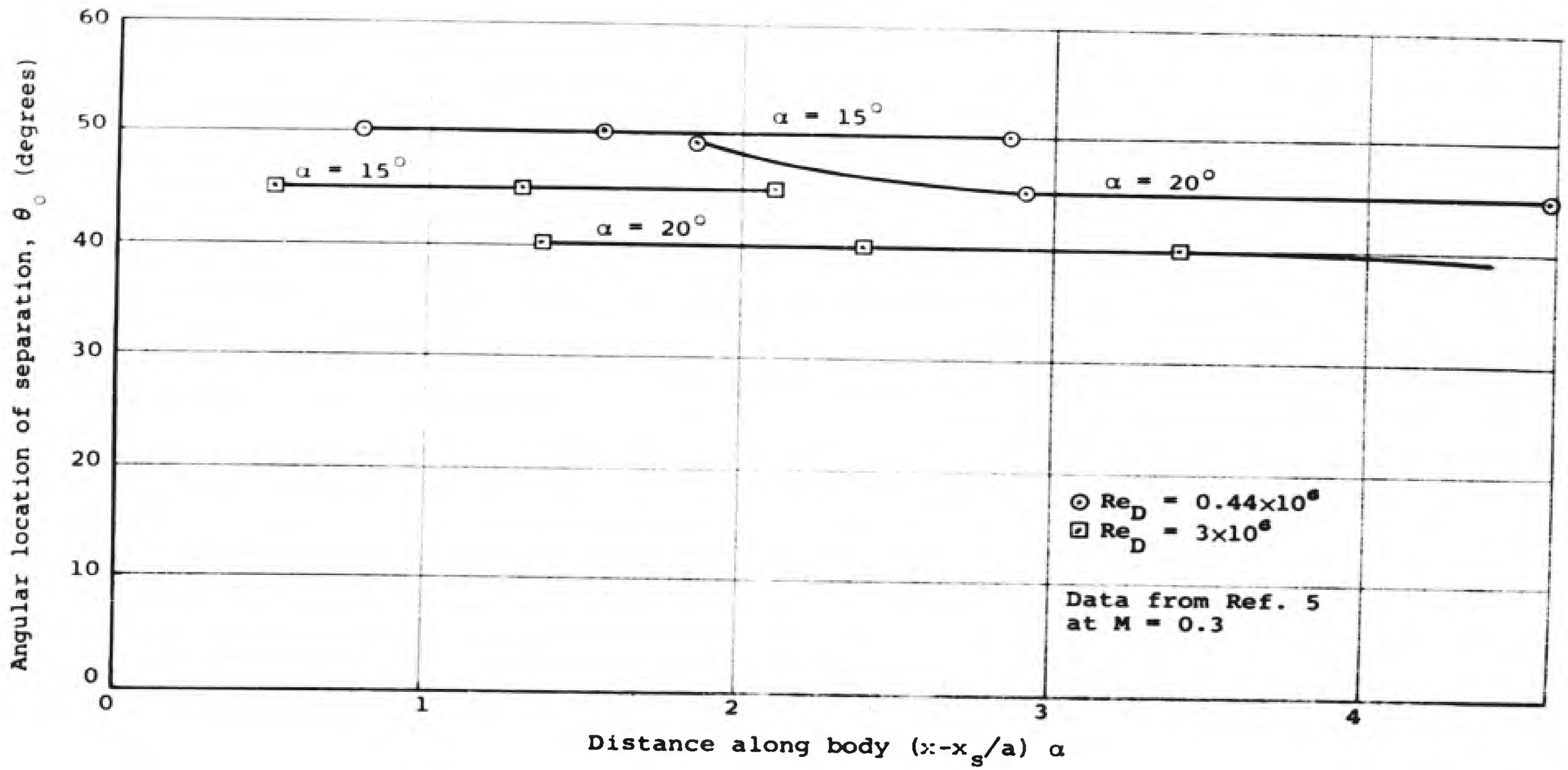


(b) Subsonic flow.

Figure 10.-Concluded.

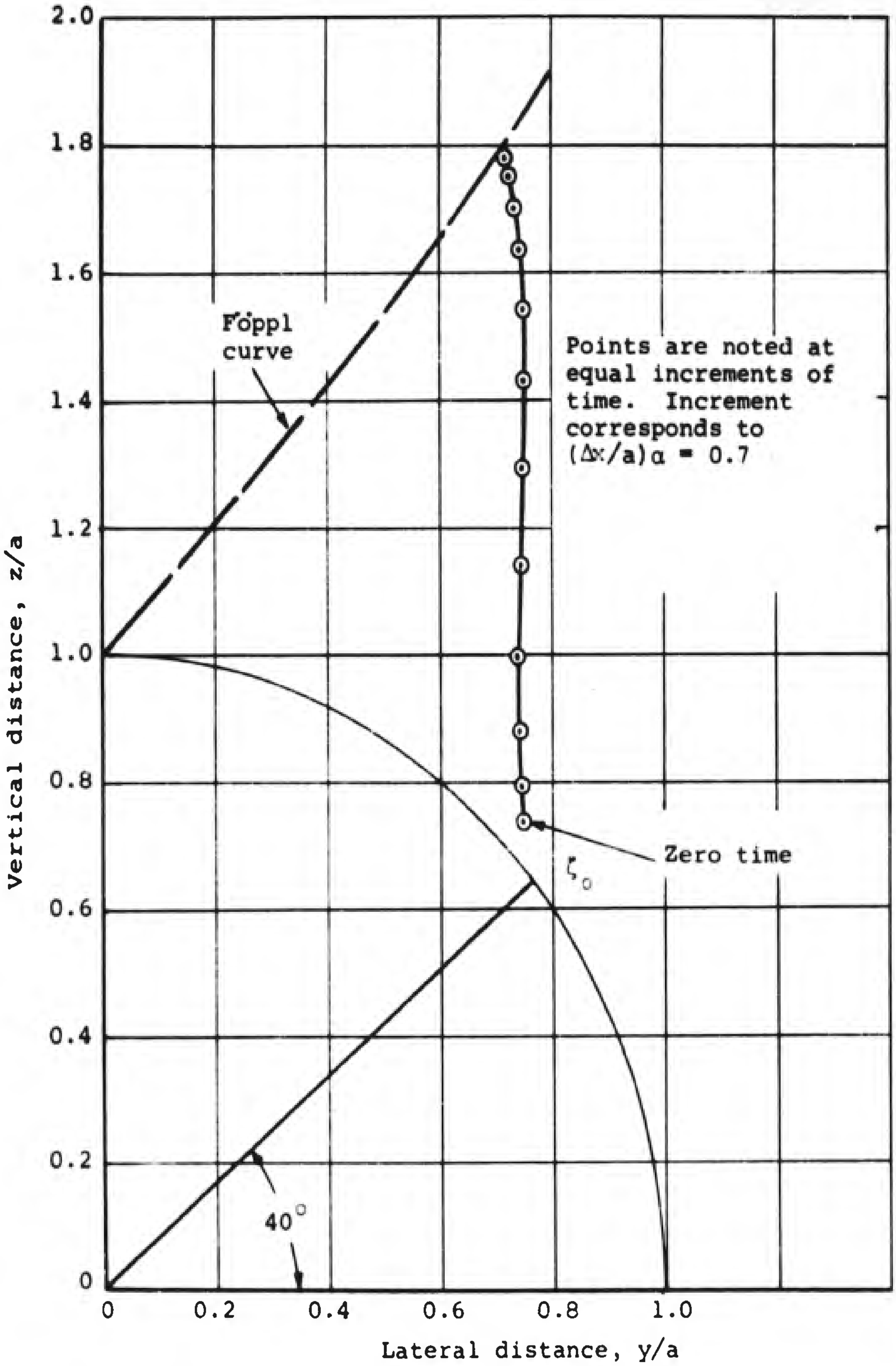


(a) Initial behavior.

Figure 11.-Theoretical vortex path in the normal plane.

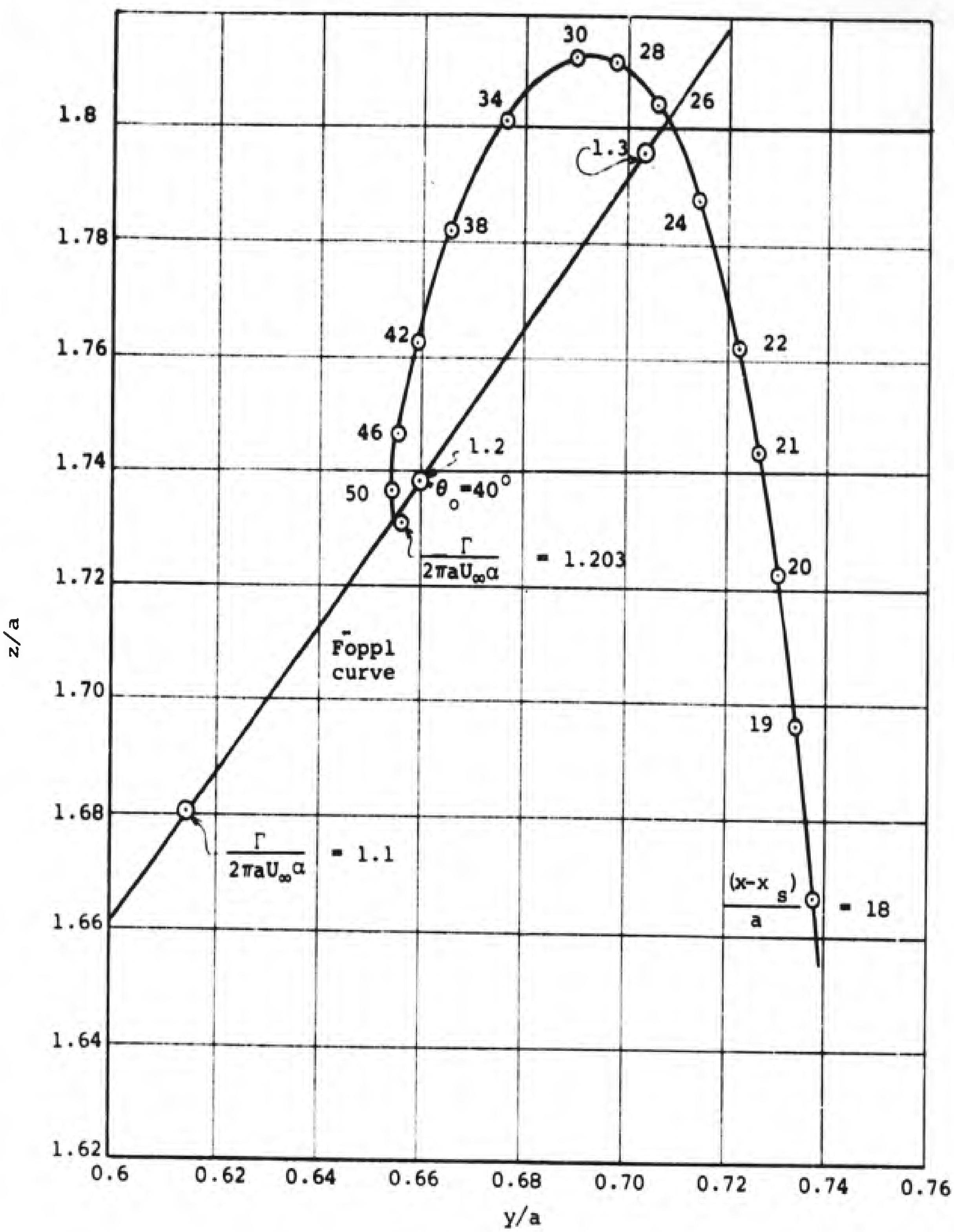


(b) Asymptotic behavior.

Figure 11.-Concluded.

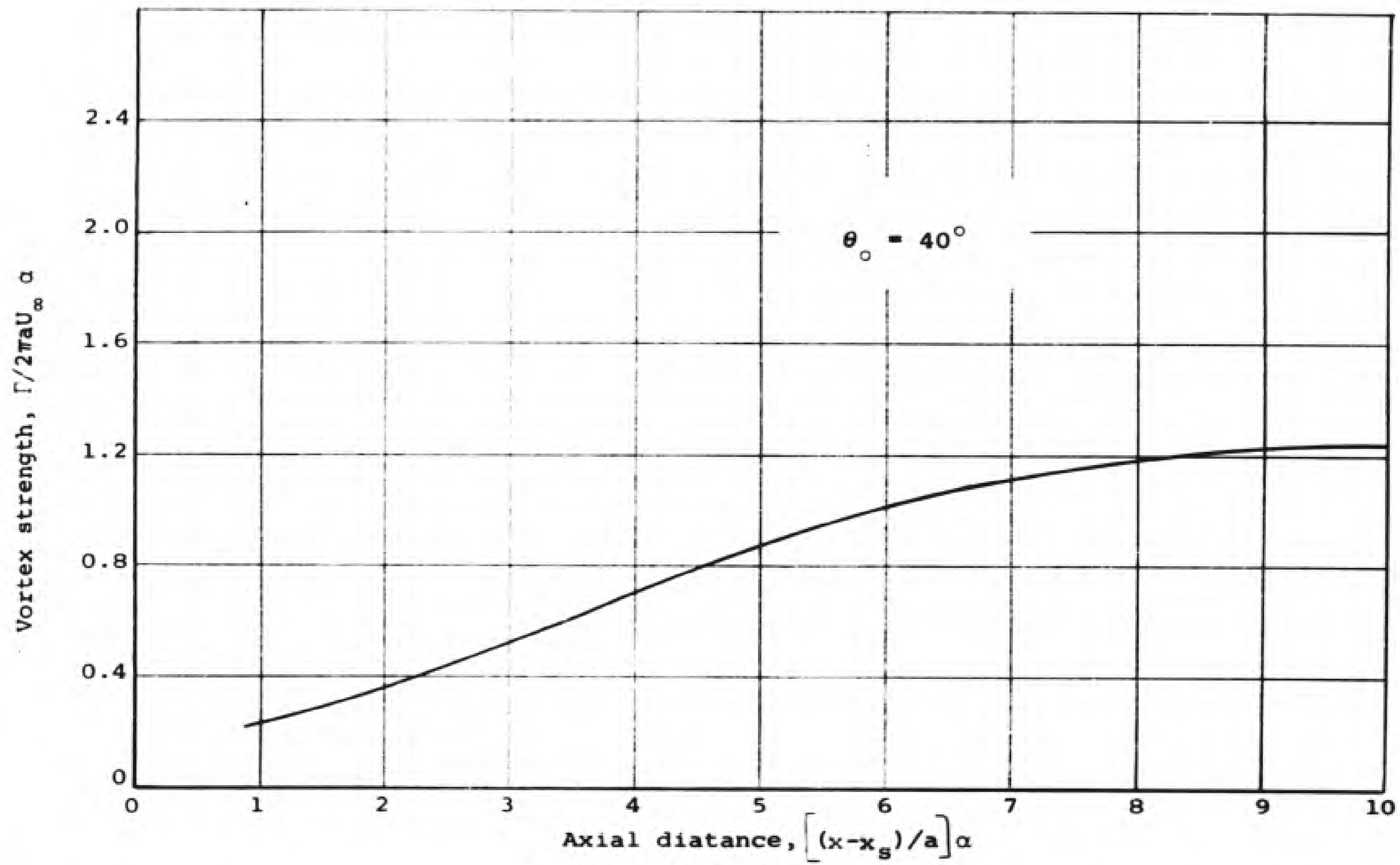


Figure 12.-Theoretical variation of vortex strength with axial distance for pointed cylinder.

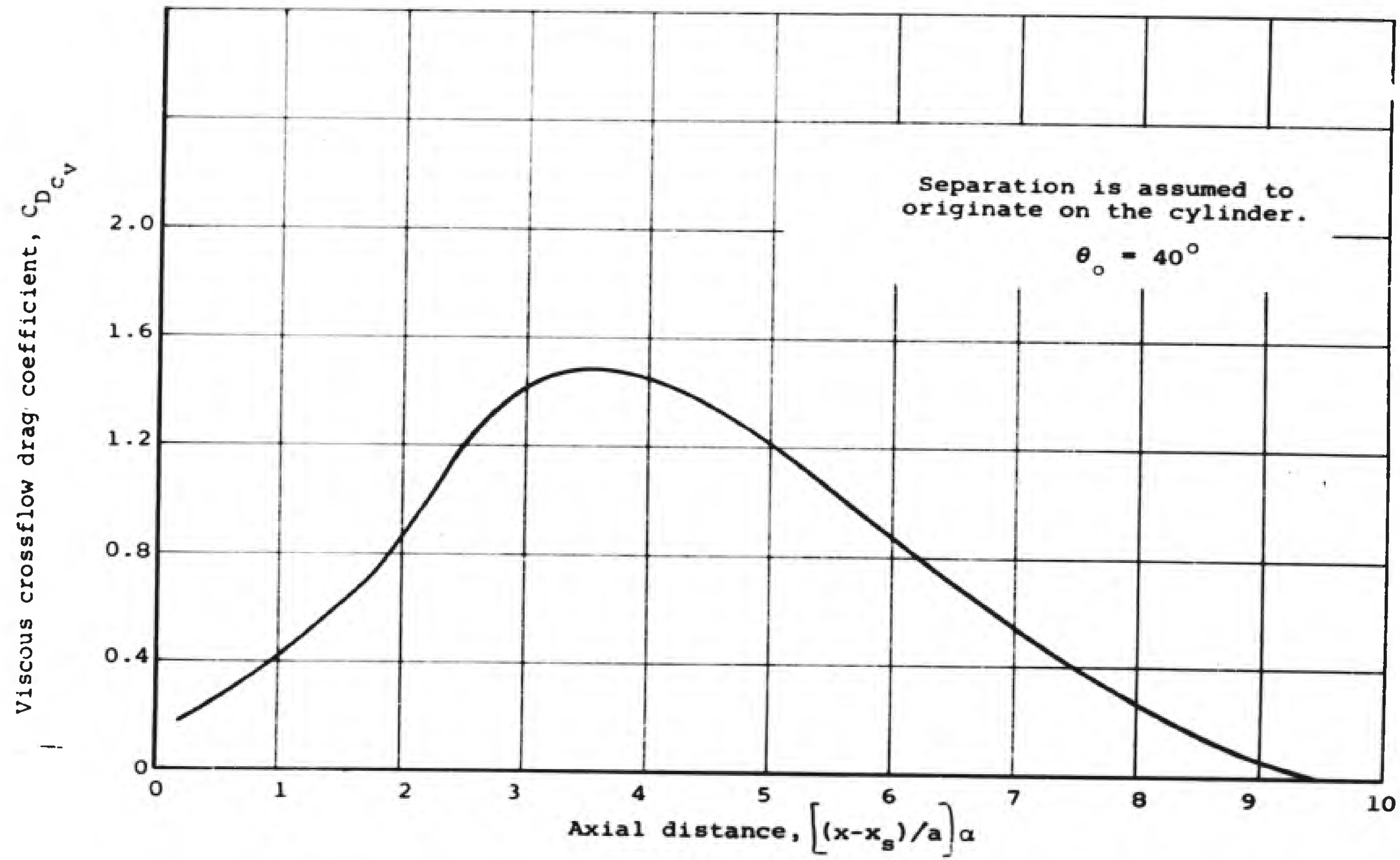


Figure 13.- Viscous crossflow drag coefficient versus distance for a pointed cylinder.

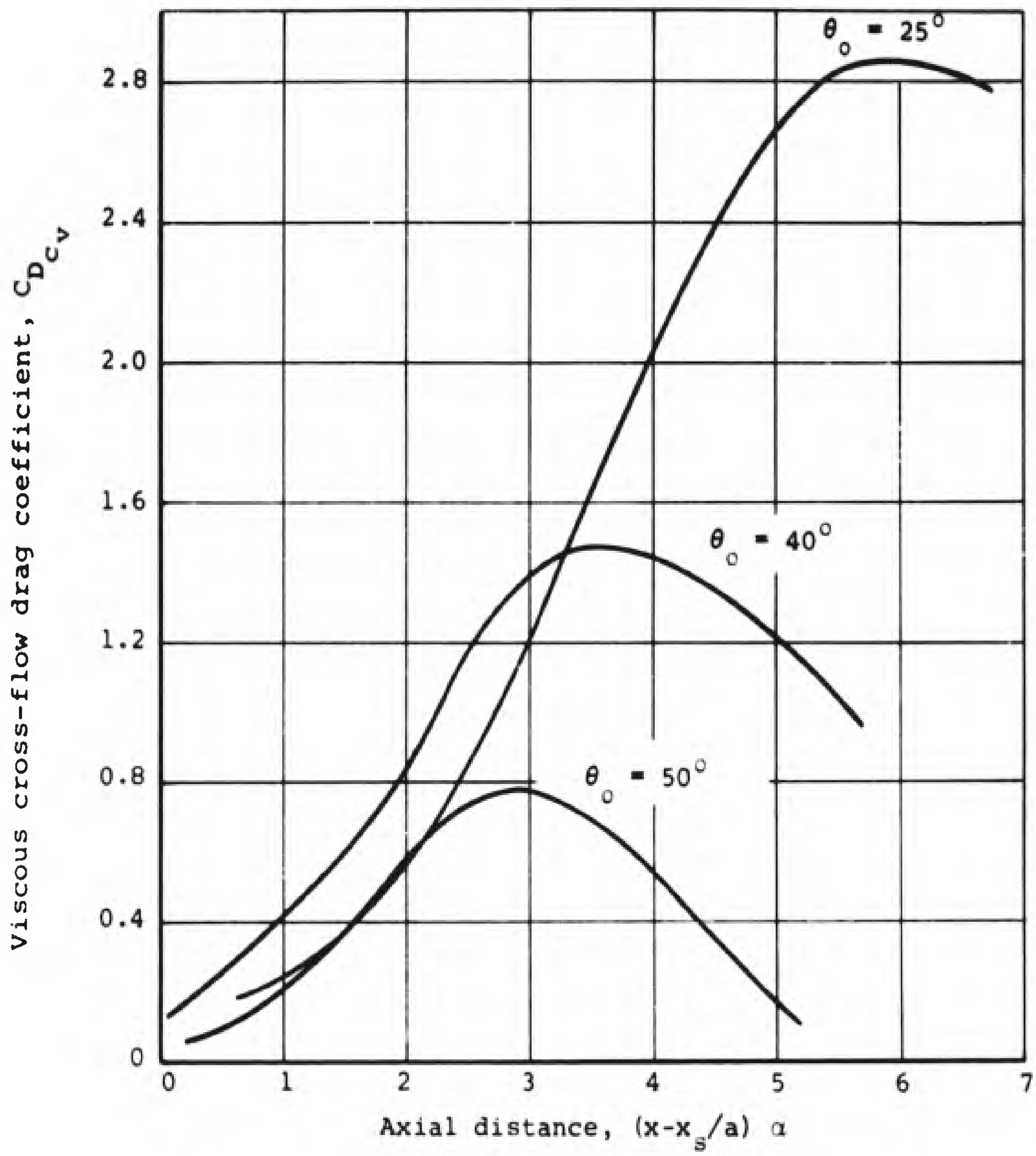


Figure 14. - Theoretical effect of separation angle on viscous cross-flow drag coefficient for pointed cylinder.

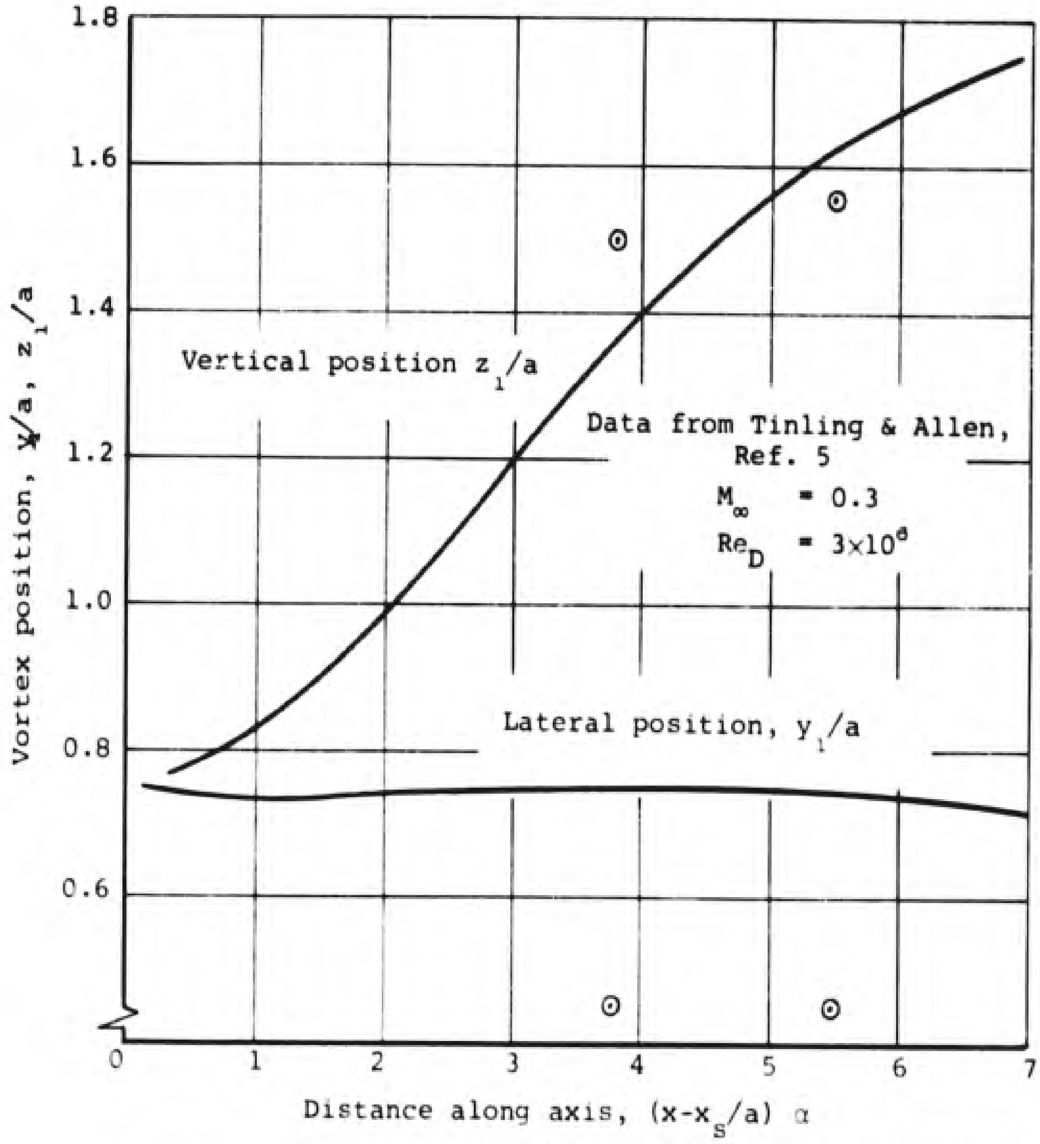


Figure 15. - Comparison of theoretical vortex position with data for ogive cylinder.

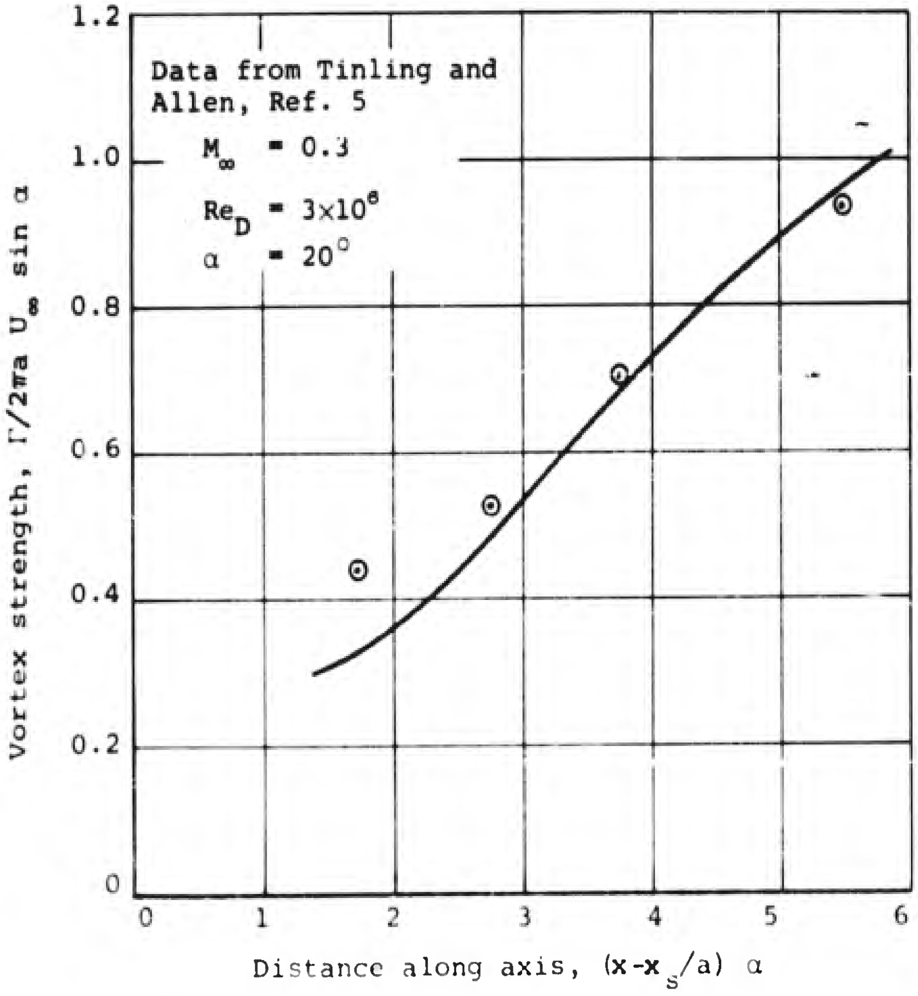


Figure 16. - Comparison of theoretical vortex strength with data for ogive cylinder.

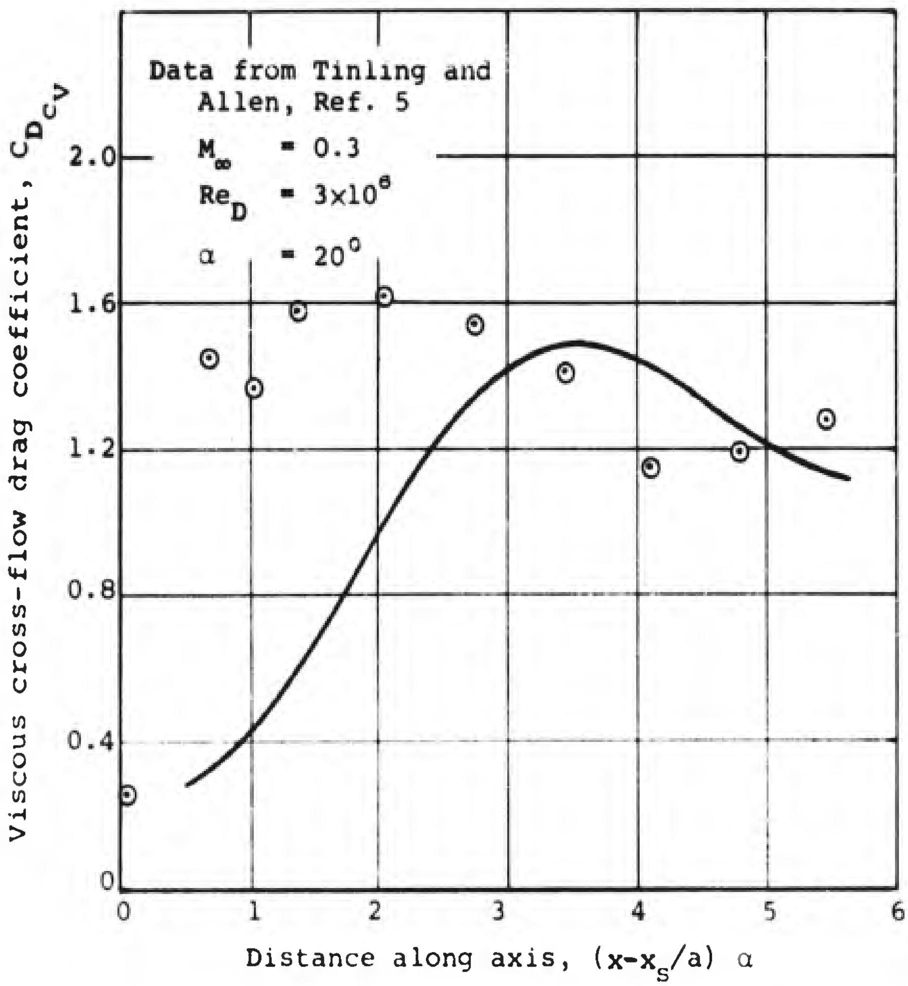


Figure 17. - Comparison of theoretical viscous cross-flow drag coefficient with data for ogive cylinder.

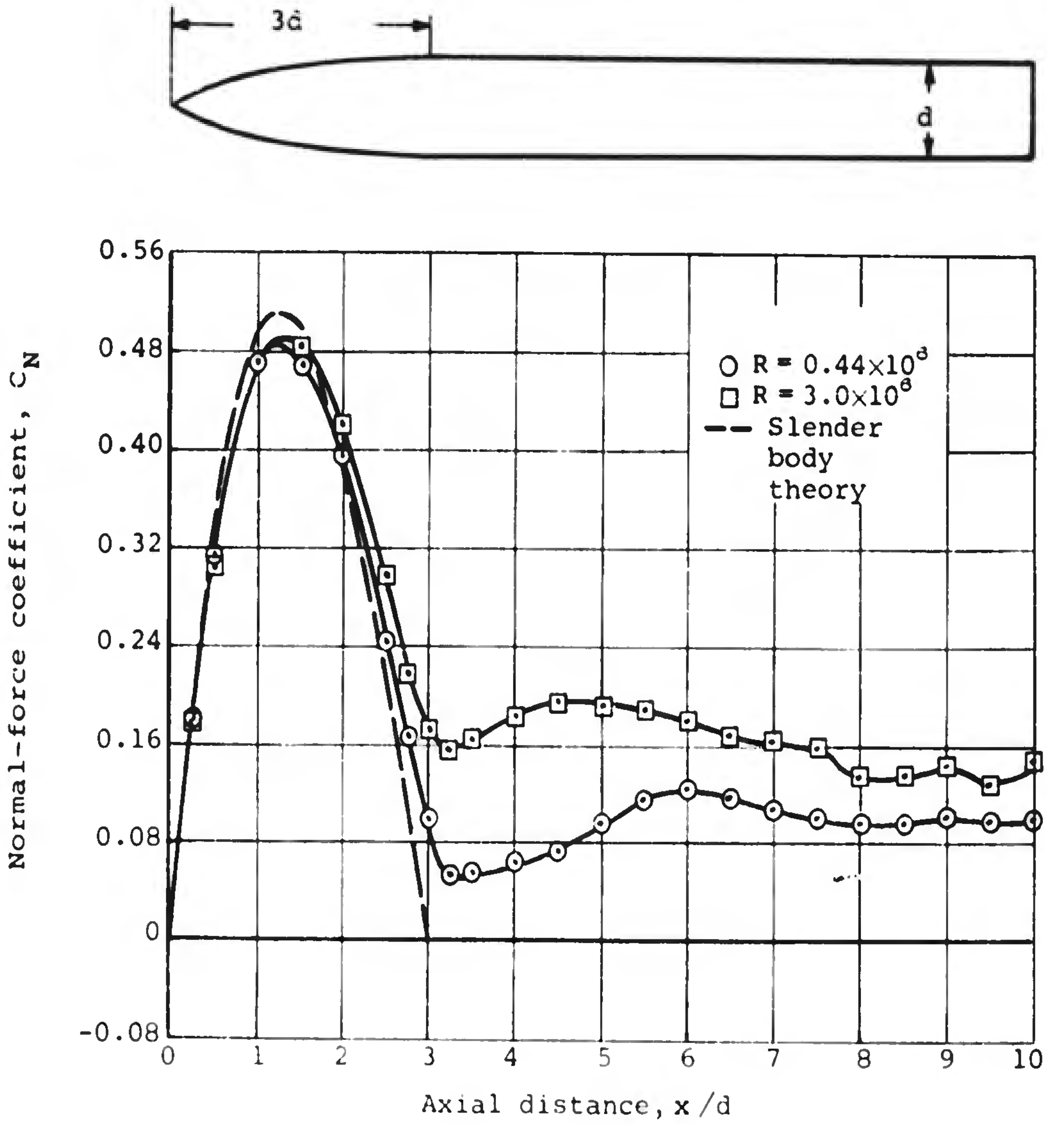


Figure 18. - Data from Reference 5, $\alpha = 20^\circ$, M = 0.3 on normal force.

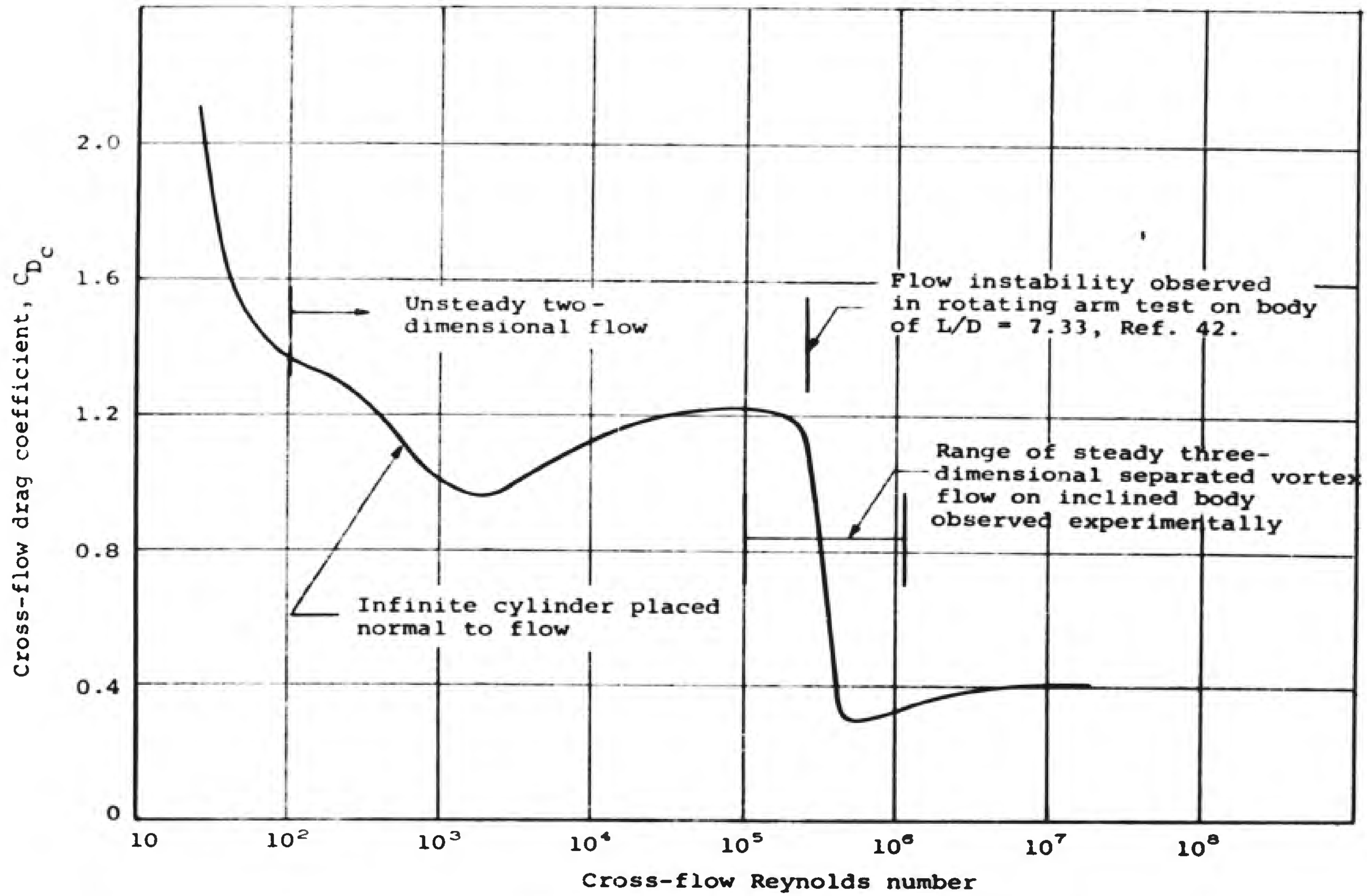


Figure 19. - Cross-flow drag coefficients for various bodies.

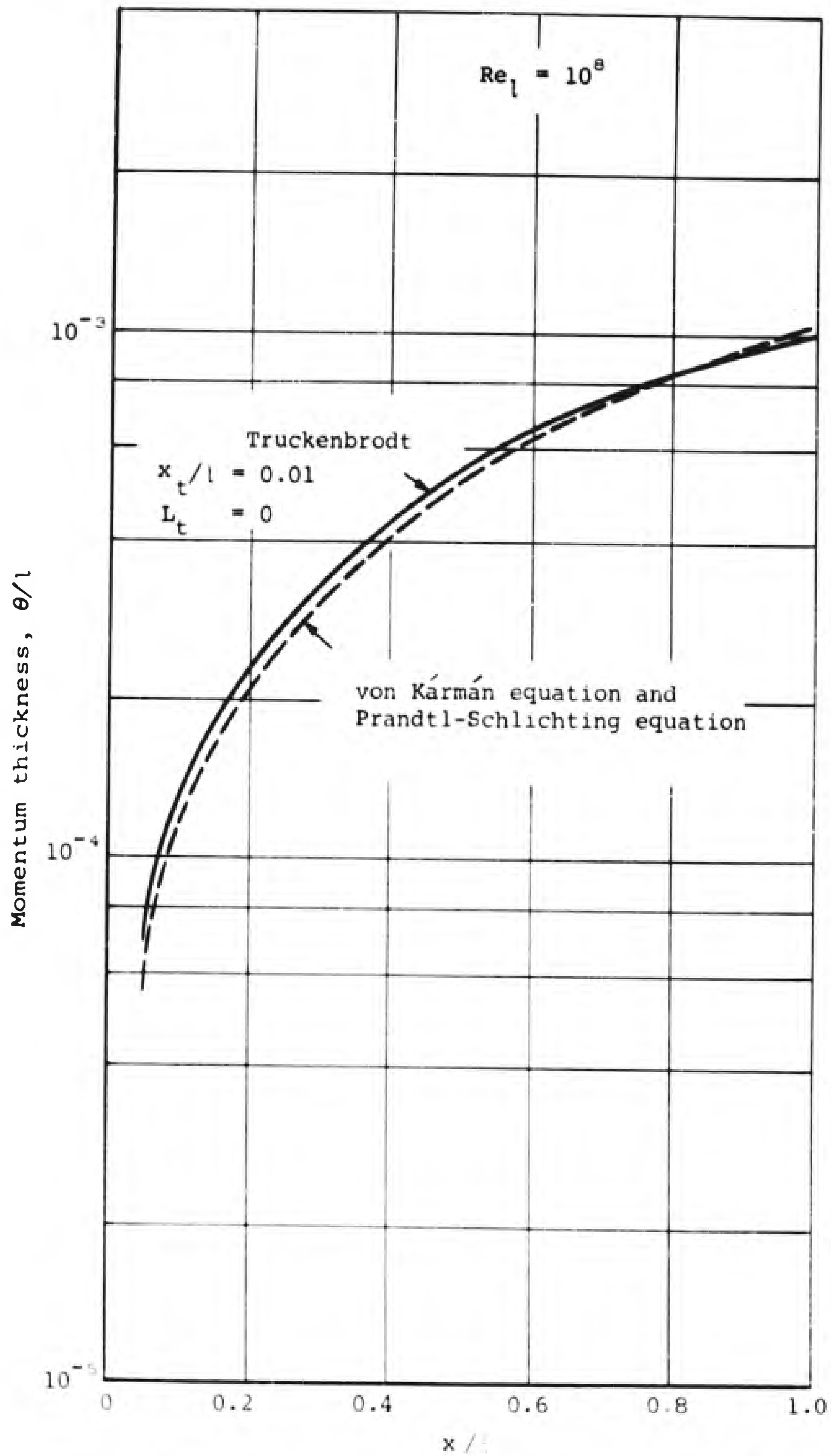


Figure 20. - Comparison of momentum thickness for flat plate.

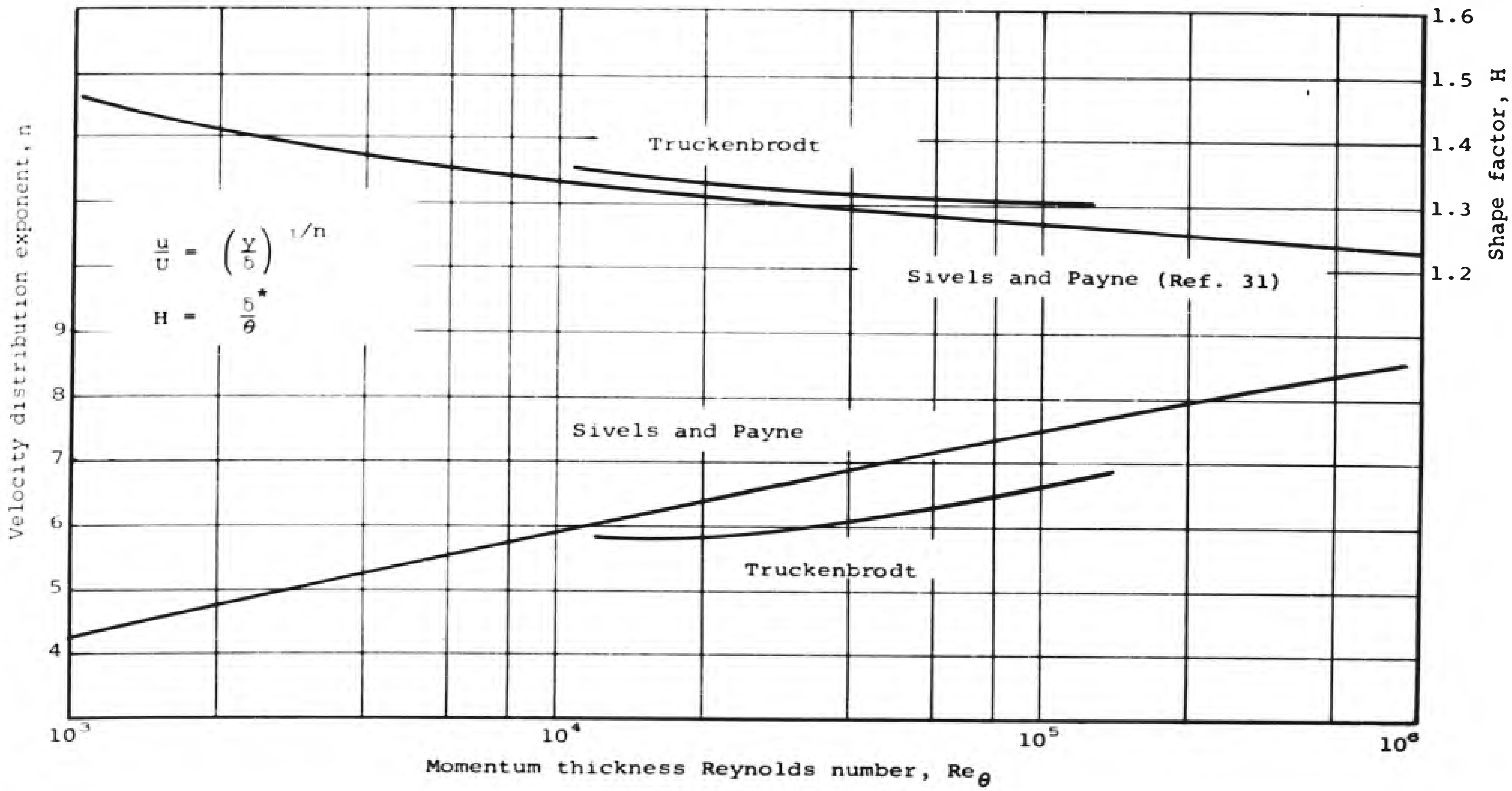


Figure 21. - Flat-plate turbulent incompressible boundary-layer comparisons.

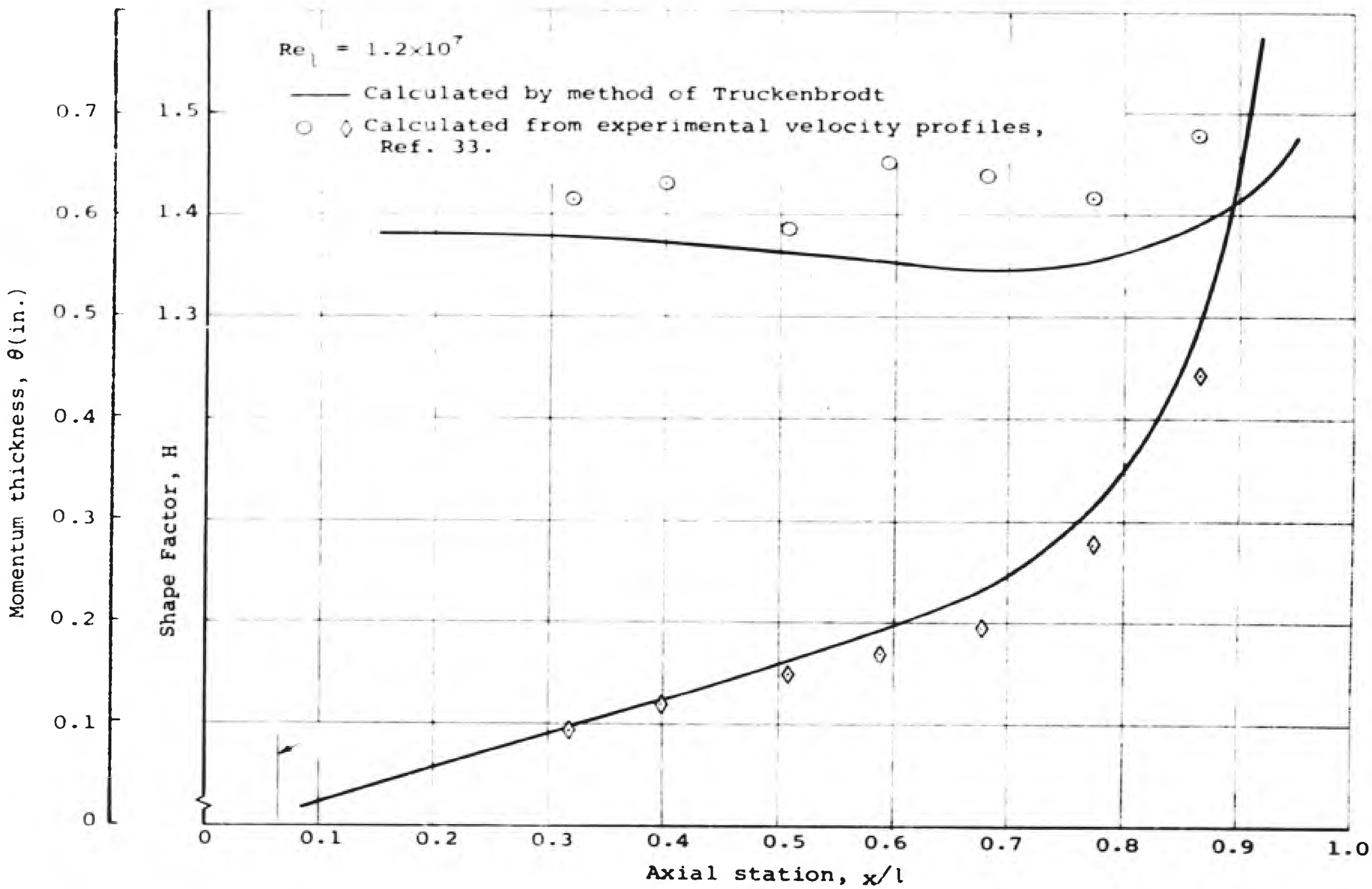


Figure 22. - Boundary-layer characteristics on USS Akron airship model.

| x/l | a/d | x/l | a/d |
|---|---|---|---|
| 0.00 | 0.00 | 0.52 | 0.482 |
| .02 | .143 | .54 | .476 |
| .04 | .203 | .56 | .468 |
| .06 | .249 | .58 | .460 |
| .08 | .287 | .60 | .451 |
| .10 | .320 | .62 | .441 |
| .12 | .349 | .64 | .431 |
| .14 | .373 | .66 | .419 |
| .16 | .395 | .68 | .406 |
| .18 | .415 | .70 | .392 |
| .20 | .431 | .72 | .377 |
| .22 | .446 | .74 | .361 |
| .24 | .458 | .76 | .343 |
| .26 | .469 | .78 | .324 |
| .28 | .478 | .80 | .304 |
| .30 | .485 | .82 | .282 |
| .32 | .491 | .84 | .258 |
| .34 | .495 | .86 | .233 |
| .36 | .498 | .88 | .206 |
| .38 | .499 | .90 | .177 |
| .40 | .500 | .92 | .146 |
| .42 | .499 | .94 | .113 |
| .44 | .498 | .96 | .078 |
| .46 | .495 | .98 | .040 |
| .48 | .492 | 1.00 | .00 |
| .50 | .488 | | |

Figure 23.- Hull offsets of representative submarine configuration.

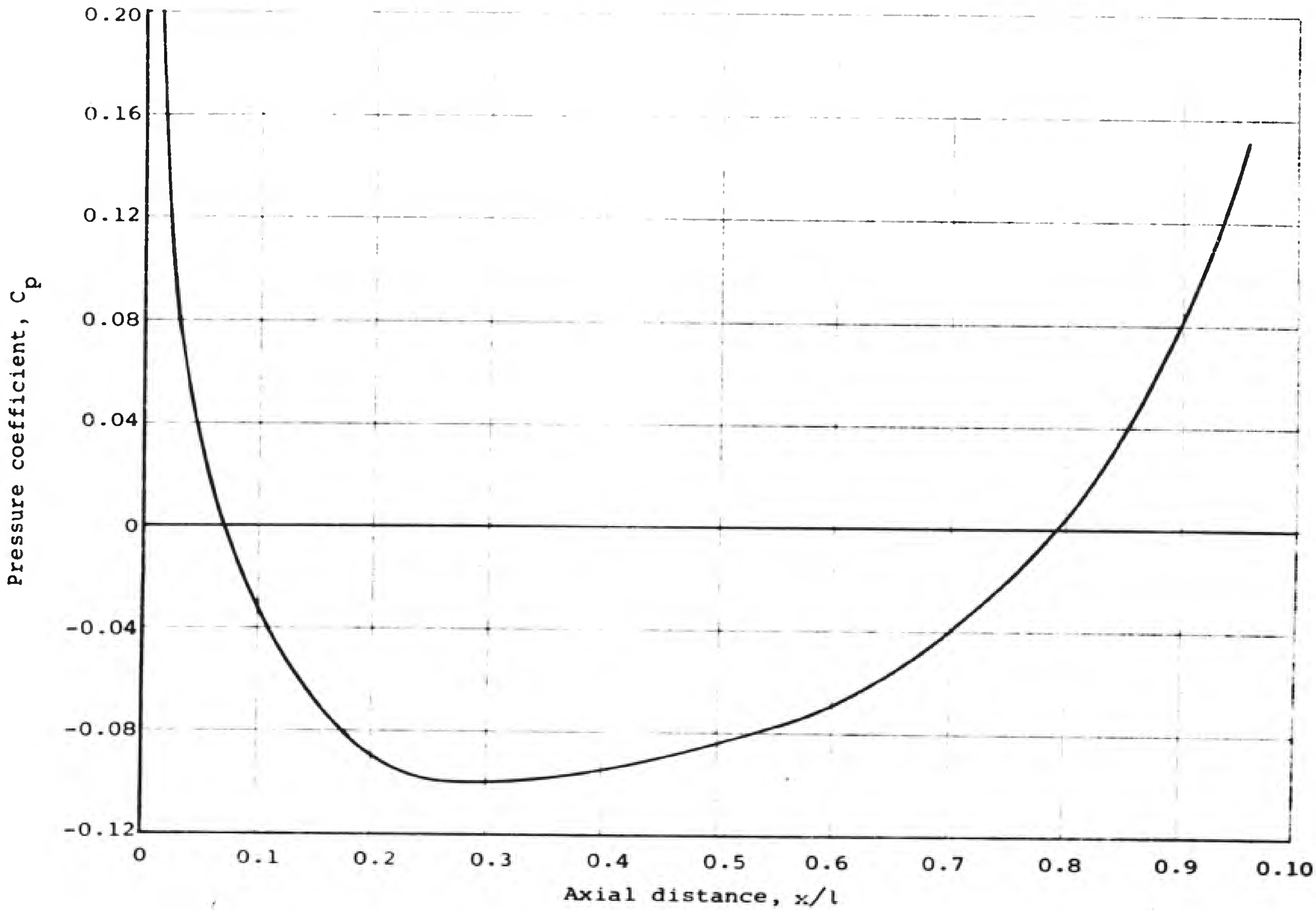


Figure 24. - Pressure distribution on representative submarine hull.

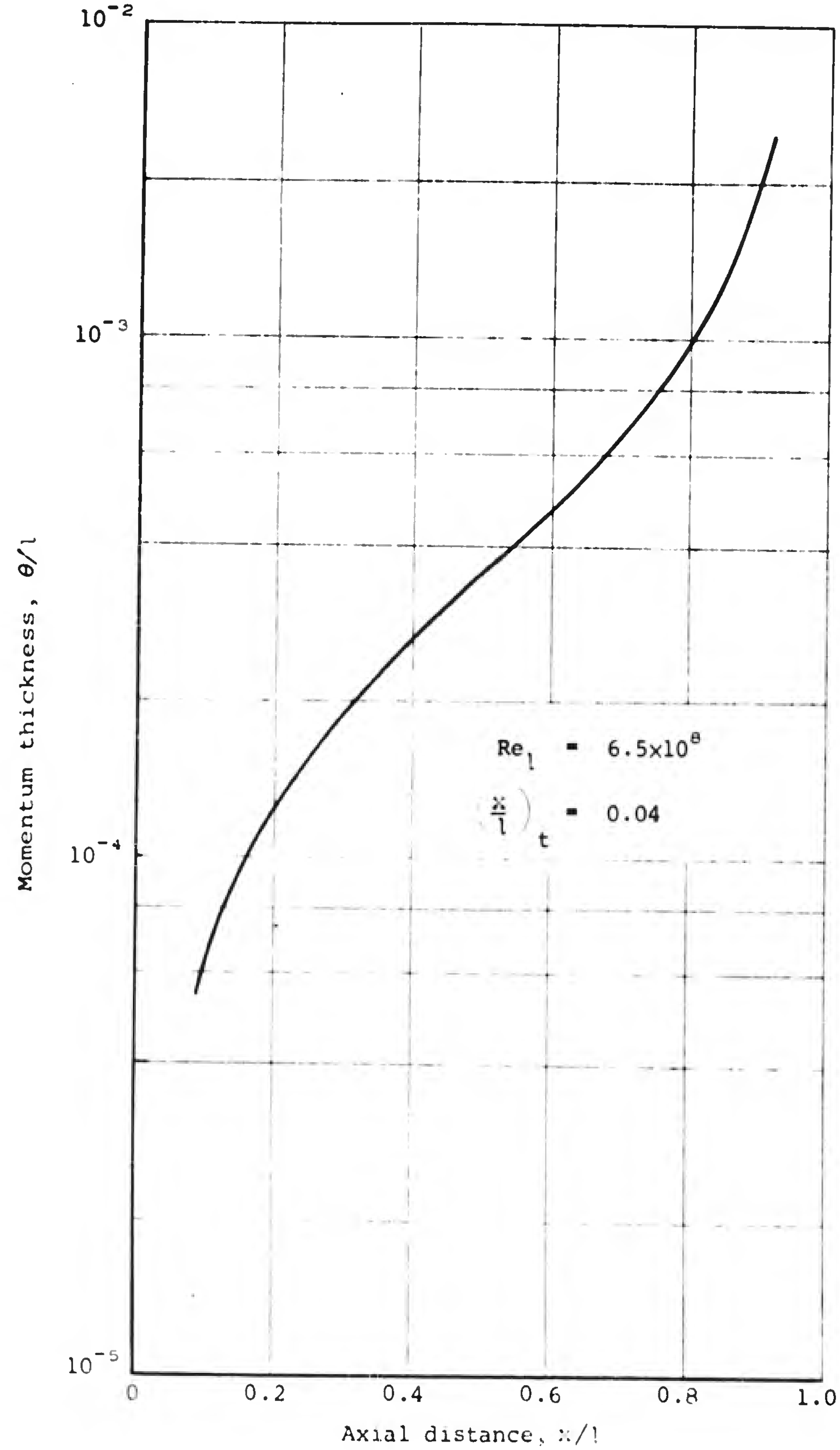


Figure 25. - Boundary-layer momentum thickness for representative configuration.

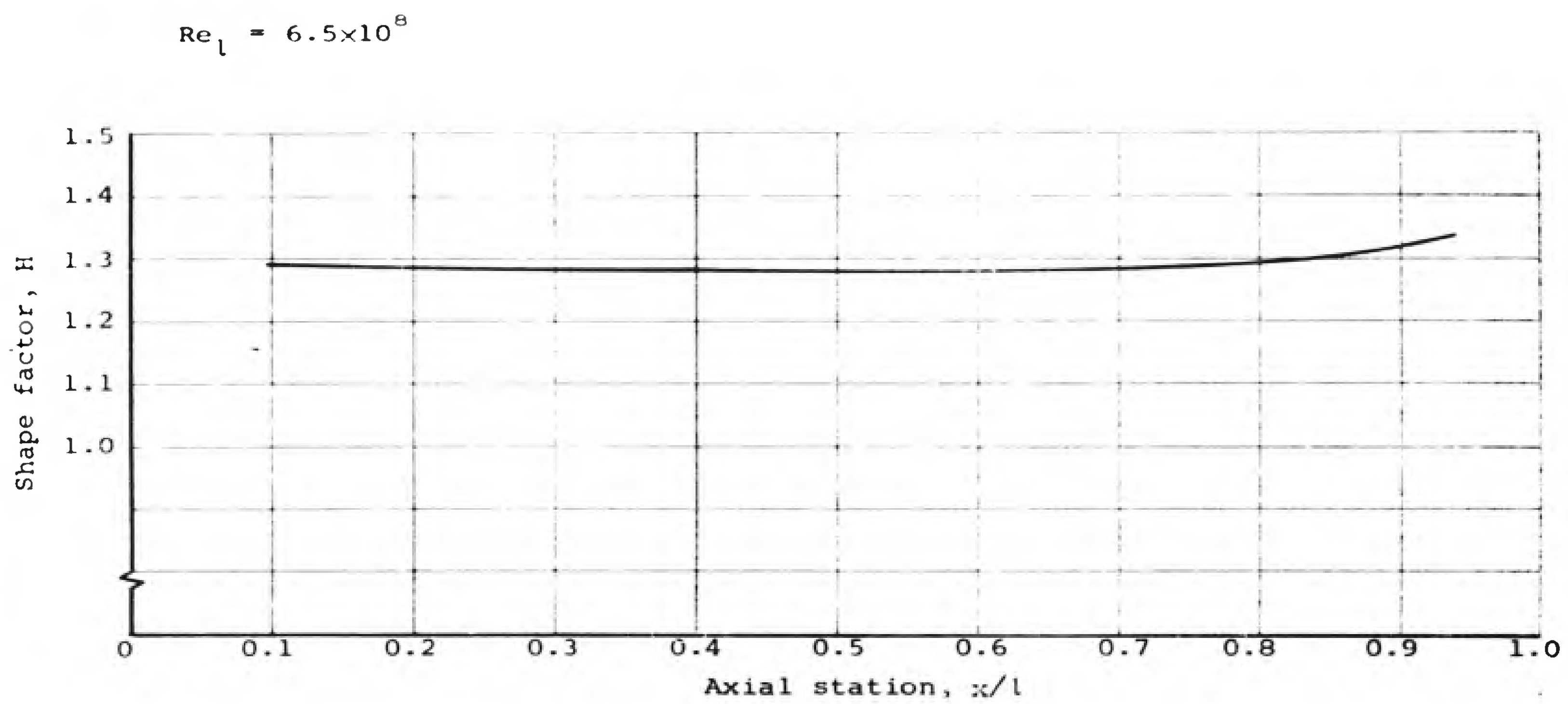


Figure 26. - Boundary-layer shape factor for representative configuration.

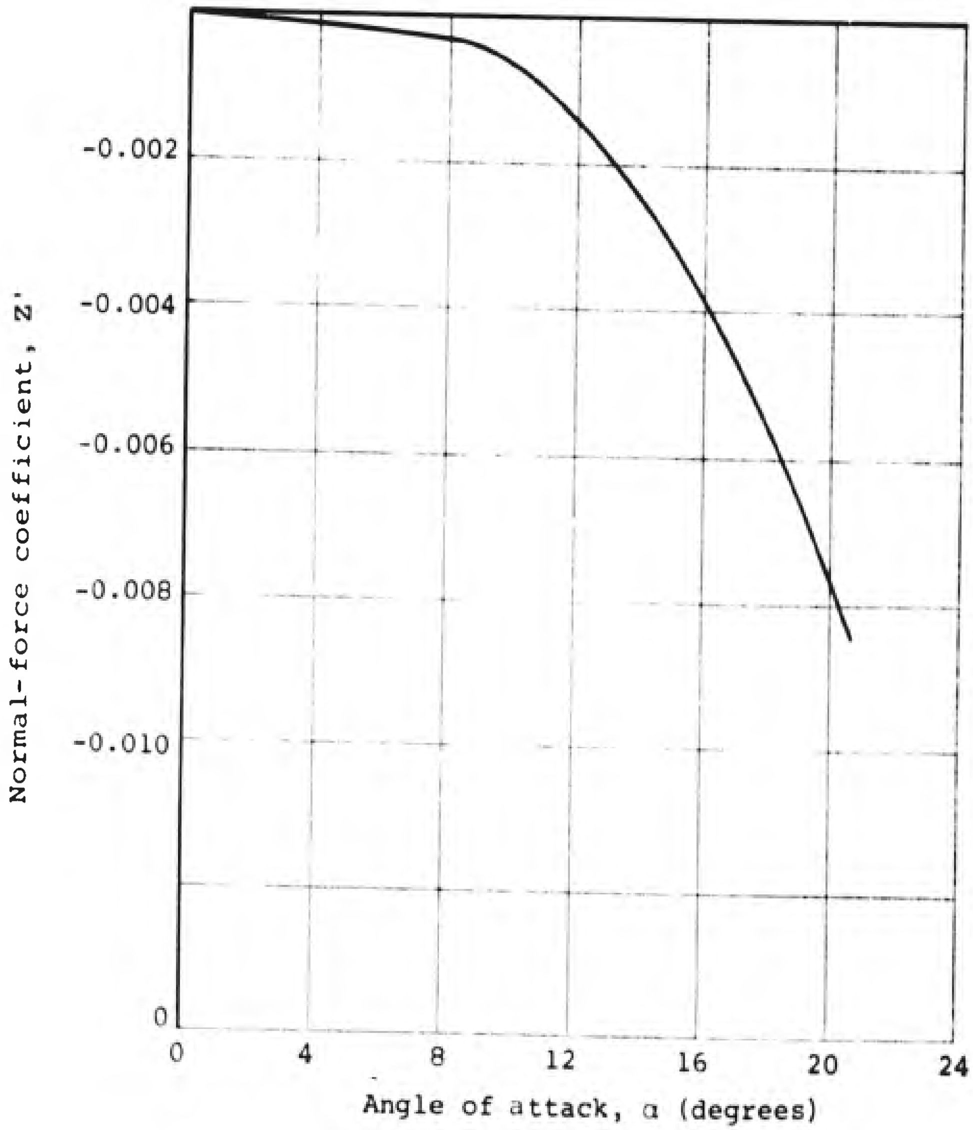


Figure 27. - Theoretical normal-force coefficient on representative submarine hull alone.

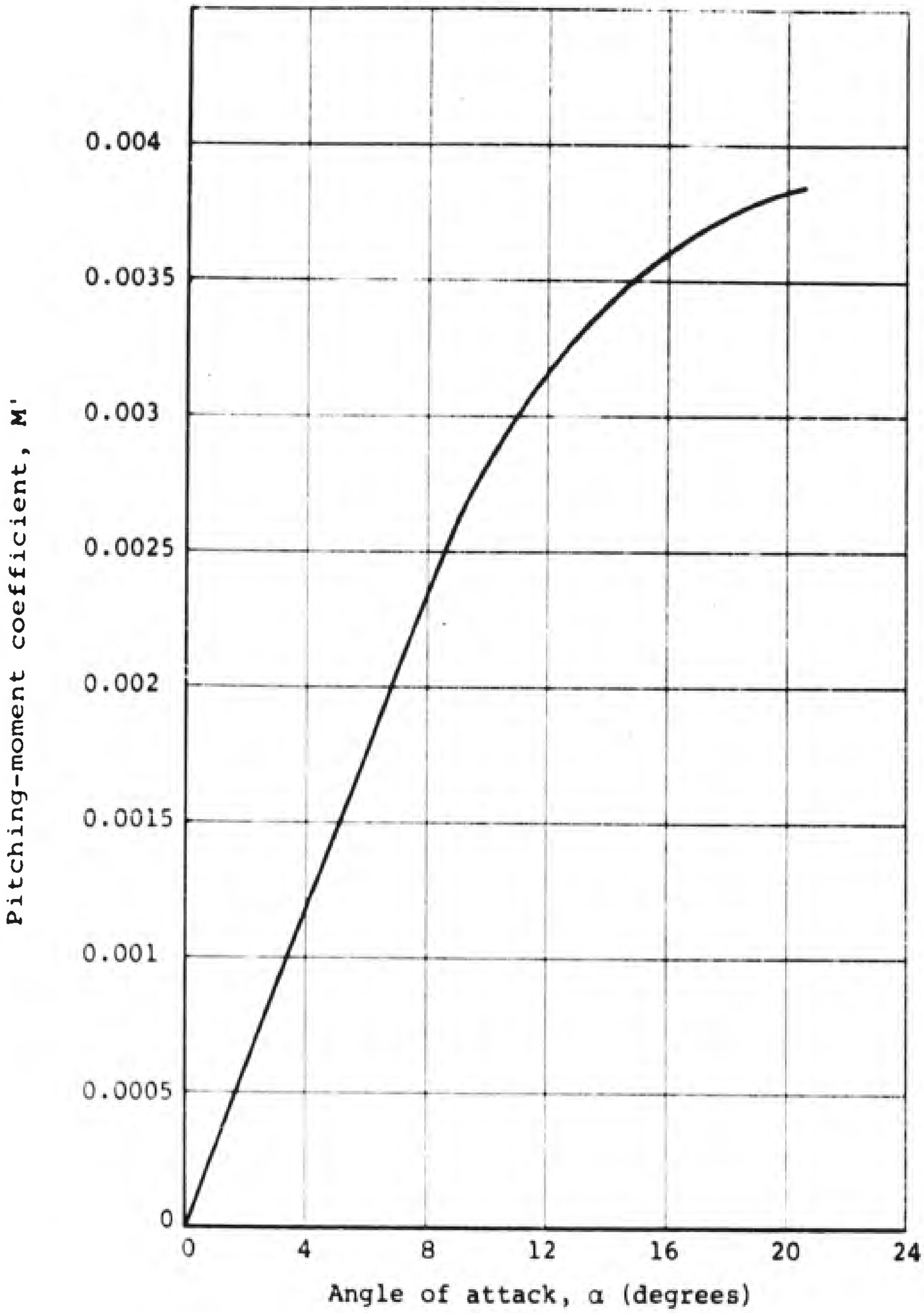


Figure 28. - Theoretical pitching-moment coefficient on representative submarine hull alone.

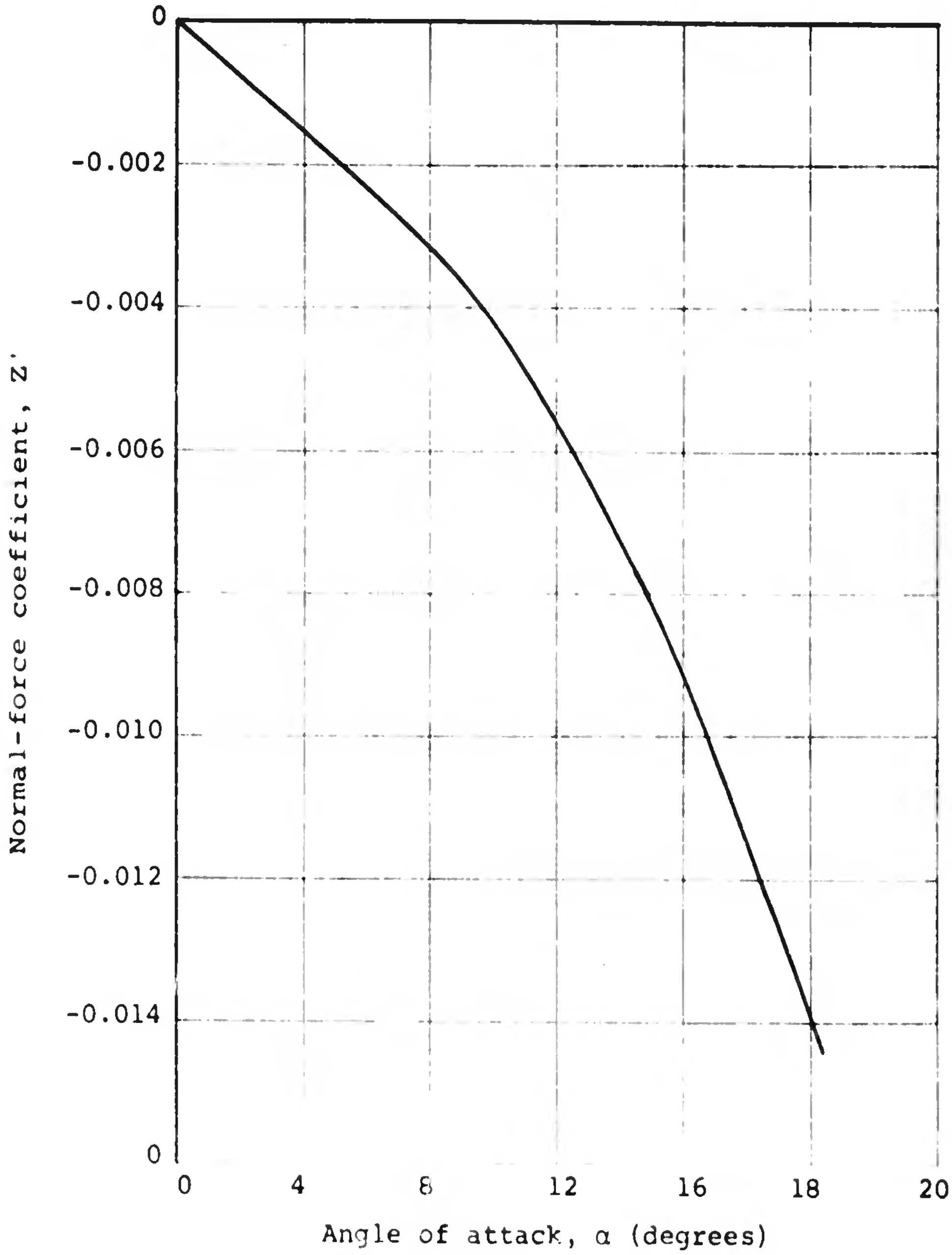


Figure 29. - Theoretical normal-force coefficient on representative submarine hull with stern planes.

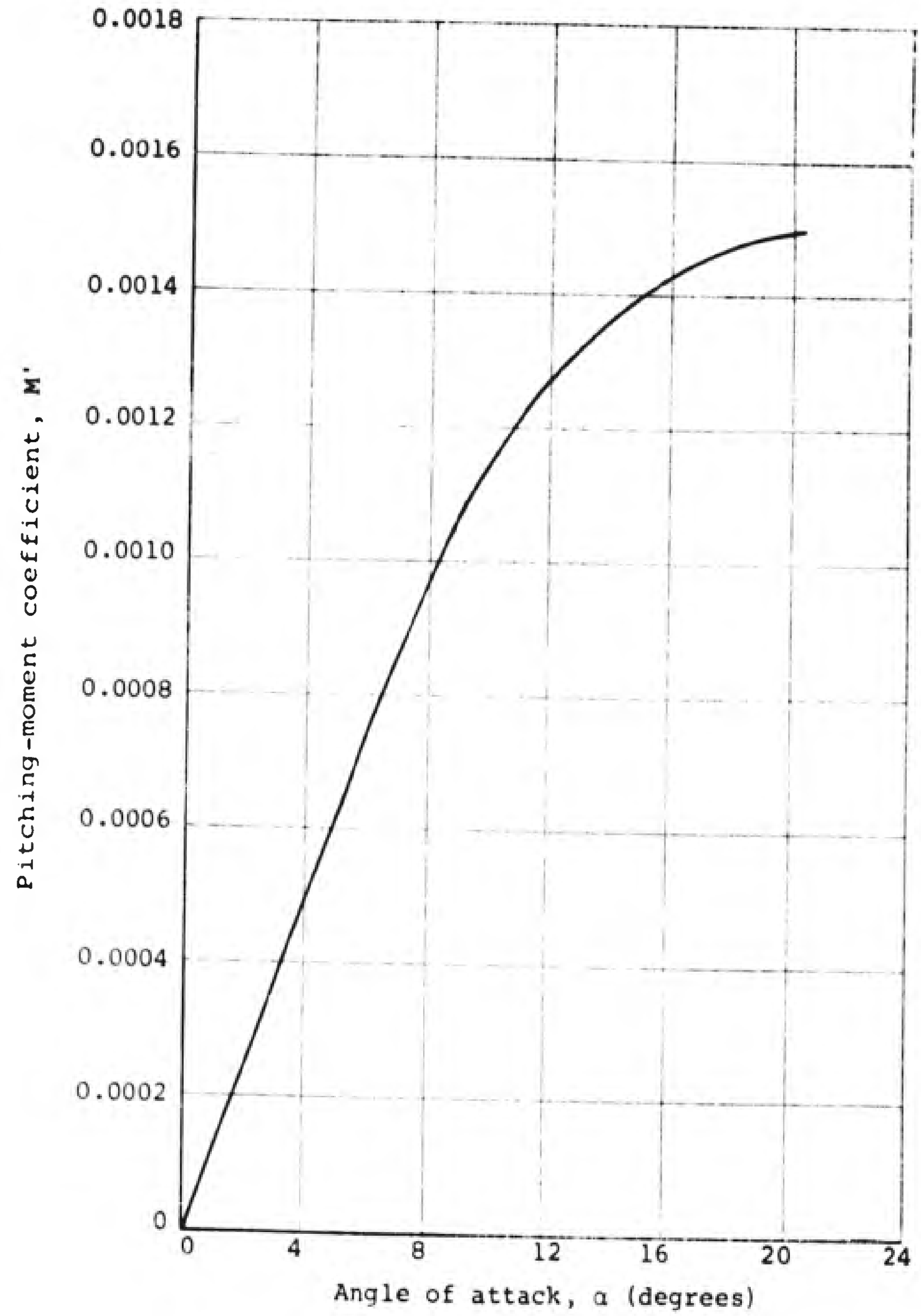


Figure 30. - Theoretical pitching-moment coefficient on representative submarine hull with stern planes.

## INITIAL DISTRIBUTION LIST
## (PART I)

Chief of Naval Research
Department of the Navy
Washington 25, D. C.
Attn: Codes 438 (3)
416 (1)
461 (1)

Commanding Officer
Office of Naval Research
Branch Office
495 Summer Street
Boston 10, Massachusetts (1)

Commanding Officer
Office of Naval Research
Branch Office
86 East Randolph Street
Chicago 1, Illinois (1)

Commanding Officer
Office of Naval Research
Branch Office
207 West 24th Street
New York 11, New York (1)

Commanding Officer
Office of Naval Research
Branch Office
Navy 100, Box 39, Fleet Post Office
New York, New York (25)

Commanding Officer
Office of Naval Research
Branch Office
1030 East Green Street
Pasadena 1, California (1)

Commanding Officer
Office of Naval Research
Branch Office
1000 Geary Street
San Francisco 9, California (1)

Director
Naval Research Laboratory
Washington 25, D. C.
Attn: Codes 2000 (1)
2020 (1)
2027 (6)

Chief, Bureau of Ships
Department of the Navy
Washington 25, D. C.
Attn: Codes 300 (1)
305 (1)
335 (1)
341 (1)
342A (1)
345 (1)
420 (1)
421 (1)
440 (1)
442 (1)
525 (1)
634A (1)

Chief, Bureau of Naval Weapons
Department of the Navy
Washington 25, D. C.
Attn: Codes R (1)
R-12 (1)
RAAD (1)
RR (1)
RRRE (1)
RU (1)
RUTO (1)

Director, Special Projects Office
Department of the Navy
Washington 25, D. C.
Attn: Codes SP-001 (1)
SP-201 (1)

Chief, Bureau of Yards and Docks
Department of the Navy
Washington 25, D. C.
Attn: Codes D-202 (1)
D-400 (1)
D-500 (1)

Commanding Officer and Director
David Taylor Model Basin
Washington 7, D. C.
Attn: Codes 142 (1)
500 (1)
513 (75)
521 (1)
522 (1)
526 (1)
530 (1)
550 (1)

Commanding Officer
NROTC and Naval Administrative
Unit
Massachusetts Institute of
Technology
Cambridge 39, Massachusetts (1)

Commanding Officer
U.S. Naval Underwater Ordnance
Station
Newport, Rhode Island
Attn: Research Division (1)

Commanding Officer and Director
U.S. Navy Mine Defense Laboratory
Panama City, Florida (1)

Commander
San Francisco Naval Shipyard
San Francisco 24, California (1)

Commander
Mare Island Naval Shipyard
Vallejo, California (1)

Air Force Office of Scientific
Research
Mechanics Division
Washington 25, D. C. (1)

Defense Documentation Center
Arlington Hall Station
Arlington 12, Virginia (10)

Office of Technical Services
Department of Commerce
Washington 25, D. C. (1)

Fluid Mechanics Section
National Bureau of Standards
Washington 25, D. C.
Attn: Dr. G. B. Schubauer (1)

Director
Engineering Science Division
National Science Foundation
Washington D. C. (1)

National Academy of Sciences
National Research Council
2101 Constitution Ave., N. W.
Washington 25, D. C. (1)

The Johns Hopkins University
Baltimore 18, Maryland
Attn: Professor S. Corrsin (1)
Professor F. H. Clauser (1)
Professor O. M. Phillips (1)

Director
Applied Physics Laboratory
The John Hopkins University
8621 Georgia Avenue
Silver Spring, Maryland (1)

California Institute of Technology
Pasadena 4, California
Attn: Hydrodynamics Laboratory (1)
Professor T. Y. Wu (1)
Professor A. T. Ellis (1)
Professor A. J. Acosta (1)
Professor M. S. Plesset (1)
Dr. J. Laufer (1)

University of California
Berkeley 4, California
Attn: Department of Engineering (1)
Professor H. A. Schade (1)
Professor J. W. Johnson (1)
Professor J. V. Wehausen (1)

Director
Scripps Institution of Oceanography
University of California
La Jolla, California (1)

Iowa Institute of Hydraulic Research
State University of Iowa
Iowa City, Iowa
Attn: Professor H. Rouse (1)
Professor L. Landweber (1)
Professor P. G. Hubbard (1)

Harvard University
Cambridge 38, Massachusetts
Attn: Professor G. Birkhoff (1)
Professor G. F. Carrier (1)
Professor S. Goldstein (1)
Professor B. Budiansky (1)

University of Michigan
Ann Arbor, Michigan
Attn: Engineering Research Institute
Professor R. B. Couch (1)

National Research Council
Montreal Road
Ottawa 2, Canada
Attn: Mr. E. S. Turner (1)

Webb Institute of Naval Architecture
Glen Cove, Long Island, New York
Attn: Professor E. V. Lewis (1)
Technical Library (1)

Institute of Mathematical Sciences
New York University
25 Waverly Place
New York 3, New York
Attn: Professor J. J. Stoker (1)
Professor A. Peters (1)
Professor J. Keller (1)
Professor R. Courant (1)

Director
Ordnance Research Laboratory
Pennsylvania State University
University Park, Pennsylvania
Attn: Dr. E. J. Skudrzyk (1)
Dr. G. F. Wislicenus (1)
Dr. M. Sevik (1)

Director
St. Anthony Falls Hydraulic Laboratory
Minneapolis 14, Minnesota (1)
Attn: Mr. J. N. Wetzel (1)
Professor B. Silberman (1)
Professor E. R. Eckert (1)

Massachusetts Institute of Technology
Cambridge 39, Massachusetts
Attn: Professor P. Mandel (1)
Professor M. Abkowitz (1)
Dr. Leon H. Schindel (1)

Stevens Institute of Technology
Davidson Laboratory
Hoboken, New Jersey
Attn: Mr. D. Savitsky (1)
Mr. J. P. Breslin (1)
Dr. S. J. Lukasik (1)
Mr. H. W. MacDonald (1)
Mr. E. Numata (1)
Dr. P. N. Hu (1)

Dr. L. L. Higgins
Space Technology Laboratories Inc.
Canoga Park Facility
8433 Fallbrook Avenue
Canoga Park, California (1)

Dr. A. Ritter
Therm Advanced Research Division
Therm, Incorporated
Ithaca, New York (1)

Hydronautics, Incorporated
Pindell School Road
Howard County
Laurel, Maryland
Attn: Mr. P. Eisenberg, Pres. (1)
Mr. M. P. Tulin, V. Pres. (1)

Technical Research Group, Inc.
2 Aerial Way
Syosset, Long Island, New York
Attn: Dr. J. Kotick (1)

AiResearch Manufacturing Company
9851-9951 Sepulveda Boulevard
Los Angeles 45, California
Attn: Blaine R. Parking (1)

Hydrodynamics Laboratory
Convair
San Diego 12, California
Attn: Mr. H. E. Brooke (1)
Mr. R. H. Oversmith (1)

Aerojet-General Corporation
6352 N. Irwindale Avenue
Azusa, California
Attn: Mr. C. A. Gongwer (1)

Republic Aviation Corporation
Farmingdale, Long Island, New York
Attn: Mr. J. Malloy, Manager
Hydrospace Systems Div. (1)

Department of Engineering Mechanics
University of Notre Dame
Notre Dame, Indiana
Attn: Professor A. G. Strandhagen (1)

Vidya Division, Itek Corporation
1450 Page Mill Road
Palo Alto, California
Attn: Dr. A. Sacks (1)

Stanford University
Stanford, California
Attn: Dr. Bryne Perry (1)

Aeronautical Engineering
Department
Catholic University of America
Washington, D. C.
Attn: Professor M. Munk, Head (1)

Department of Aeronautical
Engineering
University of Colorado
Boulder, Colorado
Attn: Professor M. S. Uberoi (1)

ASW and Ocean Systems Department
Lockheed Aircraft Corporation
Burbank, California
Attn: Mr. G. W. Paper (1)

Electric Boat Division
General Dynamics Corporation
Groton, Connecticut
Attn: Mr. R. McCandliss (1)

Missile Development Division
North American Aviation, Inc.
Downey, California
Attn: Dr. E. R. Van Driest (1)

U. S. Rubber Company
Research and Development Department
Wayne, New Jersey
Attn: Mr. L. M. White (1)

Douglas Aircraft Company, Inc.
Aircraft Division
Long Beach, California
Attn: Mr. A. M. O. Smith (1)

Vidya Division, Itek Corporation
1450 Page Mill Road, Palo Alto, California
THE EFFECT OF FLOW SEPARATION FROM THE HULL ON THE STABILITY OF A HIGH-SPEED SUBMARINE. PART I - THEORY,
by S. B. Spangler, A. H. Sacks, J. N. Nielsen
Vidya Report No. 107, August 1963. 84 pages, 30 illus.,
(Contract No. Nonr 3934(00)) Unclassified report

A theoretical analysis of the force distribution induced on an inclined body of revolution by flow separation at high angle of attack has been made. The separated flow over the body is characterized by a steady vortex sheet system, upon which an inviscid analysis is made. The theory is applied to a typical, high-speed submarine configuration, using an assumed location of the separation line based on existing experimental data. Separation induced forces were found to occur at 8° angle of attack and to become appreciable compared to non-separated forces and moments at 20° angle of attack.

UNCLASSIFIED

1. Submarines - Stability
2. Submarines - Maneuverability - Submerged conditions
3. Bodies of Revolution - TMB series 58 - Forces and Moments

I Spangler, S. B.
II Sacks, A. H.
III Nielsen, J. N.

Vidya Division, Itek Corporation
1450 Page Mill Road, Palo Alto, California
THE EFFECT OF FLOW SEPARATION FROM THE HULL ON THE STABILITY OF A HIGH-SPEED SUBMARINE. PART I - THEORY,
by S. B. Spangler, A. H. Sacks, J. N. Nielsen
Vidya Report No. 107, August 1963. 84 pages, 30 illus.,
(Contract No. Nonr 3934(00)) Unclassified report

A theoretical analysis of the force distribution induced on an inclined body of revolution by flow separation at high angle of attack has been made. The separated flow over the body is characterized by a steady vortex sheet system, upon which an inviscid analysis is made. The theory is applied to a typical, high-speed submarine configuration, using an assumed location of the separation line based on existing experimental data. Separation induced forces were found to occur at 8° angle of attack and to become appreciable compared to non-separated forces and moments at 20° angle of attack.

UNCLASSIFIED

1. Submarines - Stability
2. Submarines - Maneuverability - Submerged conditions
3. Bodies of Revolution - TMB series 58 - Forces and Moments

I Spangler, S. B.
II Sacks, A. H.
III Nielsen, J. N.

Vidya Division, Itek Corporation
1450 Page Mill Road, Palo Alto, California
THE EFFECT OF FLOW SEPARATION FROM THE HULL ON THE STABILITY OF A HIGH-SPEED SUBMARINE. PART I - THEORY,
by S. B. Spangler, A. H. Sacks, J. N. Nielsen
Vidya Report No. 107, August 1963. 84 pages, 30 illus.,
(Contract No. Nonr 3934(00)) Unclassified report

A theoretical analysis of the force distribution induced on an inclined body of revolution by flow separation at high angle of attack has been made. The separated flow over the body is characterized by a steady vortex sheet system, upon which an inviscid analysis is made. The theory is applied to a typical, high-speed submarine configuration, using an assumed location of the separation line based on existing experimental data. Separation induced forces were found to occur at 8° angle of attack and to become appreciable compared to non-separated forces and moments at 20° angle of attack.

UNCLASSIFIED

1. Submarines - Stability
2. Submarines - Maneuverability - Submerged conditions
3. Bodies of Revolution - TMB series 58 - Forces and Moments

I Spangler, S. B.
II Sacks, A. H.
III Nielsen, J. N.

Vidya Division, Itek Corporation
1450 Page Mill Road, Palo Alto, California
THE EFFECT OF FLOW SEPARATION FROM THE HULL ON THE STABILITY OF A HIGH-SPEED SUBMARINE. PART I - THEORY,
by S. B. Spangler, A. H. Sacks, J. N. Nielsen
Vidya Report No. 107, August 1963. 84 pages, 30 illus.,
(Contract No. Nonr 3934(00)) Unclassified report

A theoretical analysis of the force distribution induced on an inclined body of revolution by flow separation at high angle of attack has been made. The separated flow over the body is characterized by a steady vortex sheet system, upon which an inviscid analysis is made. The theory is applied to a typical, high-speed submarine configuration, using an assumed location of the separation line based on existing experimental data. Separation induced forces were found to occur at 8° angle of attack and to become appreciable compared to non-separated forces and moments at 20° angle of attack.

UNCLASSIFIED

1. Submarines - Stability
2. Submarines - Maneuverability - Submerged conditions
3. Bodies of Revolution - TMB series 58 - Forces and Moments

I Spangler, S. B.
II Sacks, A. H.
III Nielsen, J. N.

Vidya Division, Itek Corporation
1450 Page Mill Road, Palo Alto, California
THE EFFECT OF FLOW SEPARATION FROM THE HULL ON THE STABILITY OF A HIGH-SPEED SUBMARINE. PART I - THEORY,
by S. B. Spangler, A. H. Sacks, J. N. Nielsen
Vidya Report No. 107, August 1963. 84 pages. 30 illus.,
(Contract No. Nonr 3934(00)) Unclassified report

A theoretical analysis of the force distribution induced on an inclined body of revolution by flow separation at high angle of attack has been made. The separated flow over the body is characterized by a steady vortex sheet system, upon which an inviscid analysis is made. The theory is applied to a typical, high-speed submarine configuration, using an assumed location of the separation line based on existing experimental data. Separation induced forces were found to occur at 8° angle of attack and to become appreciable compared to non-separated forces and moments at 20° angle of attack.

UNCLASSIFIED

1. Submarines - Stability
2. Submarines - Maneuverability - Submerged conditions
3. Bodies of Revolution - TMB series 58 - Forces and Moments

I Spangler, S. B.
II Sacks, A. H.
III Nielsen, J. N.

Vidya Division, Itek Corporation
1450 Page Mill Road, Palo Alto, California
THE EFFECT OF FLOW SEPARATION FROM THE HULL ON THE STABILITY OF A HIGH-SPEED SUBMARINE. PART I - THEORY,
by S. B. Spangler, A. H. Sacks, J. N. Nielsen
Vidya Report No. 107, August 1963. 84 pages. 30 illus.,
(Contract No. Nonr 3934(00)) Unclassified report

A theoretical analysis of the force distribution induced on an inclined body of revolution by flow separation at high angle of attack has been made. The separated flow over the body is characterized by a steady vortex sheet system, upon which an inviscid analysis is made. The theory is applied to a typical, high-speed submarine configuration, using an assumed location of the separation line based on existing experimental data. Separation induced forces were found to occur at 8° angle of attack and to become appreciable compared to non-separated forces and moments at 20° angle of attack.

UNCLASSIFIED

1. Submarines - Stability
2. Submarines - Maneuverability - Submerged conditions
3. Bodies of Revolution - TMB series 58 - Forces and Moments

I Spangler, S. B.
II Sacks, A. H.
III Nielsen, J. N.

Vidya Division, Itek Corporation
1450 Page Mill Road, Palo Alto, California
THE EFFECT OF FLOW SEPARATION FROM THE HULL ON THE STABILITY OF A HIGH-SPEED SUBMARINE. PART I - THEORY,
by S. B. Spangler, A. H. Sacks, J. N. Nielsen
Vidya Report No. 107, August 1963. 84 pages. 30 illus.,
(Contract No. Nonr 3934(00)) Unclassified report

A theoretical analysis of the force distribution induced on an inclined body of revolution by flow separation at high angle of attack has been made. The separated flow over the body is characterized by a steady vortex sheet system, upon which an inviscid analysis is made. The theory is applied to a typical, high-speed submarine configuration, using an assumed location of the separation line based on existing experimental data. Separation induced forces were found to occur at 8° angle of attack and to become appreciable compared to non-separated forces and moments at 20° angle of attack.

UNCLASSIFIED

1. Submarines - Stability
2. Submarines - Maneuverability - Submerged conditions
3. Bodies of Revolution - TMB series 58 - Forces and Moments

I Spangler, S. B.
II Sacks, A. H.
III Nielsen, J. N.

Vidya Division, Itek Corporation
1450 Page Mill Road, Palo Alto, California
THE EFFECT OF FLOW SEPARATION FROM THE HULL ON THE STABILITY OF A HIGH-SPEED SUBMARINE. PART I - THEORY,
by S. B. Spangler, A. H. Sacks, J. N. Nielsen
Vidya Report No. 107, August 1963. 84 pages. 30 illus.,
(Contract No. Nonr 3934(00)) Unclassified report

A theoretical analysis of the force distribution induced on an inclined body of revolution by flow separation at high angle of attack has been made. The separated flow over the body is characterized by a steady vortex sheet system, upon which an inviscid analysis is made. The theory is applied to a typical, high-speed submarine configuration, using an assumed location of the separation line based on existing experimental data. Separation induced forces were found to occur at 8° angle of attack and to become appreciable compared to non-separated forces and moments at 20° angle of attack.

UNCLASSIFIED

1. Submarines - Stability
2. Submarines - Maneuverability - Submerged conditions
3. Bodies of Revolution - TMB series 58 - Forces and Moments

I Spangler, S. B.
II Sacks, A. H.
III Nielsen, J. N.

UNCLASSIFIED

UNCLASSIFIED